A MULTISCALE STUDY OF CAVITATION MECHANISM AND DAMAGE IN SOFT MATERIALS

by

FUAD HASAN

Presented to the Faculty of the Graduate School of

The University of Texas at Arlington in Partial Fulfillment

of the Requirements

for the Degree of

DOCTOR OF PHILOSOPHY

THE UNIVERSITY OF TEXAS AT ARLINGTON

August 2020

Acknowledgments

This thesis is the testimony to those who have helped me enormously to make it possible.

First, I would like to sincerely thank my supervisor, Professor Ashfaq Adnan, for his support and encouragement throughout my Ph.D. life. His approach to mentor a student suited my work ethics and helped me develop as a researcher. I would also like to thank Professor Kamesh Subbarao, Professor Brian Dennis, Professor Kent Lawrence, and Professor MD Sahadat Hossain for taking the time to serve on my dissertation committee. Special thanks to Professor Brian Dennis for letting me use his supercomputing facility (CFDLAB) as well as to his student Dr. Sandeep Patil who helped a lot in my study. My thanks to Assistant Professor Wonmo Kang from Arizona State University for helping me with my research.

My sincere gratitude to all the faculty members and staff of the MAE Department. Special thanks to my lab mates, KAH Al Mahmud, Riaz Kayser, Saket Thapliyal, Rajni Chahal, Megha Tangri, and Ishak Khan.

To all my family and friends, I appreciate all your support and encouragement over the years. I cannot thank enough my parents H A Gofran and Begum Rezia, and my siblings Farhana Parvin and Fahmida Parveen and their husbands, four wonderful nieces and nephews Zara, Nuha, Sami, and Sara.

Lastly, my words cannot describe my gratitude to my loving and caring wife, Moushumi Kabir, who has been my constant encouragement. Thank you for giving me the most significant gift of my life, our daughter, Sophia Ruhi Hasan. Hats off to you for all your sacrifices for which I am indebted to you for a lifetime.

July 23, 2020

Abstract

A MULTISCALE STUDY OF CAVITATION MECHANISM

AND DAMAGE IN SOFT MATERIALS

Fuad Hasan, PhD

The University of Texas at Arlington, 2020

Supervising Professor: Ashfaq Adnan

Cavitation is defined as the formation and growth of the gaseous bubble in bulk liquid due to the tensile pressure followed by the violent collapse. The collapse of the bubble is particularly significant due to its potential to cause damage to relatively stronger materials by either creating pressure waves (symmetric collapse) or liquid jet (asymmetric collapse). The study of cavitation in soft materials (e.g., tissue, brain, gelatin gel, etc.) has, therefore, gained a fair share of attention in the scientific communities. Recent studies have indicated that cavitation could be one of the leading causes of the mild Traumatic Brain Injury (TBI) and greatly motivates us to study the cavitation mechanism in soft materials from a multiscale perspective. The goal of this work is to study, i) cavitation onset criteria, ii) damage intensity, and iii) axonal damage mechanism.

The microstructure of the gelatin gel is studied by observing the scanning electron microscope (SEM) images of the random fiber network (RFN). The geometric and material properties are evaluated by proposing a unit cell model of the network. A theoretical model is developed to incorporate the bubble growth in the network to quantify the threshold tensile pressure as the onset criteria of cavitation in soft materials.

The study of the onset criteria is followed by the study of cavitation damage intensity in soft materials. Shock-bubble interaction with symmetric collapse has been studied. A multiphase, compressible, and viscoelastic computational fluid dynamics

(CFD) model has been developed to simulate the bubble dynamics. Several damage criteria (e.g., stress, strain, and energy based) have been proposed, and a parametric study has been done.

Finally, a complete material characterization of the neuronal cell (e.g., axon) has been performed. A representative volume element (RVE) of the axon is developed based on its cytoskeletal components. Nine independents (orthotropic) viscoelastic relaxation modulus are evaluated by nonlinear regression fit to the Prony series. This viscoelastic constitutive model of axon will be used to study the diffuse axonal injury (DAI).

Table of Contents

List of Illustrations

List of Tables

Chapter 1

Introduction

The study of cavitation in the field of hydrodynamics can be broadly grouped into three categories, i) nucleation theory, ii) bubble dynamics, and iii) damage mechanism. The classical nucleation theory (CNT) deals with phase change phenomena, liquid tensile strength, and nucleation rate [1]–[7]. Bubble dynamics, on the other hand, studies the stability of the bubble, natural frequency, bubble growth-collapse due to the far-field pressure. The damage mechanism due to the bubble collapse can be characterized as the formation of secondary pressure wave, high strain rate deformation of the surrounding medium for symmetric collapse (Rayleigh collapse), and high energetic liquid jet formation in the case of asymmetric collapse. The symmetric collapse is typical of the cavitating flows where asymmetric collapse is due to either geometric asymmetry or shock-bubble interaction [8]. However, cavitation phenomena are both qualitatively and quantitively different in soft materials. Recently the topic has gained its importance as it has interdisciplinary implications to mTBI [9]–[14], micro-rheology of soft materials [15]–[17], drug delivery [18]–[21], medical treatment (i.e., lithotripsy) [22]–[24], etc. Therefore, the goals of this work are to study the cavitation onset criteria and the damage mechanism in soft materials and to evaluate how they differ from the pure liquid (e.g., water).

In this chapter, a brief discussion is given on the nucleation theory and the damage mechanism in pure liquid, followed by the discussion of cavitation in soft materials. In chapter 2, a theoretical model is developed to quantify the onset criteria on the threshold tensile pressure in soft materials. Samples of the gelatin gel of different concentrations are prepared, and the SEM images are studied in detail to develop a theoretical model of the microstructural effect on the onset of cavitation. Then symmetric

collapse of the cavitating bubble is studied in chapter 3. A multiphase, compressible, and viscoelastic CFD model is developed for simulating the bubble dynamics. Several damage criteria are proposed, and a parametric study is shown for different material parameters. Finally, a composite RVE modeling of the neuronal cell (e.g., axon) is presented in chapter 4, and complete viscoelastic material characterization is done.

Classical Nucleation Theory (CNT)

The classical nucleation theory deals with the phase change phenomena, followed by the mechanical and thermodynamic stability of the critical bubble nuclei, the energetics of bubble formation, and the nucleation rate.

Phase Change Phenomena

The discussion of CNT should start with the thermodynamics of phase change phenomena, and we can assume that the van der Waals equation of state (EOS) is valid for the liquid-vapor transition given as,

$$P = \frac{(\bar{R}/\bar{M})T}{v - b} - \frac{a}{v^2} \tag{1.1}$$

Where P is pressure, T is temperature, $\bar{R}$ is the universal gas constant, $\bar{M}$ is molecular weight, v is the specific volume, a, and b are material properties. The isothermal solution of $(\partial P/\partial v)_T$ of equation 1.1 is shown in figure 1-1, which is the line ABCDEFG. AB is the liquid phase where B corresponds to the saturation condition at the given temperature, T_0. Now, if enough nucleation sites are available, then we can reach F, and the transition takes place from liquid to vapor. But without the favorable perturbation (not enough nucleation sites of critical size), the liquid can have states between B and C. This condition of liquid is called the *metastable* liquid. However, the

line ABCDEFG is valid since it satisfies the thermodynamic equilibrium. Still, a portion of it (e.g., CDE) does not correspond to any realizable state since it violates the mechanical equilibrium. The mechanical equilibrium states that, $(\partial P/\partial v)_T < 0$, and hence CDE is not permitted [25].

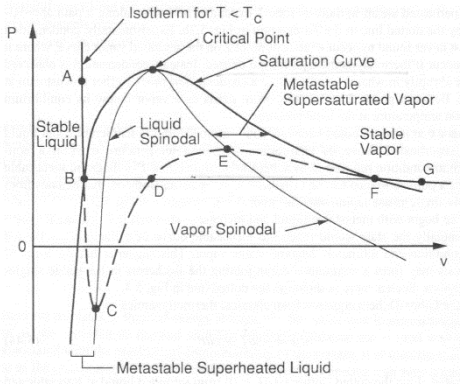

Figure 1-1 P-v diagram of the liquid-vapor system showing the *metastable* (B-C and E-F) regions and *spinodal* lines [25].

A *metastable* liquid (between B and C) having pressure (P_{nuc}) is said to be in tension, and the tensile pressure is given as, $\Delta P = (P(T_0)_{sat} - P_{nuc})$. Several authors have defined ΔP as the tensile strength of the liquid [1]. From figure 1-2 we can see there exists two valid states, *b,* and *c* at the pressure, P_{nuc} that corresponds to *metastable* liquid and stable vapor phase, respectively (*a* is not valid). Therefore, a *metastable* liquid (state *b*) may remain liquid indefinitely or jump to state *c* (stable vapor phase). This conditional equilibrium can be explained further based on the critical bubble radius (R_o), which we will discuss in the next sub-section.

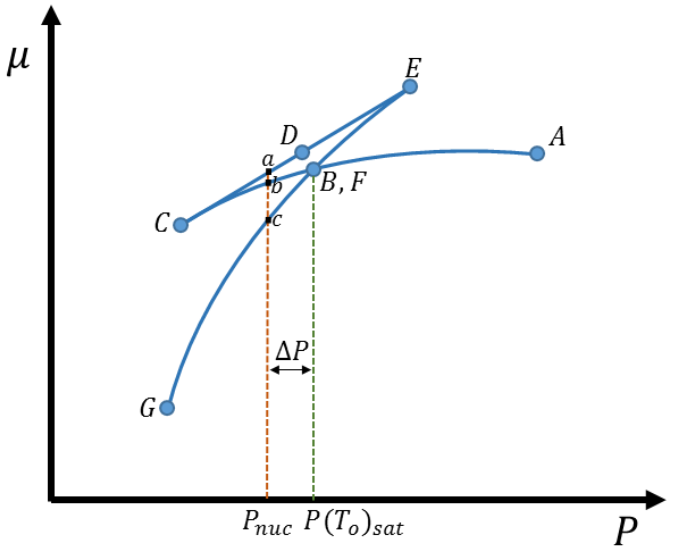

Figure 1-2 Shape of the chemical potential vs. pressure variation along an isotherm as predicted by the van der Waals equation [25].

Mechanical and Thermodynamic Stability of the Critical Bubble Nuclei

If we assume that there exists a bubble with a radius R_o in a *metastable* liquid subject to tensile pressure, then thermodynamics equilibrium requires that chemical potential of the two phases are same, $\mu_l = \mu_v \; at \; T_0$. On the other hand, mechanical equilibrium is established by the *Young-Laplace* equation which states that the internal bubble pressure (P_B) and the external liquid pressure must be balanced by the surface tension (S) effect, $P_B = P_{nuc} + 2S/R_o$. These two equilibrium conditions can be used along with the ideal gas EOS for vapor and incompressible assumption for the liquid to arrive at the critical bubble radius [25] for the specific volume of liquid (v_l) and vapor gas constant (R_v),

$$R_o = \frac{2S}{P(T_0)_{sat} \exp\{v_l[P_{nuc} - P(T_0)_{sat}]/R_v T_0\} - P_{nuc}} \quad (1.2)$$

The equation 1.2 tells that there exists a critical bubble radius for liquid subjected to the tension and any nucleation site having radius more than the critical radius $(r > R_o)$ will eventually grow, and cavitation would occur. On the other hand, the nucleation site will collapse and disappear if the radius is less than the critical radius $(r < R_o)$. Since soft material consists of a solid phase (random fiber network) and a liquid phase (solvent), we can assume that the nucleation occurs solely in the liquid phase. Therefore, in terms of the nucleation formation, we can omit the elastic effect of the soft materials. From equation 1.2, the critical radius for soft materials only differ through the value of the surface tension. For pure water, typical surface tension is $72\ mN/m$. In the solution state, adding gelatin into the water reduces the surface tension $(\sim 60\ mN/m)$. However, when gelation starts and gel starts to form, then the surface tension increases $(\sim 80\ mN/m)$ and seems to vary as a function of the concentration [17]. For the same bubble nuclei to cavitate in soft material will then require higher tensile pressure to overcome higher surface energy compare to the pure liquid and will be discussed in detail in chapter 2.

Energetics of the Bubble Formation and Nucleation Rate

The above discussion of a stable bubble in tensile pressure does not answer how the critical bubble forms in the first place. Therefore, equation 1.2 is only the first of the three equations of CNT. The rest of the two equations deal with the bubble formation energy and the probability (nucleation rate) of that much energy to be available to form the bubble nuclei in the system within the time of observation.

The theory of homogeneous nucleation states that random thermal motion of atoms spontaneously creates energetic particles that leave the liquid phase and vaporize, thus form nucleation sites [1]. Church (2002) showed that the required energy for the nucleation increases with no bound at atmospheric pressure condition (P_{atm}) and nuclei immediately collapse [26]. A liquid subjected to negative (tensile) pressure, however, requires finite energy for spontaneous nucleation to occur, and it depends on the strength of the tensile pressure, surface tension, and temperature.

As described by Herbertz (1988), the nucleation energy (W_{nuc}) required to form a nucleus under tension consists of three work terms [27]: i. W_c, the work to create the cavity under far-field pressure (P_∞), ii. W_i, the work needed to establish the interface having surface tension (S), and iii. W_v, the energy attained by the formation of the vapor phase at bubble pressure (P_B),

$$W_{nuc} = W_c + W_i - W_v$$

$$= 4\pi r^2 S + \frac{4}{3}\pi r^3 (P_\infty - P_B) \tag{1.3}$$

Equation 1.3 implies that for a given tensile pressure ($P_\infty = P_{nuc}$) there exists maximum nucleation energy, $W_{nuc,max}$ ($setting\ \ dW_{nuc}/dr = 0$) which is required to form the bubble of the critical radius, $r = R_0$. Figure 1-3 shows the energy necessary for different far-field pressure. For any positive (compressive) pressure, the required energy is unbounded. However, for negative pressure, if the available energy is less than that of maximum energy ($W_{nuc,max}$), then the bubble will have a smaller radius than the critical radius and will eventually collapse. On the other hand, the bubble will grow and cavitate if the radius is bigger than the critical value. For simple homogenous liquid, the tensile pressure will suffice to cavitate, given that the condition is met as described above. The

tensile strength of the liquid is defined earlier as, $\Delta P = (P(T_0)_{sat} - P_{nuc})$. From equation 1.3, the critical energy of nucleation can be found from the tensile strength of the liquid considering the critical tensile pressure ($P_\infty = P_{nuc}$) and saturation pressure of the bubble content ($P_B = P(T_0)_{sat}$),

$$W_{nuc,max} = W_{cric} = 4\pi {R_o}^2 S + \frac{4}{3}\pi {R_o}^3 \Delta P \tag{1.4}$$

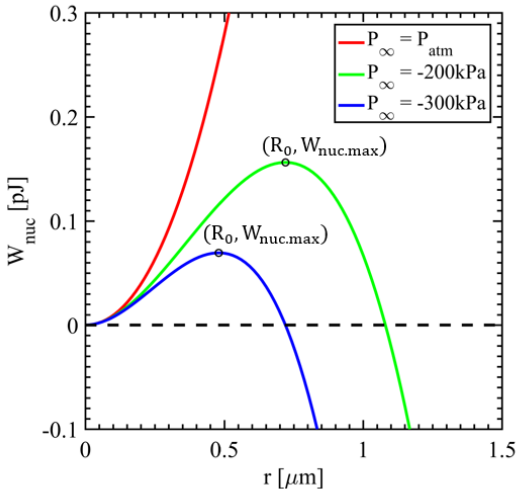

Figure 1-3 Nucleation energy as a function of nuclei radius

The tensile strength, described in equation 1.4, should be the same for soft materials compare to the pure liquid, since earlier we have postulated that the formation of nuclei solely occurs in the liquid phase. This is not the case, and as experimental observation shows, tensile pressure increases 175% from pure water to 1% [w/v] gelatin gel [17]. One contribution comes from the increased surface energy, as discussed in the previous sub-section, and another contribution, as we have postulated in this manuscript,

is due to the presence of the elastic random fiber network (RFN). In chapter 2, we have discussed and developed a theoretical model to include the effect of the RFN on the onset of cavitation in soft materials.

The final equation of CNT is required to evaluate the probability of deposition of W_{cric} within the time of observation. Gibbs number is defined as the ratio of the critical energy required to form a bubble nucleus and the kinetic energy of the molecules due to the stochastic thermal motion,

$$Gb = \frac{W_{cric}}{k_b T_o} \tag{1.5}$$

Where, k_b is the Boltzmann's constant, and the nucleation rate, J, is defined as the number of nucleation per unit volume per unit time as,

$$J = N\left(\frac{2S}{\pi m}\right)^{\frac{1}{2}} e^{-Gb} \tag{1.6}$$

Where N is the molecular number density per unit volume, and m is the mass of the molecule.

Single Bubble Dynamics

Most of the studies involving bubble dynamics in soft materials are inspired by the pioneering contributions of Lord Rayleigh, Plesset, and Prosperetti [4]–[7], [28], who have given us the necessary understanding of bubble dynamics. However, much of the earlier works were limited to the incompressible, inviscid fluid. It is after the advancement of computational power and more advanced numerical techniques; researchers started to study the viscous effects on bubble dynamics [29]. Extending those models for studying cavitation in soft materials remains challenging due to the complexity involved in fluid

(viscous) and solid (elastic) like behavior of soft materials [30], [31]. Based on the understanding of the inertial cavitation in water, few numerical tools were developed to study the cavitation phenomena in viscoelastic soft biomaterials [32]–[34]. Not to mention that most of these works made various approximations to keep the system of equations manageable [26], [35]–[41]. For example, compressibility was ignored or at most approximated to the first order in these approaches [39]. The incompressible approximation overestimates the collapsing pressure and is unable to capture the propagation of collapsing pressure pulse. Still, this approach is reasonable if one interested in bubble dynamics instead of cavitation damage.

In the next sub-section, a one-dimensional bubble dynamics equation will be summarized for the symmetric growth-collapse.

Spherical Bubble Dynamics (Symmetric Growth and Collapse)

First, we will introduce the incompressible Rayleigh-Plesset equation of the bubble dynamics. Consider a bubble of radius, $R(t)$, which is a function of time t, in a bulk liquid of time-varying pressure, $P_\infty(t)$ and constant temperature, T_o. Then for bubble pressure, $P_B(t)$, constant dynamic viscosity, μ_L, and constant density, ρ_L, the one-dimensional bubble dynamic equation is,

$$R\ddot{R} + \frac{3}{2}\dot{R}^2 = \frac{P_B - P_\infty}{\rho_L} - \frac{4\mu_L}{\rho_L}\frac{\dot{R}}{R} - \frac{2S}{\rho_L R} \tag{1.7}$$

Equation 1.7 is a second-order ordinary differential equation (ODE), which requires two initial conditions to be solved numerically. Initial condition $R(0) = R_o$ and $\dot{R}(0) = 0$ coincide with bubble growth from the critical nucleus. Initial condition $R(0) =$

R_{max} and $\dot{R}(0) = 0$ simulate bubble collapse from the maximum size. In equation 1.7, the bubble pressure is defined as,

$$P_B(t) = P_v + P_{go}\left(\frac{R(0)}{R(t)}\right)^{3k} \tag{1.8}$$

Where k is the polytropic constant, and P_v is the saturation vapor pressure. In chapter 3, the initial partial pressure of the non-condensable gas content, P_{go} will be discussed in detail.

Equation 1.7 neglects the compressibility effect and good enough to capture the bubble growth. However, a critical bubble of radius, R_o grows to its maximum size, R_{max} which is 2-3 times higher order in magnitude. The growth is followed by the violent collapse, which can produce pressure shock in the order of gigapascal [42]. To evaluate the high inward velocity of the bubble wall and to capture the formation of the pressure shockwave, compressibility needs to be incorporated into the equation 1.7. One approach is the first-order or linear approximation in the Mach number proposed by Keller and Miksis (1980) and given here from ref. [34],

$$\begin{aligned}\left(1-\frac{\dot{R}}{c}\right)R\ddot{R} + \frac{3}{2}\left(1-\frac{\dot{R}}{3c}\right)\dot{R}^2 \\ = \left(1+\frac{\dot{R}}{c}\right)\left[\frac{P_B - P_\infty}{\rho_L} - \frac{4\mu_L}{\rho_L}\frac{\dot{R}}{R} - \frac{2S}{\rho_L R} - \frac{\Sigma}{\rho_L}\right] \\ + \frac{R}{\rho_L c}\frac{d}{dt}(P_a - P_\infty)\end{aligned} \tag{1.9}$$

Where c is the speed of sound in the liquid and $P_a = P_B - \frac{4\mu_L\dot{R}}{R} - \frac{2S}{R} - \Sigma$. Equation 1.9 is the compressible and viscoelastic (Kelvin-Voigt) form of the Rayleigh-Plesset equation. The elastic contribution (Σ) is summarized in table 1-1 where G is the small

strain shear modulus, and R_{eq} is the bubble radius in a stress-free configuration. For bubble growth $R_{eq} = R_o$, and for collapse $R_{eq} = R(t \to \infty)$.

Table 1-1 Summary of the Elastic Term in Equation 1.9

Model	Elastic Term, Σ
Newtonian Fluid with no Elasticity	0
Linear Hookean	$2G\left[1-\left(\frac{R_{eq}}{R}\right)^2\right]$
Neo-Hookean	$\frac{G}{2}\left[5-4\left(\frac{R_{eq}}{R}\right)-\left(\frac{R_{eq}}{R}\right)^4\right]$

Shock-Bubble Interaction (Asymmetric Collapse)

When a bubble starts to collapse from its maximum size, asymmetry in the flow field may cause the bubble to collapse non-spherically. Geometric asymmetry (e.g., solid wall), as well as the shock-bubble interaction, leads to the formation of a reentrant jet (i.e., microjet) that penetrates the nearby surrounding medium with high kinetic energy and may cause substantial damage. The asymmetric collapse not only creates the microjet but also produces liquid hammer pressure of higher magnitude, which has equal or arguably more damaging potential [8], [37], [43], [44].

In this work, we have studied the symmetric collapse due to the shockwave interaction with the bubble. This type of collapse is particularly interesting for soft materials. In the medical treatment (i.e., shockwave lithotripsy) high magnitude pressure pulse is passed through the soft tissue, which may interact with the bubble. A controlled application of shock-bubble interaction may be utilized for several medical treatment procedures. In contrast, an uncontrolled shock-bubble interaction (e.g., blast-induced brain injury) may lead to severe tissue damage.

The shock-bubble interaction mainly depends on two characteristic times; i) shock passing-time, and ii) bubble collapse time. In the incompressible assumption, shock speed through the medium is infinite. Therefore, shock-induced bubble collapse is like the symmetric collapse (Rayleigh collapse), considering the instantaneous step increase in far-field pressure. On the other hand, if the shock passing time is comparable to the bubble collapse time, then the bubble collapses asymmetrically. The characteristic time of the bubble collapse can be defined as,

$$t_c = \frac{R_{max}}{\sqrt{(P_\infty - P_B)/\rho_L}} \tag{1.10}$$

Cavitation Damage

Cavitation induced damage to surrounding medium is characterized by, i) the formation of highly localized shockwave, ii) high strain rate deformation, and iii) formation of microjet followed by liquid-hammer pressure. The first two are typical phenomena of symmetric collapse, whereas the third one is the outcome of asymmetric collapse.

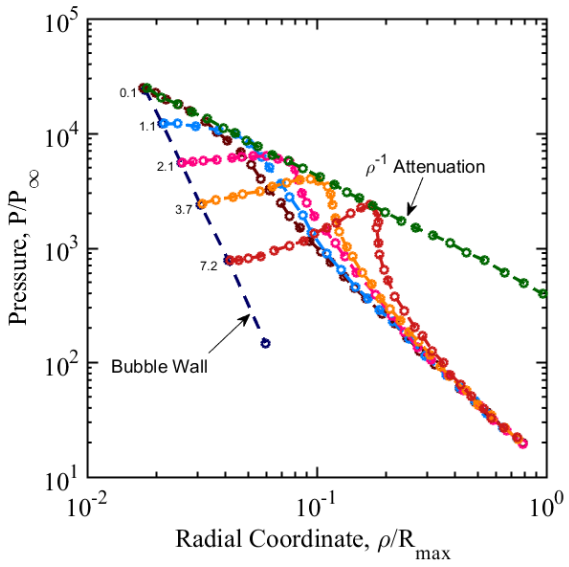

Figure 1-4 Pressure distribution from bubble wall after the collapse. Time associate with each curve is proportional to the time after the bubble attains the minimum size. Pressure magnitude attenuates as it propagates away from the wall as an inverse function of the radial coordinate [38].

Figure 1-4 is recreated from the work of Hickling and Plesset (1964), which shows how pressure pulse propagates through the bulk liquid after the collapse. The peak pressure of the pulse attenuates as an inverse function of the radial coordinate (ρ) as,

$$P_{peak} \approx \frac{100 R_{max} P_{\infty}}{\rho} \tag{1.11}$$

Equation 1.11 implies that at the close vicinity of the bubble wall, say at the $\rho = R_{max}$, the intensity of the collapsing pressure is, $P_{peak}\big|_{\rho=R_{max}} = 100P_{\infty}$. The surrounding medium not only experiences a highly localized pressure pulse but also must withstand high strain rate deformation. Estrada et al. (2018) evaluated the strain rate of the

collapsing bubble for the polyacrylamide gel in the order of $10^8 s^{-1}$. Since soft materials show rate-dependent behavior (e.g., viscoelastic), it is essential to quantify the damage accumulation through the bubble collapse and subsequent growths.

Johnsen and Colonius (2009) studied the asymmetric bubble collapse for varying shock strength. They have found that the microjet speed (V_j) can get as high as 0.4 to 0.8 times the speed of sound for the shock pressure 100 to 700 times of the atmospheric pressure. When this high-speed jet impacts the other side of the bubble, the liquid hammer pressure (P_h) is generated, and defined as,

$$P_h = \rho_L c \left| V_j - V_d \right| / 2 \tag{1.12}$$

Where V_d is the speed of the bubble wall opposite of the jet formation side. Johnsen and Colonius (2009) showed that P_h can get as high as the megapascal range for the shock range mentioned above.

Although this study is, in general, applicable to any soft materials (e.g., tissue, biomaterials, etc.), we have mainly summarized damage criteria for traumatic brain injury in table 1-2 and 1-3. We will discuss these injury criteria and will provide a quantitative parametric study of cavitation induced damage in soft materials in chapter 3.

Table 1-2 Stress-Based Injury Criteria

Reference	Injury Definition	Injury Criterion	Tolerance Level
Ward et al. (1980) [45]	Severe Brain Injury	Coup Pressure	$256\ kPa$
		Contrecoup	$-152\ kPa$
Kang et al. (1997) [46]	Severe Brain Injury	von Mises Stress	$11 - 16.5\ kPa$
Anderson et al. (1999) [47]	Mild DAI	Shear Stress	$8 - 16\ kPa$
Takhounts and Eppinger (2003) [48]	50% Probability of Contusions	Pressure Threshold	$-100\ kPa$
Zhang et al. (2004) [13]	25% Probability of mild TBI	Shear Stress	$6\ kPa$
	50% Probability of mild TBI	Shear Stress	$7.8\ kPa$
	80% Probability of mild TBI	Shear Stress	$10\ kPa$
Kleiven (2007) [49]	50% Probability of Concussion	von Mises Stress	$8.4\ kPa$
		Pressure	$65.8\ kPa$
		Minimum Pressure	$-55.1\ kPa$
Yao et al. (2008) [50]	Severe Brain Injury	von Mises Stress	$14.8\ kPa$
		Shear Stress	$7.9\ kPa$
		Coup Pressure	$256\ kPa$
		Contrecoup Pressure	$-152\ kPa$
Deck and Willinger (2008) [51]	50% Probability of mild DAI	von Mises Stress	$26\ kPa$
	50% Probability of Severe DAI	von Mises Stress	$33\ kPa$

Table 1-3 Strain-Based Injury Criteria

Reference	Injury Definition	Injury Criterion	Tolerance Level
Trosseille et al. (1992) [52]	Irreversible Brain Injury	Strain	0.15
Marguiles and Thibault (1992) [53]	Moderate to Severe DAI	Strain	$0.05 - 0.1$
Shreiber et al. (1999) [54]	Contusion	Logarithmic Strain	0.19
Viano and Lovsund (1999) [55]	Brain Injury	Average Strain x Strain rate	$36/s$
Takhounts and Eppinger (2003) [48]	Probability of Consussion	Strain Threshold	0.15
King et al. (2003) [56]	25% Probability of mild TBI	Strain Rate	$46/s$
		Strain x Strain rate	$14/s$
	50% Probability of mild TBI	Strain Rate	$60/s$
		Strain x Strain rate	$19/s$
	75% Probability of mild TBI	Strain Rate	$80/s$
		Strain x Strain rate	$24/s$
Zhang et al. (2004) [13]	25% Probability of mild TBI	Strain	0.14
	50% Probability of mild TBI	Strain	0.19
	80% Probability of mild TBI	Strain	0.24
Viano (2005) [57]	Concussion	Average Maximum Principal Strain	$0.35 - 0.45$
		Average Strain Rate	$60 - 80/s$
Kleiven (2007) [49]	50% Probability of Concussion	Maximum Principal Strain	0.21
		Maximum Principal Strain	0.26
		Principal Strain Threshold	0.1
		Strain Rate	$48.5/s$
		Strain x Strain Rate	$10.1/s$
Deck and Willinger (2008) [51]	50% Probability of mild DAI	von Mises Strain	0.25
		Maximum Principal Strain	0.31

Chapter 2

Cavitation Threshold Criteria for Soft Materials

Cavitation is considered one of the main driving factors that can potentially cause soft tissue damage [58]. The phenomenon has been studied in the medical treatments (e.g., lithotripsy) applications from the biological perspective and recently has gained its fair share of attention since it has been linked to the Traumatic Brain Injury (TBI) [14]. This lead to the study of cavitation bubble dynamics in soft tissue like materials (e.g., gelatin hydrogel), and the recent research on cavitation has intended towards the origin of nucleation theory as well as macroscopic behavior of cavitating bubble in soft materials [17]. Kang et al. (2018) used a novel drop-tower system to impact the gelatin samples and characterized critical acceleration to cavitation inception for various concentrations of gelatin gel. They suggested corresponding critical tensile pressure (P_T) for the onset of cavitation in gelatin and showed that there is a 175% increase from the water to 1% [w/v] gelatin. Evidently, soft materials tends to withstand more tensile load before the inception of cavitation damage. Hence, critical tensile pressure seems to be one of the most important parameters for the tissue damage study. In this context, we should mention the work of Gaudron et al. (2015), who modified the well-known Rayleigh-Plesset equation of bubble dynamics for a nonlinear viscoelastic model to study the bubble dynamics in soft materials [34]. Their study on the stability of bubble nuclei showed that elasticity plays a significant role in stabilizing much smaller nuclei by modifying the Blake radius [59]. It can be argued that higher activation energy is required than water to cavitate smaller nuclei in the soft materials. These two studies mentioned above dictated our motivation of this chapter to systematically study the threshold tensile pressure of cavitation onset in soft material. We have postulated that, i) due to the presence of the random fiber network (RFN) of gelatin gel, the critical flaw size (e.g., bubble nuclei of radius R_0) is comparable

to the pore size of the gel and ii) the threshold tensile pressure (P_T) is required for two consecutive works done by the bubble. First, a portion of the tensile energy is spent on activating the bubble nuclei and then rest of the energy is spent on overcoming the surface energy and the elastic energy imparted by the gel system for bubble to cavitate.

Recent studies on cavitation in soft biomaterials are based on the numerous pioneering works on cavitation in hyperelastic elastomers (e.g., rubber) [60]–[63]. We have found that one of the most frequently used cavitation onset criteria for visible bubbles to appear in a rubber block subjected to far-field triaxial tension is when cavity pressure (P_c) reach a critical value of $5G/2$ (G is the shear modulus for small strain) [15], [64], [65]. This onset criterion is based on the incompressible Neo-Hookean material model and applicable to nuclei size ranging from $0.5\ \mu m$ to $1mm$ (the range is only for rubber like material with higher elastic modulus and higher fracture toughness than gelatin hydrogel) [66]. In his "cautionary tale", Gent discussed the limitation of this onset criterion and suggested, i) for smaller nuclei surface energy might dominate the cavity growth, ii) at large deformation, real rubber-like materials do not follow the simple kinetic theory of rubber-like elasticity, and iii) a fracture based approach based on Griffith's fracture criterion [67] might explain the anomaly for smaller nuclei [68]. Indeed, Williams and Schapery (1965) considered the energy required for the cavities to fracture and showed that the required cavity pressure was as large as $9G$ for $0.5\ \mu m$ nuclei and even more for much smaller nuclei [69]. In the recent trend, more realistic material models have been used with "energy limiter" to study the cavitation in rubber [70], [71]. At the same time, Lopez-Pamies argued that cavitation needs to be studied as dynamic deformation where both inertia and viscosity play a significant role in bubble dynamics along with the material nonlinearity [72]–[74]. However, he discussed the poor agreement between theoretical and experimental observations and suggested that the microscopic

mechanism of rubber fracture needs to be incorporated for further study [75]. Indeed, all the references mentioned above did not consider the heterogeneity posed by the microstructure of the rubber material. The argument raises the question of the application of cavitation onset criterion ($9G \geq P_c \geq 5G/2$) for gelatin gel, or in general, for any biomaterials because of the inherent microstructure of hydrogel and rubber are quite different. The significant difference between rubber and biomaterials is that the microstructure of rubber is made of RFN of “flexible fibers/chains” having “entropic deformation” [76], whereas biomaterials have network of “semi-flexible fibers” having “enthalpy dominant deformation” [77]. Moreover, studies involved in cavitation in rubber considered presence of “vacuous cavity” while homogeneous nucleation theory considers the presence of nuclei is a spontaneous phase change phenomenon happens in the liquid phase (water) filled with the vapor and non-condensable gas under tension [1], [26], [78]–[80]. Therefore, considering gel system as a biphasic material where RFN is the solid phase and solvent (e.g., water) is the liquid phase, we can assume that the nucleation process is same as in the water alone and solid phase only interacts while the bubble grows. This assumption is the base of our second postulate mentioned in the previous paragraph. This approach simplifies the analysis by separating the contribution of tensile load to two consecutive events; first, to provide enough activation energy to nucleate a bubble and second, to overcome surface and elastic energy for bubble to grow.

However, the elastic contribution of the gelatin network on bubble growth is complicated to quantify. There are mainly three different approaches to study the mechanics of the RFN [81], [82]: Single fiber mechanics [83], [84], unit cell modeling [85]–[88], and construction of the 3-dimensional (3D) network [89]–[99]. The structure of the gelatin network itself is very complex [100]–[102] and depends on many factors, e.g.,

source of gelatin (bovine, porcine, etc.), manufacturing process and sample preparation [103], [104]. Moreover, 3D network generation requires substantial computational effort; therefore, we have adopted the “unit cell modeling” approach. In this approach, one needs to propose a unit cell having a finite number of fibers, followed by establishing a relationship between the fiber stretching (λ_f) and the unit cell stretching (λ_G). Then utilizing the experimental stress-strain (stretching) data we can use a curve fitting method to find the relevant properties of the fibers. We have seen successful implementation of the unit cell modeling approach in rubber elasticity with “flexible fibers/chains”. A 3-chain [105], [106], 4-chain [107], [108] and 8-chain [109], [110] models are the most frequently adopted unit cell models. Recently 8-chain model of Arruda and Boyce (1993) has been modified for “semi-flexible fibers” and used to describe mechanics of fibrin network and mussel byssal threads [111], [112]. Cryogenic-temperature scanning electron microscopy (cryo-SEM) observation shows that gelatin fibers form a d-periodic hierarchical structure similar to collagen fibril and connected via triple-helical gelatin strand at the crosslink [113]. Due to the similarity of collagen fibril and gelatin fiber we have used the unit cell proposed by Susilo et al. (2010) who studied the micromechanics of collagen based extra-cellular matrix (ECM). Experimental stress-strain data up to the gel failure is then used to find the fiber level ultimate failure stretch (λ_f^u) [114], [115].

The present work investigates the cavitation threshold tensile pressure for the gelatin gel system and the role of RFN on the bubble growth. The failure of the individual fiber is considered as the limiting criterion for cavitation onset. The strain energy gained by the RFN before the failure is used to calculate the tensile pressure. In the second approach, the critical energy release rate (G_c) is used as a fracture criterion considering gel as a homogeneous medium, and a comparison is drawn between the two approaches. This chapter is organized as follows. First, we have discussed in detail the

justification of our assumptions. The length scale involved in the gel system for bubble nucleation is presented and threshold tensile pressure (P_T) is defined. In the next section, mesh size (i.e., crosslink to crosslink fiber distant, ξ_0) is computed using the linear shear modulus (G) and critical flaw size (R_0) is proposed based on the pore size. Then a unit cell model is used to quantify the fiber properties, and the bubble growth mechanism is introduced to the unit cell failure. Lastly, a fracture criterion is formulated for the hyperelastic Ogden material model [116], followed by results and discussion sections.

Cavitation Threshold Tensile Pressure for Gelatin

In equation 1.4, we have shown the critical energy required for a bubble to form in the pure liquid. The critical tensile pressure for a bubble to form in the liquid is defined as P_{nuc}. Since critical tensile pressure for a bubble to cavitate in soft material (P_T) is significantly higher than P_{nuc}, we can define the extra tensile pressure as,

$$P_T = P_{nuc} + \Delta P_T \tag{2.1}$$

In the above equation, ΔP_T arises due to the bubble growth in the presence of the random fiber network and surface energy. Figure 2-1 depicts this scenario where gray background and blue fibers represent bulk liquid and fiber networks, respectively. Considering bubble only contains saturated vapor and no non-condensable gas ($P_{go} = 0$), then mechanical equilibrium at the formation of a bubble requires,

$$P_v = P_{nuc} + \frac{2S}{R_o} \tag{2.2}$$

We assume that, in this case, R_o is the reference configuration with stress-free surrounding medium (i.e., $R_o = R_{eq}$), hence there is no elastic contribution in equation 2.2. When a bubble starts to grow, strain energy is stored in the network, and at the

current configuration the mechanical equilibrium is established at the onset of cavitation in gel,

$$P_v\left(\frac{R_o}{R}\right)^3 = \Delta P_T + \frac{2S}{R} + P_{RFN} \tag{2.3}$$

Where, P_{RFN} is the pressure contribution from the strain energy density stored in the network until the bubble stretch ratio $(\lambda_B = R/R_o)$ reaches a critical value. In the above equation, we have considered vapor as an ideal gas with isothermal polytropic expansion (k=1). In terms of the bubble stretch ratio, equation 2.3 can be written for the extra tensile pressure as,

$$\Delta P_T = P_v\left(\frac{1}{\lambda_B}\right)^3 - \frac{2S}{R_o\lambda_B} - P_{RFN} \tag{2.4}$$

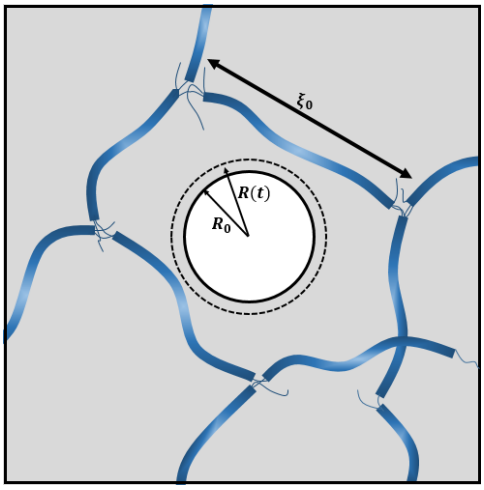

Figure 2-1 Bubble nucleation site growing within a random fiber network

Figure 2-2 plots equation 1.2 for the different surface tension of gelatin concentration. Data from the water-vapor saturation table is used for the other parameters at temperature, $T_o = 20^oC$. Kang et al. (2018) reported that the mean tensile pressure for water was $120kPa$ which corresponds to a critical radius of $1.2\ \mu m$ (figure 2-

2). Even for the same critical radius to cavitate in the gel system without considering the elastic contribution, the tensile nucleation pressure would be higher due to increasing surface energy (W_i) to overcome (horizontal dashed line in figure 2-2).

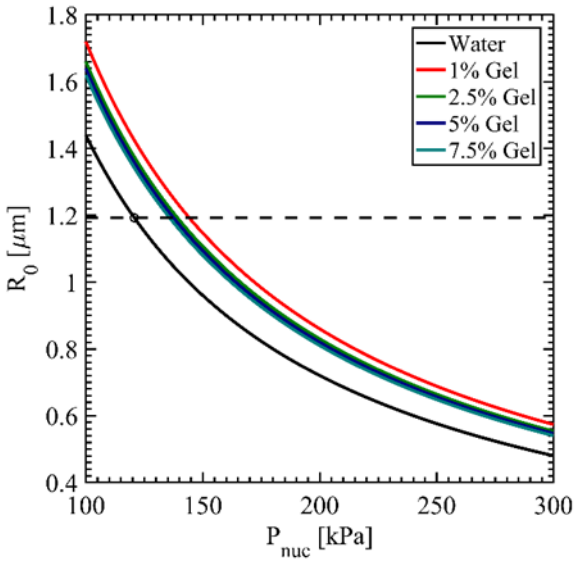

	Surface Tension, S [mN/m]
Water	72
1% Gel	86
2.5% Gel	83
5% Gel	82
7.5% Gel	81

Figure 2-2 Critical bubble radius as a function of the nucleation pressure from equation 1.2

To the best of our knowledge, until now, only Kang et al. (2018) reported the cavitation threshold tensile pressure (P_T) for different concentrations ($C\%\ [w/v]$) of gelatin gel (figure 2-3). In their work, "Knox gelatin" is solved with water in weight to volume ratio to prepare 1%, 2.5%, 5%, and 7.5% gelatin gels. In figure 2-3, the green dotted line indicates a 175% increase in threshold tension from water to 1% gelatin. The Blue dotted line is fitted with a nonlinear least square method ($R^2 = 0.93$) to show the increasing trend with gelatin concentration. From figure 2-3, the mean P_T varies from 188 to 228 kPa from 1% to 7.5%, which corresponds to R_0 of 0.9 to $0.7\ \mu m$ in figure 2-2. As discussed in the previous section, elasticity tends to stable much smaller nuclei. In the next sub-

section, we will discuss the presence of smaller nuclei from the microstructural point of view.

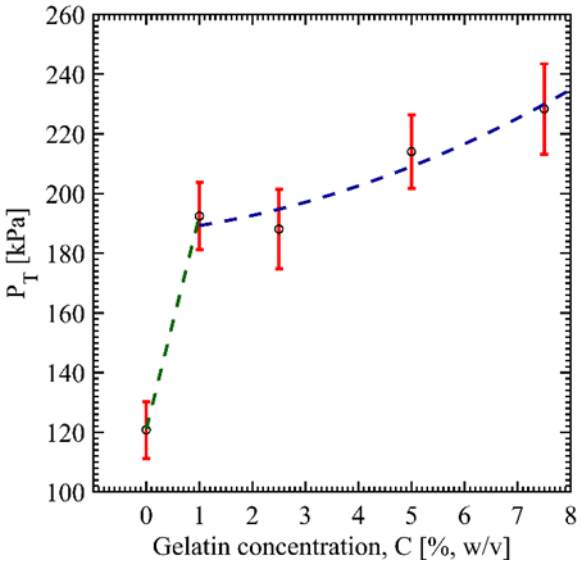

Figure 2-3 Experimental observation of the threshold tensile pressure for different concentrations of gelatin gel [17]. C=0 corresponds to pure water. (Vertical red error bar indicates the standard deviation)

Random Fiber Network of the Gelatin Gel

Marmorat et al. (2016) used the cryo-SEM imaging technique to observe the gelatin supramolecular structure. They showed that gelatin fibers are connected via the triple-helical gelatin strand at the crosslink. In low crosslink density, however, the distance between the crosslinks are large to allow the strands' natural tendency to recoil into fibrils (Figure 2-4). Those gelatin fibrils showed a well-known banded pattern with a periodicity of $64\ nm$ similar to the collagen fibril [117]. The theory of determining the mesh size based on the rubber elasticity [118] underestimated the mesh size observed by Marmorat et al. (2016). MacKintosh et al. (1995) proposed that the "semi-flexible"

network shows increased rigidity due to its secondary structure between the crosslinks and must be taken into consideration to determine the mesh size [119]. Considering the network consists of effective spring where effective spring constant is k_{ef}, then the small strain shear modulus is related to the mesh size as [113],

$$\xi_0 = \frac{k_{ef}}{G} \tag{2.5}$$

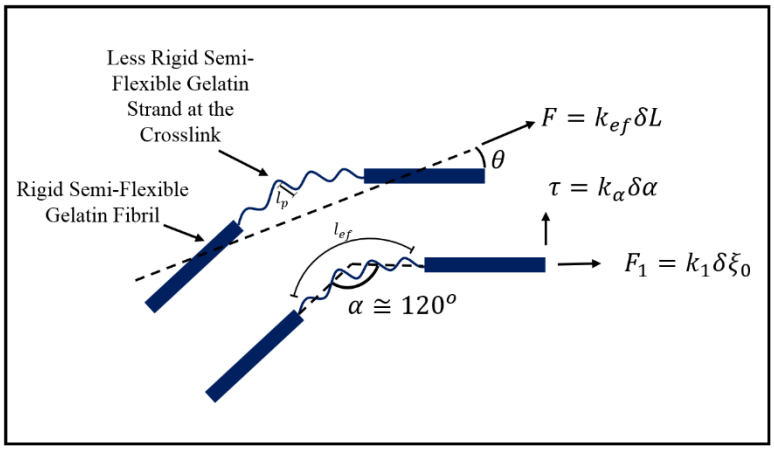

Figure 2-4 Typical crosslink of the gelatin fiber network. Individual fibers are crosslinked via the gelatin strand.

For small strain, the rigidity arises from the straightening of α angle of the gelatin strand at the crosslink. However, Gelatin fibril will deform as well for large strain and will be considered in later sections. From figure 2-4, for any force (F) applied to the crossling with effective spring constant (k_{ef}) will have two components; i. F_1 will stretch the gelatin strand with stretching spring constant k_1, and ii. torque τ will act to change angle α with angular deformation constant k_α. Treloar (1960) calculated the k_{ef} for polymeric chain and will be adopted here [120],

$$\frac{1}{k_{ef}} = \frac{\delta L}{F} = n\left[\frac{cos^2(\alpha/2)}{k_1} + \frac{l_p^2 sin^2(\alpha/2)}{k_\alpha}\right] \quad (2.6)$$

In the above equation, $n = l_{ef}/l_p$, is the amount of zigzag which is defined as the ratio of the effective length of the gelatin strand (l_{ef}) at the crosslink and the persistence length of the gelatin strand (l_p). The cryo-SEM observation showed that the statistical average crosslink angle is $\langle\alpha\rangle \cong 120^o$, hence $\langle sin^2\left(\frac{\alpha}{2}\right)\rangle = 0.75$ [113]. Considering crosslink deformation dominated by k_α for small strain and for an inextensible gelatin strand ($k_1 \gg k_\alpha$), we can drop the first term in equation 2.6,

$$k_{ef} = \frac{k_\alpha}{n l_p^2 \langle sin^2\left(\frac{\alpha}{2}\right)\rangle} \quad (2.7)$$

From Treloar (1960) and Marmorat (2016), the angular deformation constant is related to the persistence length and monomer unit length (l_0) as $k_\alpha = k_B T_o l_p/l_0$. Where k_B is the Boltzmann constant. Therefore, the effective spring constant is,

$$k_{ef} = \frac{4k_B T_o}{l_0 l_{ef} \langle sin^2\left(\frac{\alpha}{2}\right)\rangle} \quad (2.8)$$

There exist two limiting cases for the effective length (l_{ef}) of the gelatin strand (figure 2-4). For high-density crosslink, the gelatin strand will not be able to recoil to form fibril like superstructure. Therefore, fibers will be made of gelatin strand only, and the effective length will be, $l_{ef} \to \xi_0/2$. On the other hand, for low-density crosslinks, fibers will have enough strand to recoil, and gelatin fibril will form. Hence, the minimum gelatin strand effective length at the crosslink, which deforms in small strain, will be reduced. Since the minimum length would be two persistence length to form the crosslink bend, the effective length would be, $l_{ef} \to 2l_p$. From equation 2.5 and 2.8,

$$\xi_0 = \sqrt{\frac{8k_B T_o}{G l_0 \langle sin^2\left(\frac{\alpha}{2}\right)\rangle}} \qquad for\ l_{ef} \to \xi_0/2 \quad (2.9)$$

$$\xi_0 = \frac{2k_B T_o}{G l_0 l_p \langle sin^2\left(\frac{\alpha}{2}\right)\rangle} \qquad for\ l_{ef} \to 2l_p \qquad (2.10)$$

Equation 2.9 and 2.10 is the theoretical minimum and maximum limit of the fiber length, respectively [113]. The small strain shear modulus is measured for 5, 7, and 14% [w/v] of Knox gelatin gels using a piezoelectric cantilever measurement technique and reported in figure 2-5(a) from the ref. [121]. The black dashed line shows a linear fit with $R^2 = 0.99$. The shear modulus value is used in equation 2.9 and 2.10, and the mesh size is plotted in figure 2-5(b). The monomer unit length, $l_0 = 1.4\ \text{Å}$ and persistence length, $l_p = 2.7\ nm$ for gelatin strand is used from the ref. [113], [122]. The theory is validated by observing the SEM image of 3 different concentrations of gelatin gels. We have followed the procedure described in ref [17] for gelatin sample preparation. The detail of the sample preparation and the SEM imaging is given in the supplementary document. The SEM images are given in figure 2-5(c), and the measurement of the mesh sizes of 3, 5, and 7% [w/v] gelatin gels are plotted in figure 2-5(b) and compared with equation 2.9 and 2.10. It seems the limiting case for equation 2.10 is valid, which means gelatin fibrils are formed as the supramolecular structure in the fibers and crosslinks are connected by the gelatin strand.

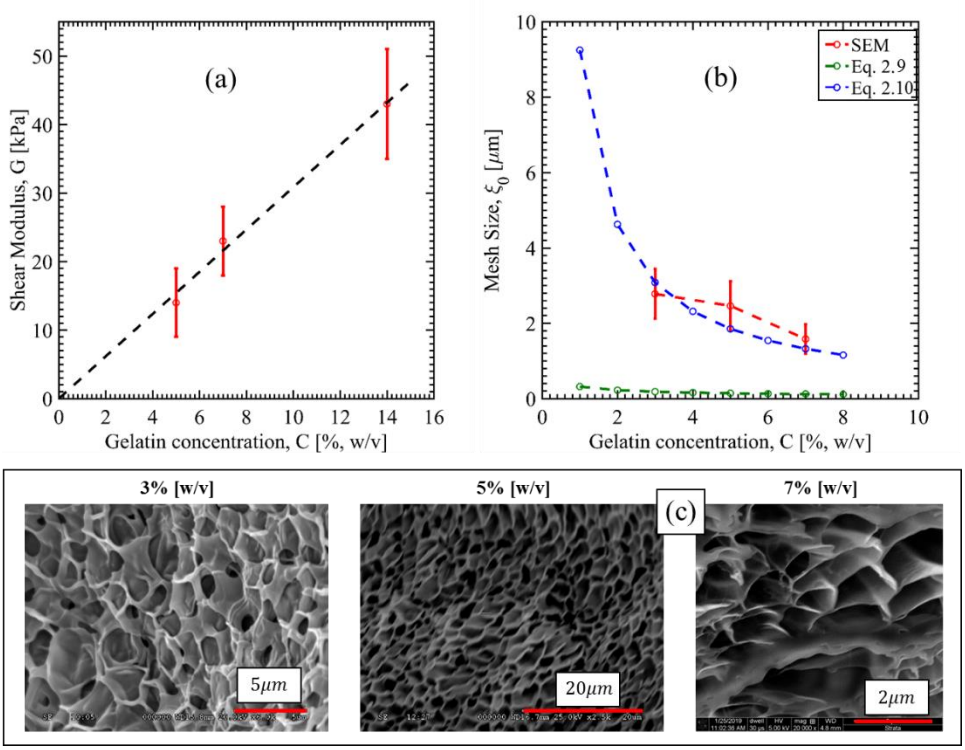

Figure 2-5 (a) Shear modulus, (b) fiber length observed from the SEM images and theoretical model (equation 2.9 and 2.10) fit, and (c) SEM images of different gel concentrations. (Vertical red error bar indicates the standard deviation)

The pose size is then measured using the Diameterj plugin with Fiji (Imagej2) software [123], [124]. The SEM image is first converted to an 8-bit binary image and then segmented using the 24 algorithms provided by the Diameterj. Each image is then analyzed, and the mean pore size is measured. Figure 2-6 shows an 8-bit SEM image, segmented image, and pose size measurement for 3% gel as a sample.

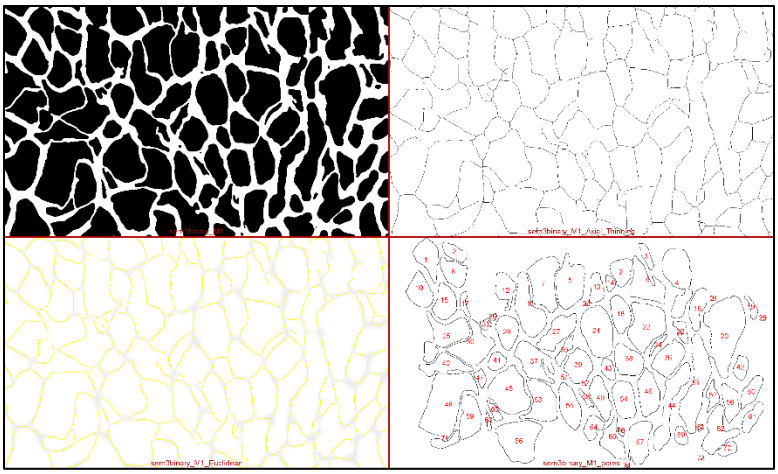

Figure 2-6 8-bit image of the SEM image of 3% gel (top left). Segmentation is done in two steps (top right and bottom left). Pore count and size measurement are shown (bottom right).

Figure 2-7 shows the pore size (A_p), and since ImageJ fits the pore size in an ellipse, we have shown the minor axis length (L_{MA}) of the pores in figure 2-8. As we have postulated in the previous section, a bubble nucleus of the critical radius (R_0) must be accommodated within a pore to cavitate under the tensile nucleation pressure (P_{nuc}). The maximum size of a sphere that can fit in an ellipse must have a radius that is half of the minor axis length. Therefore, in equation 1.2 we will use $R_0 \rightarrow L_{MA}/2$ for gel system to compute P_{nuc}.

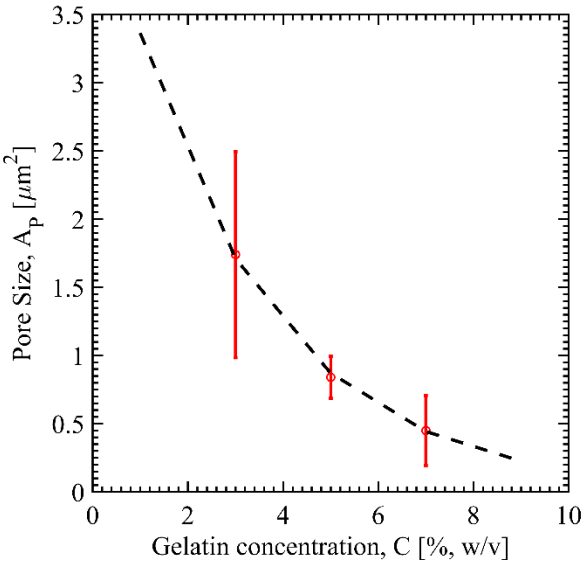

Figure 2-7 Pore area size measured by observing the SEM image of different gel concentrations. (Vertical red error bar indicates the standard deviation)

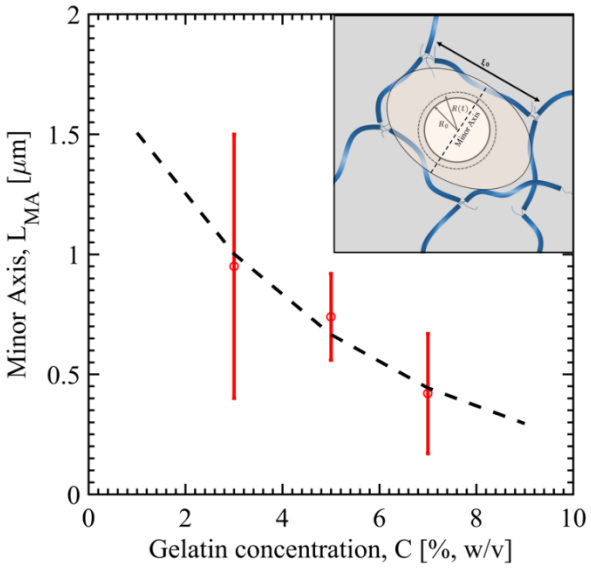

Figure 2-8 Minor axis length of the pore area. (Vertical red error bar indicates the standard deviation)

Strain Energy-Based Failure Criteria

Since $l_{ef} \rightarrow 2l_p \ll \xi_0$ we will assume that the crosslink to crosslink fiber is consists of the gelatin fibril only. From now on, we will use gelatin fibril length and mesh size interchangeably. To construct the gelatin network, we will replace the contribution of the gelatin strand with torsional spring at the crosslink with effective torsional spring constant, K_t (figure 2-10). Since gelatin triple-helical strands self-assemble into the secondary supramolecular structure as collagen fibril, which is modeled as semi-flexible fiber, we can model each gelatin fibril as such [93]. We used the word "fibril" for gelatin fiber to be consistent with the definition of the hierarchical structure of collagen micro-fibril, fibril, and fiber [125]. A semi-flexible fibril is defined such that its thermal persistence length is comparable to the fibril length, $L_P/\xi_0 \sim 1$. The persistence length of the gelatin fibril can be defined as the ratio between the bending rigidity and thermal energy, $L_P = E_f I_f / k_B T_o$, where E_f is the fibril Young's modulus and $I_f = \pi {d_f}^4/64$ is the moment of inertia of the fibril, respectively. The only material and geometric properties we need to compute the strain energy of the network is the Young's modulus (E_f), crosslink torsional spring constant (K_t), fibril length (ξ_0), and diameter of the fibril (d_f). Considering the gelatin fibril as elastic beam which resists stretching and bending, and crosslink as torsional spring, the strain energy of the network for any given configuration is defined as [93],

$$\begin{aligned} U &= U_S + U_B + U_T \\ &= \sum_{i=1}^{N_s} \left(\int_0^{\Delta\xi_0} F_f d\Delta\xi_0 \right)_i + \sum_{i=1}^{N_b} \left(\int_0^{\xi_0} \frac{M^2}{2E_f I_f} dx_f \right)_i + \sum_{j=1}^{N_t} \left(K_t \frac{{\Delta\theta_t}^2}{2} \right)_j \end{aligned} \tag{2.11}$$

In equation 2.11, N_s and N_b are the number of fibrils that contribute to the stretching strain energy (U_S) and bending strain energy (U_B), respectively. Crosslink

torsional strain energy (U_T) is due to the N_t number of crosslinks having rotational angles θ_t. The difference between the current and reference configuration is indicated by Δ, and $A_f = \pi {d_f}^2/4$ is the cross-sectional area of the fibrils. The stretching force is defined as, $F_f = E_f A_f(\exp(B_f \varepsilon_f) - 1)/B_f$, where B_f is a material parameter and the Green strain (ε_f) is calculated using the fibril stretching ratio as, $\varepsilon_f = ({\lambda_f}^2 - 1)/2$ [126]. M is the non-uniform (fibril length wise) transverse moment on the fibril due to bending (x_f is the fibril local longitudinal coordinate defined in figure 2-15).

Incorporating the bubble growth ratio (λ_B) into equation 2.11, we can compute the strain energy of the network. Ultimately, we will assume that the network failure strain energy is the work done by P_{RFN}. In the next sub-section, we will adopt a unit cell model to find fibril material and geometric properties. Then we will incorporate the bubble growth into the equation 2.11.

Unit Cell Model and Fibril Properties

In the unit cell modeling, we will fit the macroscale stress-strain data to the microstructural deformation of the RFN unit cell. For large strain, gelatin gel is proposed to behave like incompressible hyperelastic Ogden material [115]. The strain energy density function for the first order Ogden material in terms of principal stretches of gel (λ_{Gi}) in three coordinate directions ($i = 1,2,3$) is,

$$W_G = \frac{\mu_G}{\beta}(\lambda_{G1}^{\beta} + \lambda_{G2}^{\beta} + \lambda_{G3}^{\beta} - 3) \tag{2.12}$$

Where μ_G and β are material properties. Particularly β is the strain hardening parameter, and for gelatin, β is reported from ref [115] (plotted in figure 2-9). The small strain shear modulus is defined as, $G = \mu_G \beta/2$, and given in figure 2-5. For uniaxial tension, the deformation gradient tensor $\boldsymbol{F_G}$ is,

$$\boldsymbol{F_G} = \begin{bmatrix} \lambda_{G1} & 0 & 0 \\ 0 & \lambda_{G2} & 0 \\ 0 & 0 & \lambda_{G3} \end{bmatrix} \tag{2.13}$$

The incompressibility condition is met when $\det(\boldsymbol{F_G}) = \lambda_{G1}\lambda_{G2}\lambda_{G3} = 1$. For uniaxial tension in direction 1, let $\lambda_{G1} = \lambda_G$ and $\lambda_{G2} = \lambda_{G3} = \lambda_G^*$, then from incompressibility condition, $\lambda_G^* = 1/\sqrt{\lambda_G}$. The three principal values of the Cauchy stress ($\boldsymbol{T_G}$) is defined as,

$$T_{Gi} = -\tilde{p} + \lambda_{Gi}\frac{\partial W_G}{\partial \lambda_{Gi}} \tag{2.14}$$

Where $\tilde{p}$ is the pseudo-pressure term that is determined for uniaxial tension by setting, $T_{G2} = T_{G3} = 0$. The experimental data reported in ref [115] is for the first Piola-Kirchhoff (nominal) stress, which is defined as, $\boldsymbol{P_G} = det(\boldsymbol{F_G})\boldsymbol{T_G}(\boldsymbol{F_G}^T)^{-1}$. Therefore, the first Piola-Kirchhoff stress in direction 1 is (plotted in figure 2-9),

$$P_{G1} = \frac{2G}{\beta}\left(\lambda_G^{(\beta-1)} - \lambda_G^{(-\frac{\beta}{2}-1)}\right) \tag{2.15}$$

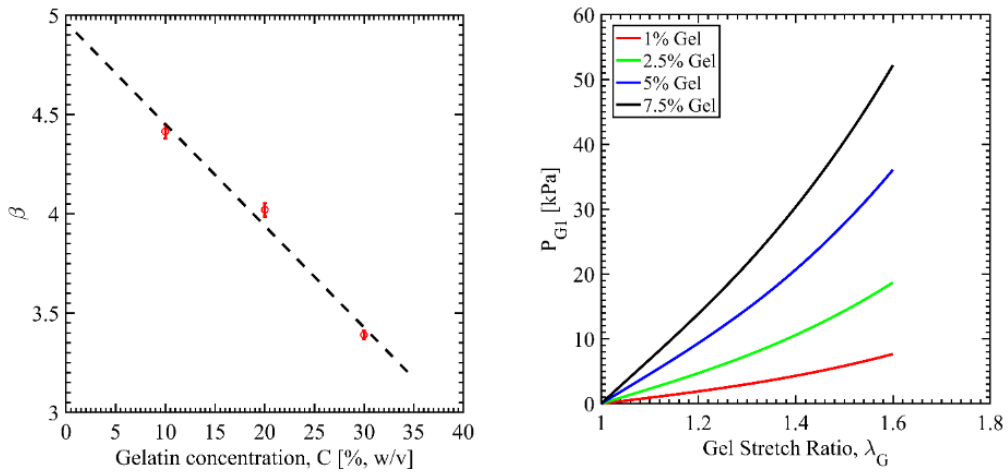

Figure 2-9 Strain hardening parameter (β) for gelatin from uniaxial testing (left) [115]. First Piola-Kirchhoff stress of gelatin gel as a function of the gel stretch [eq. 2.15] (right).

The three-dimensional microstructure of the gel system is represented by the unit cell in figure 2-10(a). The proposed unit cell assumes isotropic microstructure, and the angles are set to be $\psi = 45°$and $\phi = 35.26°$ for the unit cell to be symmetric in all principal coordinate directions. Other two geometric properties are fibril diameter (d_f) and length (ξ_0). The initial dimensions of the unit cell in three coordinate directions are,

$$L_{1,0} = 2\xi_0(1 + cos\phi cos\psi)$$

$$L_{2,0} = 2\xi_0(1 + sin\phi) \qquad \text{(2.16 a,b,c)}$$

$$L_{3,0} = 2\xi_0(1 + cos\phi sin\psi)$$

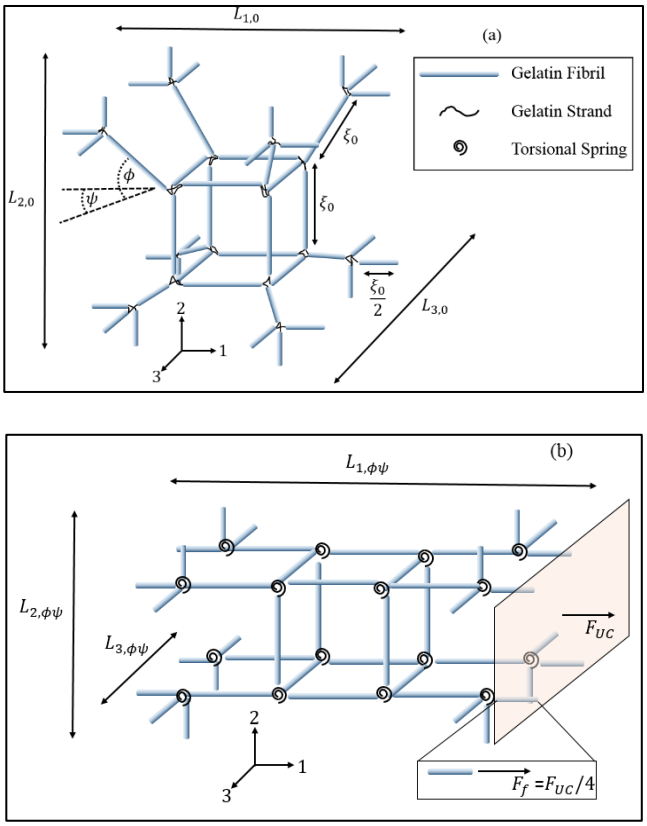

Figure 2-10 (a) Representative unit cell of the random fiber network of gelatin gel. (b) Uniaxial stretching until fibers align in the stretch direction due to the crosslink rotation.

Previously, we have assumed that the small strain is due to the strengthening of the crosslink angles. Therefore, oblique fibrils are aligned parallel to direction 1 before fibril level stretch (λ_f) imposed on the fibrils (figure 2-10(b)). The dimension of the unit cell when fibril alignment occurs are,

$$L_{1,\phi\psi} = 4\xi_0$$

$$L_{2,\phi\psi} = 2\xi_0 \qquad \text{(2.17 a,b,c)}$$

$$L_{3,\phi\psi} = 2\xi_0$$

The gel stretch is defined as,

$$\lambda_G = \frac{L_1}{L_{1,0}} \tag{2.18}$$

In the current configuration, the dimension of the unit cell in direction 1 is L_1. The gel stretch at the fibril alignment is,

$$\lambda_{G,align} = \frac{L_{1,\phi\psi}}{L_{1,0}} \tag{2.19}$$

Since fibril stretch occurs after fibril alignment, the fibril stretch is defined as,

$$\lambda_f = \frac{L_1}{L_{1,\phi\psi}} = \frac{\lambda_G}{\lambda_{G,align}} \qquad for\ \lambda_G \geq \lambda_{G,align} \tag{2.20}$$

The first Piola-Kirchhoff stress is defined as the force per initial unit area. Therefore, the force on the unit cell (F_{UC}) is,

$$P_{G1} = \frac{F_{UC}}{L_{2,0}L_{3,0}} \tag{2.21}$$

From figure 2-10(b), the force on the fibril (F_f) is one-fourth of the force on the unit cell, $F_f = F_{UC}/4$. From equation 2.11, we can decompose the stored strain energy of the RFN as crosslink deformation and fiber stretching (figure 2-11),

$$W_G(\lambda_G)V_U = \begin{cases} U_T = \sum_{j=1}^{N_t=16} K_t \frac{\Delta\theta_t{}^2}{2} & for\ \lambda_G \leq \lambda_{G,align} \\ U_S = \sum_{i=1}^{N_s=4} \left(\int_0^{\Delta\xi_0} F_f d\Delta\xi_0 \right)_i - U_T(\lambda_{G,align}) & for\ \lambda_G > \lambda_{G,align} \end{cases} \tag{2.22 a,b}$$

Where unit cell volume is $V_U = L_{1,0}L_{2,0}L_{3,0}$. Due to the symmetry, only one oblique fibril is shown in figure 2-11. The strain energy in equation 2.22(a) is due to the 16

crosslink ($N_t = 16$) rotation until $\lambda_{G,align}$, followed by 4 fibrils ($N_s = 4$) stretching until gel failure stretch, ${\lambda_G}^u$ (figure 2-11). K_t and E_f, $d_f$and B_f will be computed from equation 2.22 (a) and 2.22 (b) using nonlinear regression analysis, respectively. 60% strain (${\lambda_G}^u = 1.6$) is taken to be the failure criterion for the gelatin gels reported in ref. [115]. A similar failure strain is reported for collagen gels as well [93], [127]. Therefore, fibril level stretch is computed from equation 2.20 which is $\lambda_f = 1.26$. Collagen fibril yield strain and ultimate failure strain are reported to vary between 10-32% and 35-45% strain, respectively [128]. As Baumberger et al. (2006) observed that at low deformation rate, fiber network fails by crosslink disentanglement, and suggested that at higher strain rate network fails due to the individual fiber scission [129]. Therefore, in the uniaxial testing at the quasi-static stretching, we can conclude that gel fails via crosslink failure, and fiber does not attain its failure strain. However, bubble growth imposes high strain rate deformation in the surrounding medium, and we will assume that fiber failure strain (35-45%) is the main failure mechanism for bubble growth.

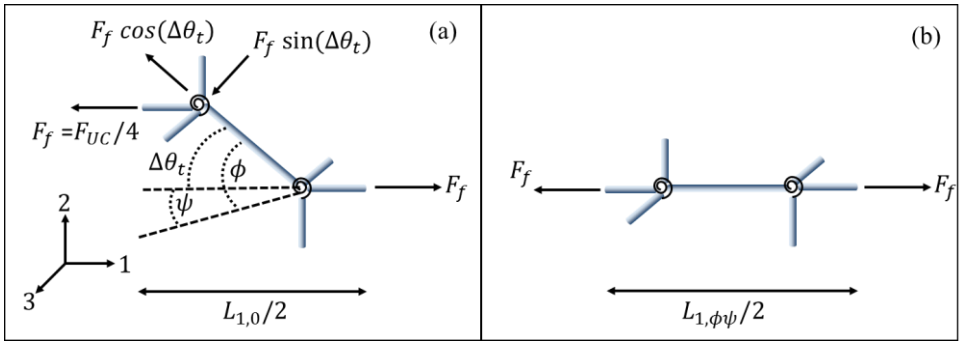

Figure 2-11 (a) one oblique fiber is shown at the beginning of the uniaxial tension. The strain energy stored until the fibers align in the stretching direction is due to the rotational strain energy of the crosslink. (b) fibers alignment is completed, and further stretching of the fiber store energy due to stretching only.

There are several studies where collagen fiber properties are measured by uniaxial stress-strain testing. However, we have not found, to our best of knowledge, any material property for gelatin fibril. Therefore, the unit cell model is developed, which can be utilized to estimate the gelatin fibril properties as the model can relate gel level properties to fibril level properties in close form. Since gelatin fibril and collagen fibril are similar in terms of their supramolecular structure, we can use collagen fibril properties as a guideline. Susilo et al. (2010) have summarized in detail the literature of collagen properties, and readers are referred to that for further reading [88]. We have found that the collagen fiber properties vary in a wide range of magnitude. One of the main reasons for this wide range is due to the hierarchical structure of collagen fiber (e.g., microfibril, fibril, and fiber). Diameter is one of the parameters that can distinguish the collagen fibril from the collagen fiber. Collagen fibril is said to have a diameter ranging from 20 nm to 400 nm, while collagen fiber may have a diameter greater than 400 nm [130]–[132]. Figure 2-12 plotted the gelatin fibril diameter for different concentrations using the unit cell model. The diameter range is seen to vary from 31 to 58 nm, and well within the discussed range given above. The decreasing trend of the diameter on the concentration is because the crosslink density increases with increasing concentration; therefore, there are fewer gelatin strands to recoil and form thicker fibrils. Cryo-SEM observation of increasing crosslink density showed a similar trend [113].

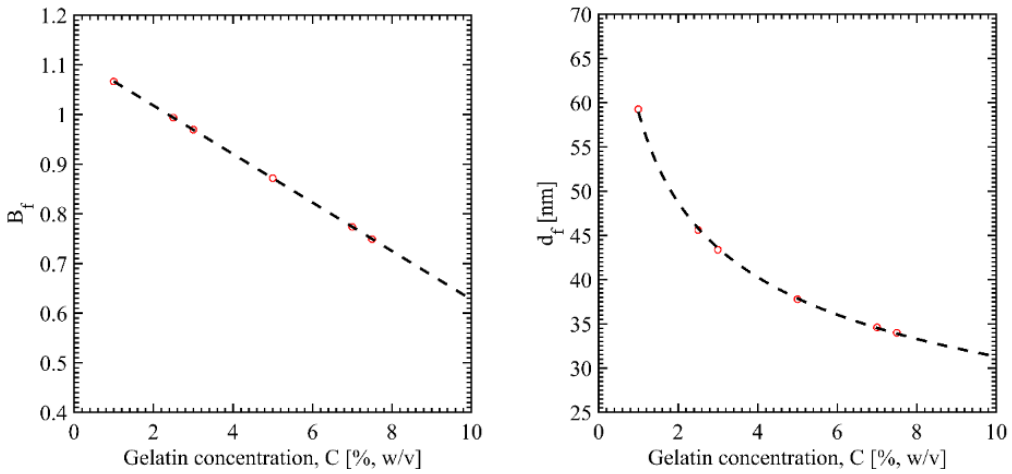

Figure 2-12 Non-linear material parameter (left) and diameter (right) of the fibers as shown for different concentrations of gel.

The range mentioned above for collagen fibril diameter (20 to 400 nm) corresponds to fibril Young's modulus from 32 MPa to 11.5 GPa [133]–[135]. For collagen fiber ($d_f > 400nm$) the modulus range is given to vary between 1.8 MPa to 1.2 GPa [88]. Figure 2-13 plotted the Young's modulus of gelatin fibril for different concentration of gelatin gel by utilizing the unit cell model and gel level material properties as described above. The Young's modulus range is shown to be within 400 MPa to 1.15 GPa and falls within the collagen fibril modulus range. The fibril parameters will be used in the next sub-section to quantify the network strain energy due to bubble growth.

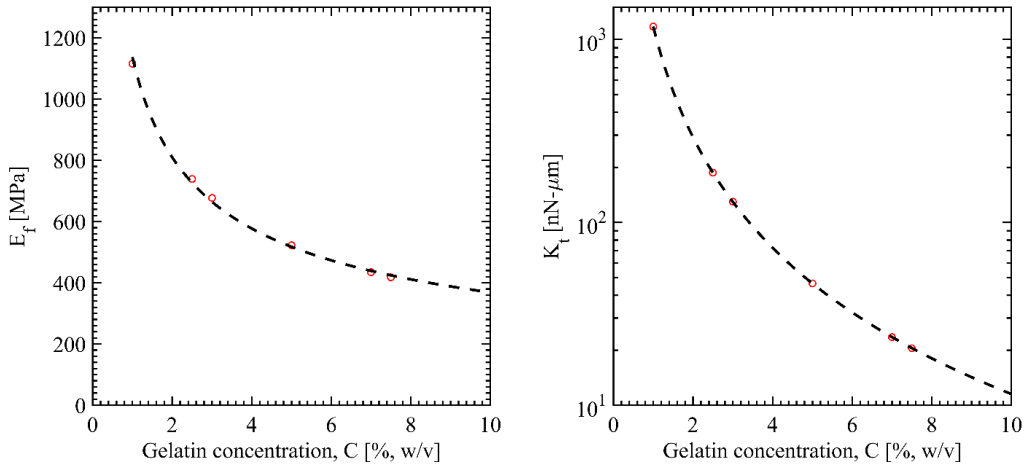

Figure 2-13 Young's modulus (left) of the fiber and crosslink torsional constant (right) of the network, as shown for different concentrations of gel.

Network Strain Energy due to the Bubble Growth

The network strain energy formulation shown in equation 2.11 can be utilized if we can establish correlations between the bubble growth ratio (λ_B) and three strain energy parameters, i.e. $\Delta\xi_o$, M and $\Delta\theta_t$. However, equation 2.11 is the superposition of three different modes of deformations (e.g., stretching, bending, and torsion). We will correlate the bubble growth to each mode of deformation separately. In doing so, a unit cell of the gelatin network is shown in figure 2-14(a) enclosing a bubble of radius R_0.

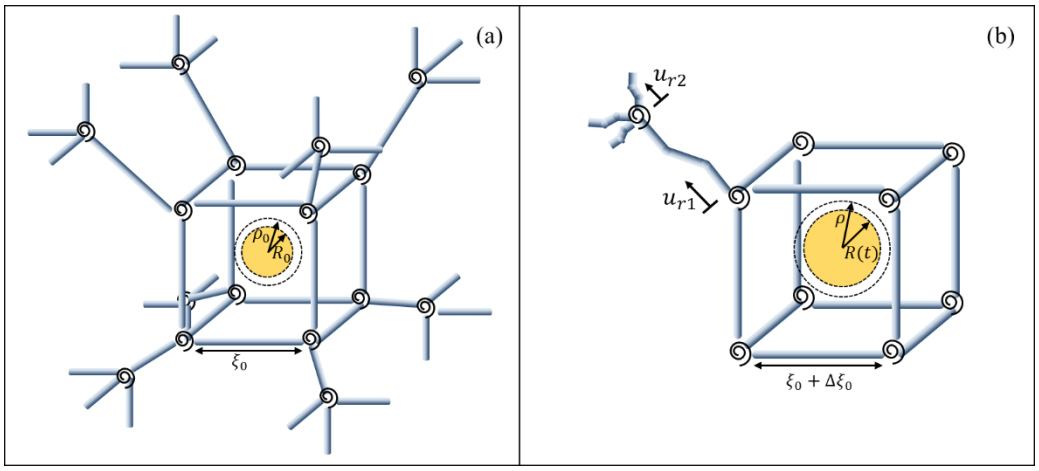

Figure 2-14 (a) Bubble nucleus enclosed by the unit cell. (b) bubble growth causing fibril stretching (cubic part) and buckling (oblique fibril).

Considering in a strain-free reference configuration, we assume the bubble center lies at the origin of a spherical coordinate whose radius is R_0. In the current configuration at the time t, the bubble radius is $R(t)$. Any material point initially at $\boldsymbol{x_0} = \rho_0 \boldsymbol{e}_\rho$ will be at $\boldsymbol{x} = \rho \boldsymbol{e}_\rho$ in the current configuration. The deformation gradient tensor of the surrounding medium due to bubble growth is [34],

$$\boldsymbol{F_B} = \begin{bmatrix} \frac{\partial \rho}{\partial \rho_0} & 0 & 0 \\ 0 & \frac{\rho}{\rho_0} & 0 \\ 0 & 0 & \frac{\rho}{\rho_0} \end{bmatrix} \tag{2.23}$$

The condition of incompressibility of the medium requires that $\det(\boldsymbol{F_B}) = 1$. Therefore, from equation 2.23, the radial stretch is, $\frac{\partial \rho}{\partial \rho_0} = (\frac{\rho_0}{\rho})^2$. Since $\rho_0 < \rho$ while bubble grows, the radial stretch decreases monotonically as a function of radial distance. Hence,

in figure 2-14(b), we have shown that all the oblique and end fibrils will experience buckling (only one corner is shown due to the ease of representation) except the fibril in the cubic portion of the unit cell. However, the buckling of semi-flexible filament is entropy dominant [77]. Since the strain energy formulation in equation 2.11 assumes the negligible entropic contribution, we will only consider the cubic portion of the unit cell that will contribute to the strain energy, and buckled fibrils are omitted.

Fibril Stretching Strain Energy

In figure 2-14(b), we have shown only the mode-I (stretching) deformation of the cubic cell within the unit cell. At the reference configuration, the initial volume of the liquid phase within the cubic cell is (figure 2-14(a)),

$$V_0 = \xi_0^3 - \frac{4}{3}\pi R_0^3 \tag{2.24}$$

Now, after an infinitesimal time increment, the bubble grows to $R(t)$ and displaces the surrounding liquid which eventually interacts with the network and increases the fiber length to $\xi_0 + \Delta\xi_0$. The volume of the surrounding liquid within the displaced cubic cell is.

$$V = (\xi_0 + \Delta\xi_0)^3 - \frac{4}{3}\pi R^3 \tag{2.25}$$

Assuming incompressibility of the liquid phase $(V_0 = V)$, we can equate equation 2.24 and 2.25 to establish the correlation between the incremental fibril length, $\Delta\xi_0$ and the bubble extension ratio, λ_B as,

$$\Delta\xi_0 = \frac{4}{9}\frac{\pi R_0^3}{\xi_0^2}({\lambda_B}^3 - 1) \tag{2.26}$$

The failure criterion for equation 2.26 is set to be, $\Delta{\xi_0}^u = \xi_0(\lambda_f^u - 1)$. The fibril failure stretch (λ_f^u) is varied between 1.35 to 1.45, as discussed in the previous section.

Fibril Bending and Crosslink Torsional Strain Energy

Since the liquid phase is displaced radially outward in all directions, we can simplify the bending shape of the fibrils and the crosslink rotation. From figure 2-15(a), looking upon a cross-sectional view of the cubic cell cutting by the A-A plane, we can superimpose a circle of radius, $R_{AA} = \sqrt{3}\xi_0/2$ on the fibril deformation due to bending. Geometric similarity requires that on the A-A plane the fractional area of the bubble growth (green shade) is related to the area (A_2) under the bended fibril (figure 2-15(b)). A deflection function $(y(x_f))$ is assumed for the fibril considering a simply supported beam with a constant distributed load per unit length (q) with local fibril coordinate system (x_f, y_f) is defined as well (figure 2-15(c)). The moment on the fibril is then defined as,

$$M = E_f I_f \frac{d^2y}{d{x_f}^2} = \frac{qx_f}{2}(x_f - \xi_0) \tag{2.27}$$

The first derivative of the deflection function evaluated at either end of the fibril ($x_f = 0 \; or \; \xi_0$) gives,

$$\Delta\theta_t = \frac{q{\xi_0}^3}{24E_f I_f} \tag{2.28}$$

Since, the area under the deflected fibril is,

$$A_2 = \int_0^{\xi_0} y dx_f = 0.207\pi R_o^2(\lambda_B^2 - 1) \tag{2.29}$$

Therefore, the distributed load on the fibril can be related to the bubble growth as,

$$q = \frac{24.84\pi}{\xi_o^5} E_f I_f R_o^2 (\lambda_B^2 - 1) \tag{2.30}$$

Equation 2.26, 2.27, 2.28, and 2.30 will be used with equation 2.11 to compute the network strain energy due to bubble growth until fibrils failed at λ_f^u.

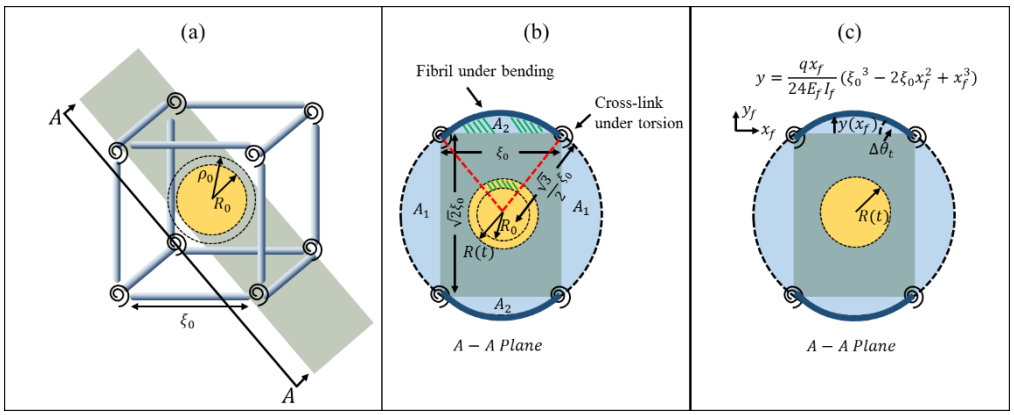

Figure 2-15 (a) a diagonal plane (A-A) is shown on which fibril bending occurs due to the bubble growth. (b) and (c) projection on the A-A plane showing geometric relation of bubble growth area and fiber bending.

Extra Tensile Pressure

Now that we have formulated the strain energy stored in the network due to the bubble growth, we can define the pressure contribution from the strain energy per unit volume as,

$$P_{RFN} = \frac{U_{cric}}{\Delta V_{cric}} \tag{2.31}$$

In the above equation, $U_{cric} = U(\lambda_f^u)$ and $\Delta V_{cric} = V_U - V_B^u$ is the difference between the volume of the unit cell and the volume of the growing bubble. The bubble volume is defined as,

$$V_B = \frac{4}{3}\pi R_o^3(\lambda_B^3 - 1) \tag{2.32}$$

At the critical condition, $V_B^u = V_B(\lambda_B^u)$. The fibril failure stretch and bubble failure stretch is related through equation 2.26 as,

$$\lambda_f^u = 1 + \frac{4}{9}\frac{\pi R_o^3}{\xi_o^3}({\lambda_B^u}^3 - 1) \tag{2.33}$$

Therefore, from equation 2.4, the extra tensile pressure is,

$$\Delta P_T = P_v\left(\frac{1}{\lambda_B^u}\right)^3 - \frac{2S}{R_o\lambda_B^u} - \frac{U_{cric}}{\Delta V_{cric}} \tag{2.34}$$

In the next section, we will develop the necessary formulation to quantify the extra tensile pressure based on the fracture theory.

Fracture Based Failure Criteria

In the previous section, we have formulated the criteria for the extra tensile pressure based on the failure of the RFN of the gel system. In this section, we will use the well-known Griffith's criterion for gelatin fracture due to bubble growth, considering gel as the homogeneous hyperelastic Ogden material. We know that elastic materials can store energy when deformed and can return to its reference configuration by spending that stored energy upon withdrawal of the loading. However, there is a limit on the stored energy beyond which fracture initiates and materials fail. Griffith's theorem states that a crack will propagate when surface energy is exceeded by the energy released due to new crack growth [136], [137]. The critical energy release rate (G_c) is the

material property that is used as the criterion for the material to resist fracture. Wire cutting tests are done to estimate G_c for gelatin gel and reported in figure 2-16 from ref. [115], [129], [138].

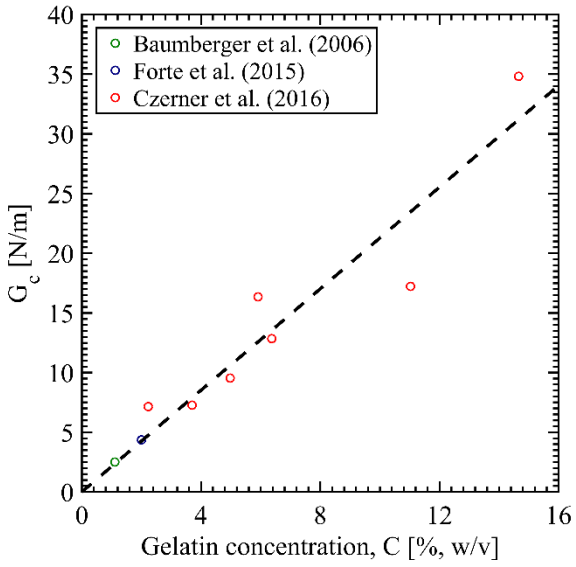

Figure 2-16 Critical energy release rate as a function of the gelatin concentration.

Several authors have modified the Rayleigh-Plesset equation of bubble dynamics for viscoelastic materials. The elastic term is added for linear Hookean, nonlinear Neo-Hookean, and strain hardening Fung models [33], [34], [58]. They have provided the procedure in detail, and readers are referred to them for further study. However, in this manuscript, we will develop the elastic contribution to bubble dynamics for the Ogden material model.

From equation 2.23, the deformation gradient tensor of the surrounding medium in spherical coordinate direction ($i = \rho, \theta, \varphi$) is,

$$\boldsymbol{F_B} = \begin{bmatrix} \lambda_{B,\rho\rho} & 0 & 0 \\ 0 & \lambda_{B,\theta\theta} & 0 \\ 0 & 0 & \lambda_{B,\varphi\varphi} \end{bmatrix} = \begin{bmatrix} \dfrac{\partial \rho}{\partial \rho_0} & 0 & 0 \\ 0 & \dfrac{\rho}{\rho_0} & 0 \\ 0 & 0 & \dfrac{\rho}{\rho_0} \end{bmatrix} \tag{2.35}$$

The incompressibility condition is applicable here as well which requires,

$$\frac{\partial \rho}{\partial \rho_0} = \left(\frac{\rho_0}{\rho}\right)^2 \tag{2.36}$$

Integrating the above equation and setting boundary condition at the bubble wall, $\rho = R(t)$ we get the reference coordinate in terms of the current coordinate of the material point,

$$\rho_0 = (\rho^3 - R(t)^3 + R_0^3)^{\frac{1}{3}} \tag{2.37}$$

From equation 2.14, the Cauchy stress tensor is,

$$\boldsymbol{T_G} = \begin{bmatrix} -\tilde{p} + \dfrac{2G}{\beta}\left(\dfrac{\rho_0}{\rho}\right)^{2\beta} & 0 & 0 \\ 0 & -\tilde{p} + \dfrac{2G}{\beta}\left(\dfrac{\rho}{\rho_0}\right)^{\beta} & 0 \\ 0 & 0 & -\tilde{p} + \dfrac{2G}{\beta}\left(\dfrac{\rho}{\rho_0}\right)^{\beta} \end{bmatrix} \tag{2.38}$$

In the above equation, we used $\lambda_{B,i}$ from equation 2.35 for the partial derivative of the strain energy density function. The pseudo-pressure term ($\tilde{p}$) in equation 2.14 and 2.38 is related to the hydrostatic pressure (p) as [34], [58],

$$\begin{aligned} p &= -\frac{T_{G,\rho\rho} + T_{G,\theta\theta} + T_{G,\phi\phi}}{3} \\ &= \tilde{p} - \frac{2G}{3\beta}\left[\left(\frac{\rho_0}{\rho}\right)^{2\beta} + 2\left(\frac{\rho}{\rho_0}\right)^{\beta}\right] \end{aligned} \tag{2.39}$$

Finally, the elastic contribution to the bubble dynamics is found by integrating the momentum equation from the bubble wall, $\rho = R(t)$ to $\rho \to \infty$ [33], [34], [58], [139],

$$\Sigma = \int_{R(t)}^{\infty} -\left[\frac{2T_{G,\rho\rho} - T_{G,\theta\theta} - T_{G,\phi\phi}}{\rho}\right] d\rho$$

$$= \int_{R(t)}^{\infty} -\frac{4G}{\beta}\left[\frac{{\rho_0}^{2\beta}}{\rho^{2\beta+1}} - \frac{\rho^{\beta-1}}{{\rho_0}^{\beta}}\right] d\rho \tag{2.40}$$

Setting $\gamma = \rho/\rho_0$ and using equation 2.37 we get,

$$d\gamma = \left(\frac{1}{\rho_0} - \frac{\rho^3}{\rho_0^4}\right) d\rho \tag{2.41}$$

Considering, $\lambda_{B,\theta\theta} = \lambda_{B,\varphi\varphi} = \lambda_B = R/R_0$, equation 2.38 becomes,

$$\Sigma = \int_{\lambda_B}^{1} -\frac{4G}{\beta}\left[\gamma^{-(2\beta+1)}\left(\frac{1-\gamma^{3\beta}}{1-\gamma^3}\right)\right] d\gamma \tag{2.42}$$

The above equation is integrated numerically using the quadrature theorem. The stored strain energy due to the elastic contribution is [58], [66],

$$U_\Sigma = \int_{R_0}^{R} 4\pi\Sigma\rho^2\, d\rho \tag{2.43}$$

The energy release rate per unit crack area is defined as $\partial \mathrm{U}_\Sigma/\partial A_c$, where $A_c = \pi R^2$ is the crack area. Applying Griffith's criterion of fracture on the energy release rate we get,

$$-\left(\frac{\partial U_\Sigma}{\partial A_c}\right) \geq 2R_0 f(\lambda_B) \tag{2.44}$$

Where $f(\lambda_B)$ is (using two dummy variables $(\zeta, and\ \eta)$),

$$f(\lambda_B) = {\lambda_B}^4 \frac{\partial}{\partial \zeta}\left(\zeta^{-3}\int_1^{\zeta} \Sigma \eta^2 d\eta\right)\Big|_{\zeta=\lambda_B} \tag{2.45}$$

At the critical condition, bubble fracture stretch is defined as, ${\lambda_B}^u = R_u/R_0$. Therefore, equation 42 can be numerically integrated until the fracture stretch by setting $f({\lambda_B}^u) = G_c/2R_0$ to find ${\lambda_B}^u$. We can then use equation 2.43 to find the total fracture energy at failure,

$$U_{\Sigma cric} = \int_{R_0}^{R_u} 4\pi \Sigma \rho^2 \, d\rho \tag{2.46}$$

Therefore, the extra tensile pressure can be defined in terms of the total fracture energy per unit volume of the bubble growth as,

$$\Delta P_T = \frac{U_{\Sigma cric}}{V_B^u} \tag{2.47}$$

Results and Discussion

Random Fiber Network

In developing the strain energy-based criterion for the onset of cavitation in soft materials, we have estimated the fibril and the network properties $(E_f, d_f, B_f, and\ K_t)$ from the gel level properties $(G\ and\ \beta)$ of the gelatin gels. The strain energy formulation of the network considers fibrils as an elastic beam, and they store energy by stretching and bending. This elastic beam model is justified since the persistence length of the fibril is much higher than the mesh size. Figure 2-17 shows the fibril thermal persistence length and how it compares to the mesh size. Collagen fibers, having mesh size in the micrometer range $(\sim 2\mu m)$ and thermal persistence length in the millimeter range $(\sim 10mm)$, often modeled as the elastic beam [93], [94]. $L_P/\xi_o < 2/\pi^{3/2}$ and $L_P/\xi_o \gg 1$

correspond to “flexible” and “rigid rod” type fibers, respectively [77]. A flexible fiber’s elastic response is due to the decrease in entropic conformation, and rigid rod-type fibers are modeled as beam theory. In between, there lies the definition of the “semi-flexible” fibers ($L_P/\xi_o \sim 1$) which shows elastic response by both stretching and bending. At low concentration and lower molecular weight, a semi-flexible fiber network shows *nonaffine* deformation, and fiber response is mainly due to bending. As concentration increases, the network tends to show more *affine* deformation, which is dominated by fiber stretching [98]. In the crosslinked network, the geometric persistence length is comparable to the mesh size, and fibers are considered semi-flexible.

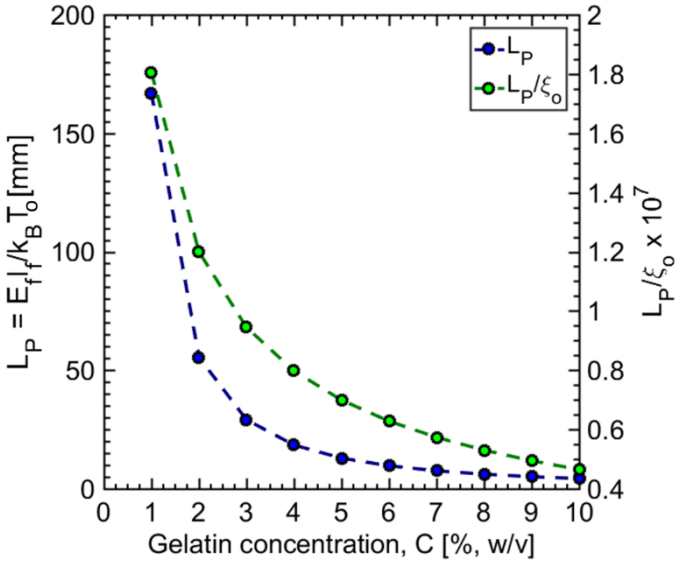

Figure 2-17 Persistence length of the gelatin fibers and the ratio between the persistence length and mesh size as a function of the concentration.

Figure 2-18 shows the strain energy of the network for different gel concentrations. The initial bubble radius is $1.2\mu m$ and grows until fibers fail at the 40% strain. The total strain energy is due to the stretching, both bending of the fiber and

crosslink rotational energy is few orders of magnitude lower than the stretching energy. For low concentration, although the bending energy increases slightly, the network deformation is mainly affine.

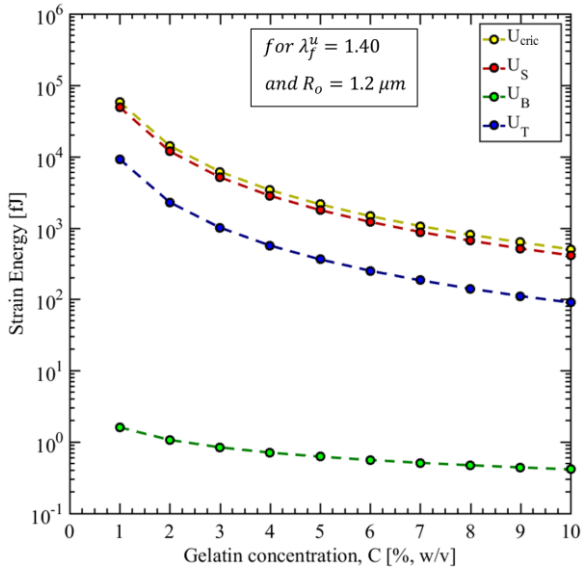

Figure 2-18 Strain energy of the network due to the bubble growth corresponds to $R_o = 1.2\mu m$ and $\lambda_f^u = 1.40$.

Critical Nucleation Pressure

Figure 2-19 plots the critical bubble size as a function of the gelatin gel concentration. The blue dotted line depicts the maximum bubble size that can be inscribed in the cubic portion of the unit cell model which is the half of the diagonal of the cube $(R_o = \xi_o/\sqrt{2})$. The SEM image observation of the network, however, indicates a much smaller *mean pore size* with a high standard deviation for the low concentration of the gelatin gels. The maximum bubble size that can be formed within the network is then limited by the pore size and defined as half of the minor axis length of the pores (red dotted line). The nucleation formation energy in pure liquid corresponds to the critical

nuclei size ($R_o = 1.2\ \mu m$) from experimental observation [17], and shown as the green dotted line.

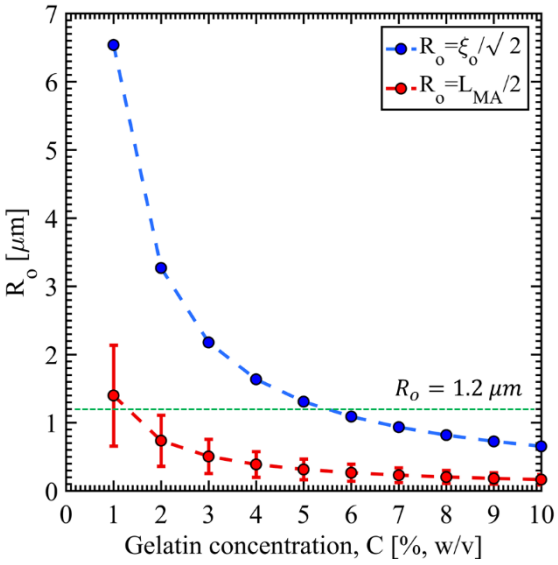

Figure 2-19 Critical bubble radius based on the unit cell model and pore size from the SEM image.

A random fiber network, having a large distribution of pore size, may have enough large pores where nucleation formation energy will only depend on the surface energy $(2S/R)$. However, the surface tension (S) value depends on various factors, such as the gel states (solution or gel), temperature, interface curvature, liquid inter-molecule affinity in the presence of the gelatin network [25], [140]. In figure 2-20(a) we have shown the surface tension of gelatin gel, both in solution and gel states and compared with water surface tension ($S_{water} = 72mN/m$) [17], [141], [142]. In the solution state, surface tension (S_{sol}) drops compared to the pure water while increases in the gel state (S_{gel}). The gelation process, however, starts by nonspecific hydrophobic interaction and the secondary supramolecular fibril forms [102]. The presence of the hydrophobic residues in

the polymeric chain may be the cause of decreased surface tension in the solution state. As the network starts to gain rigidity percolation, less and less of those hydrophobic residues are in close vicinity of the water molecule. Therefore, the liquid inter-molecular affinity increases and hence the surface tension rises in the gel state. Since, gelation process is a chemically dynamic equilibrium state, the coexistence of free-floating gelatin monomers (α-chain) and network is a typical condition in the gel system. Therefore, we have considered both surface tension (solution and gel) as the maximum and minimum limit for the nucleation. In figure 2-20(b) we have plotted the nucleation pressure for varying critical nucleation radius and represented as a function of the gel concentration. The vertical bars correspond to the maximum and minimum surface tension. While nucleation pressure for water is 120kPa for $R_o = 1.2\ \mu m$, it varies from 142 to 133 kPa for 1% to 10% gelatin. Considering there exists enough large pore size in the network comparing to the critical bubble size that of water, we will assume this nucleation energy as the base case.

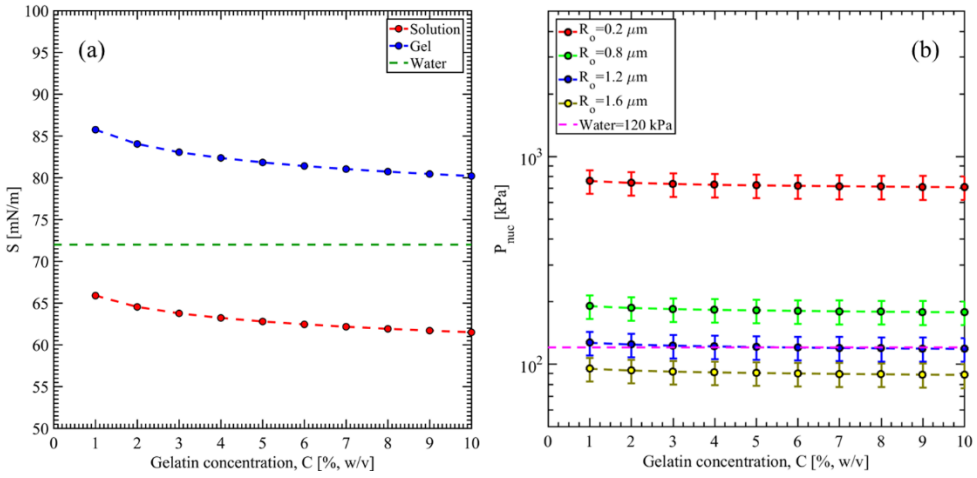

Figure 2-20 (a) Surface tension of gelatin gel in solution and gel states. (b) Nucleation energy required for different bubble sizes and gelatin concentration compared to pure liquid (i.e., water).

Critical Threshold Tensile Pressure

In this section, we have summarized the extra tensile pressure (ΔP_T) and the critical tensile pressure (P_T) on the onset of cavitation for the gelatin gels. Results from both the strain energy-based criteria (unit cell model) and the fracture-based criteria are presented. For the unit cell model the critical condition is set to the fibril failure stretch (λ_f^u) and varied between 35 to 45% strain. Bubble failure stretch (λ_B^u) is used for the fracture-based model and set to $f(\lambda_B^u) = G_c/2R_0$. Two cases are considered for both models, i) critical bubble radius is kept fixed for all gel concentration, and ii) varied based on the unit cell maximum ($R_o = \xi_o/\sqrt{2}$), and pore size maximum ($R_o = L_{MA}/2$). Results are compared with the theoretical range ($\Delta P_T\{max, min\} = \{9G, 5G/2\}$) for the extra tensile pressure and experimental data for the critical tensile pressure from the work of Kang et al. (2018). The vertical bars are used for the unit cell results to indicate the maximum, and minimum case corresponds to ($S_{gel}\ and\ \lambda_f^u = 1.45$) and ($S_{sol}\ and\ \lambda_f^u = 1.35$), respectively.

Figure 2-21(a) shows the extra tensile pressure for case (i). Both the model predicts extra tensile pressure within the theoretical range for the given gel concentration. For low concentration, ΔP_T does not depend on the critical radius but varies in a wide range for higher gel concentration. $9G$ curve well predicts at the low concentration and overestimates as the concentration increases. $5G/2$ curve does not predict the extra tensile pressure at the low concentration as experimental observation suggests [15]. The unit cell model coincides with the theoretical maximum curve for the low concentration. As the concentration increases, the fiber length (ξ_o) decreases and the unit cell volume decrease as well. For the same bubble radius, the slope of the ΔP_T tends to reduce as the fiber failure strain is reached earlier, and less and less strain energy is required for

the bubble to grow unconditionally. For the fracture model, the gel critical energy release rate linearly increases with the gel concentration and hence, shows an increasing trend. Figure 2-21(b) plotted the extra tensile pressure for case (ii), where R_o is a function of gel concentration. Two values of R_o are considered as mentioned earlier. $R_o = L_{MA}/2$ is the lower limit of the maximum possible bubble based on the pore size distribution, and extra tensile pressure happens to coincide with the maximum limit given by $9G$ curve. As the maximum limit is based on smaller bubble nuclei with higher surface energy, $R_o = L_{MA}/2$ is more conservative and overestimates the critical tensile pressure. On the other hand, $R_o = \xi_o/\sqrt{2}$ is based on the maximum possible bubble size that can fit in the cubic portion of the unit cell. $R_o = \xi_o/\sqrt{2}$ condition when used in the unit cell model predicts the most moderate values of the extra tensile pressure.

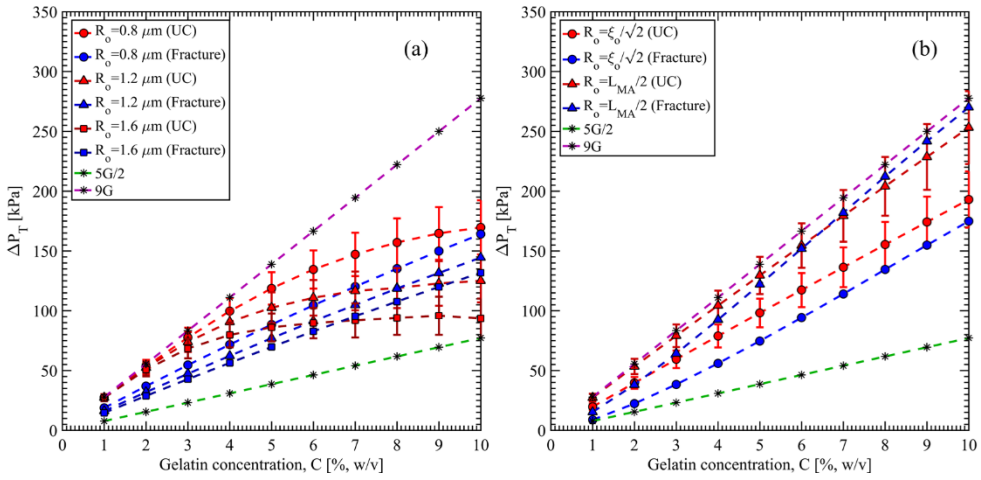

Figure 2-21 Extra tensile pressure for (a) fixed critical radius for different concentrations of gel, (b) varying critical radius. (UC=unit cell model, Fracture=fracture-based model)

Threshold tensile pressure is plotted and compared with the experimental data for the case (i) and (ii) in figure 2-22 and 2-23, respectively. Both unit cell and fracture-based model results are shown. For case (i), the best fit is provided by the $R_o = 1.2\mu m$

and can predict the critical tensile pressure for a wide range of the gel concentration for both models. For case (ii), $R_o = \xi_o/\sqrt{2}$ can predict the critical tensile pressure well for the gel concentration from 3 to 7%. $R_o = L_{MA}/2$ overestimates the critical tensile pressure for both models, as discussed earlier.

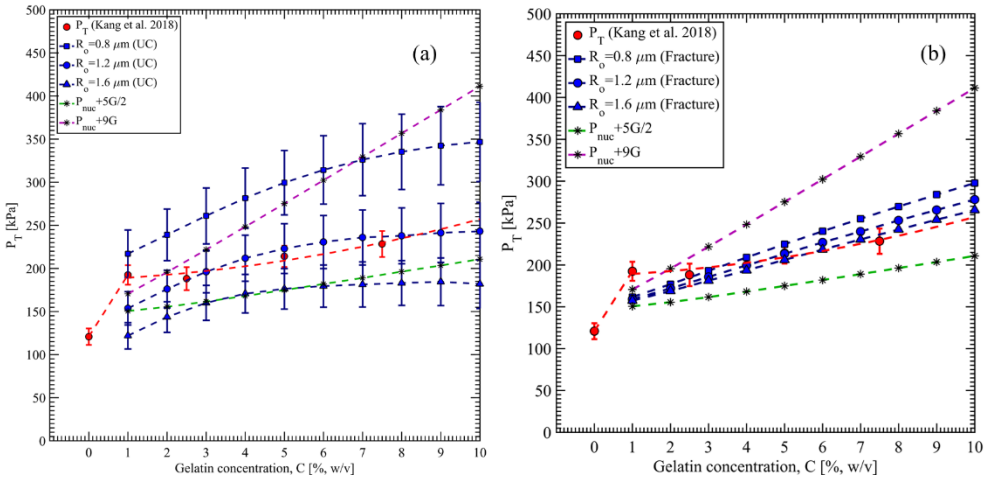

Figure 2-22 Threshold tensile pressure for fixed critical bubble radius for different gel concentrations. (a) unit cell model and (b) the fracture model.

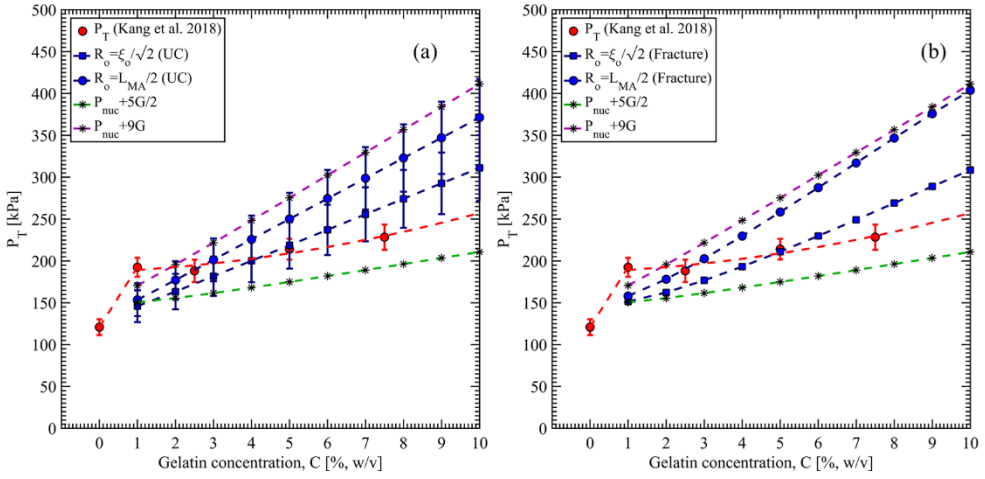

Figure 2-23 Threshold tensile pressure for variable critical bubble radius for different gel concentrations. (a) unit cell model and (b) the fracture model.

In this chapter, we have developed a theoretical framework to estimate the critical tensile pressure for cavitation in soft materials. Gelatin gel has been used for modeling purposes since it has various applications in the biomechanics field. Multifunctionality, less toxicity, and less biodegradability are few reasons for which gelatin gels are being used for tissue engineering and tissue mechanics. In the first part of this chapter, we have evaluated the gelatin network topology and then estimated the fiber properties by proposing a unit cell model. A bubble-network interaction is introduced, and strain energy-based failure criteria are then proposed. A fracture-based model is developed as well, and critical tensile pressure is evaluated. As we have postulated, the nucleation pressure in gelatin is comparable to that of water. A large distribution of the pore size is the basis of this hypothesis. There exist enough large pores that can activate nucleation sites in the range of $\sim 1.2\mu m$. The critical tensile pressure is well predicted by both unit cell and fractured based model for the critical bubble radius, $R_o \sim 1.2\mu m$. However, both models underestimate the critical tensile pressure for 1% gel. Since the network rigidity percolation transition happens at the 1% gelatin, an affine network model is not adequate [17], [143]. Just after the network rigidity percolation, there exists a nonaffine domain. Nonaffine network elasticity is bending dominated and not considered in our proposed model [98]. The nonaffinity is the measure of the heterogeneity of the deformation. Including the degree of the nonaffinity into the network-model, may improve its prediction for the low concentration gels. On the other side of the spectrum, we have a high concentration of the gelatin gel (~10%). As the thermal persistence length decreases with increasing concentration, the fibers are more entropic (flexible filament) than enthalpic. Cryo-SEM image observation showed that at the higher crosslinked network of the gelatin, the fibers are unable to recoil and form secondary structures [113]. Since the crosslink density increases with increasing concentration, fibers need to be

modeled as entropic. There are several entropic fiber models well discussed in the literature, such as the Gaussian, inextensible worm-like-chain (WLC) model, etc. We have not considered this approach since it is beyond the scope of this work.

Chapter 3

Cavitation Induced Damage in Soft Materials

Hydrodynamic cavitation phenomena have been studied for a long time since it has the potential to cause damage to structural and biological materials [1]–[7]. Recently the topic has gained its importance as it has implications to mild traumatic brain injury (mTBI) [9]–[14], micro-rheology [15]–[17], drug delivery [18]–[21], medical treatment (i.e., lithotripsy) [22]–[24], etc. Typically, when a soft material is under the critical hydrostatic tensile pressure, then tiny pre-existing stable bubbles (~ μm) start to grow and become visible size (~mm). The growth is then followed by collapses and rebounds until a new mechanical and thermodynamic equilibrium is reached. It is the first violent collapse that is identified as the most damaging since it produces a higher pressure pulse upon collapsing. Additionally, the surrounding medium also experiences high strain rate and shear deformation [17]. Several experimental and numerical studies have indicated cavitation occurrence in cerebrospinal fluid (CSF) as well as deep in the brain tissue [10]–[12]. Particularly the coup and the contrecoup regions are more likely to experience cavitation damage when subjected to blast wave or impact [144]–[146]. The complex fluid-structure interactions between the skull, CSF, and tissue indicate that several pressure pulses are propagating back and forth in those regions. Therefore, after the initial growth, when the bubble collapses from its maximum size, it is subjected to a far-field pressure higher than the critical tensile (positive) pressure. Since, in general, any tissue damage is induced by the collapsing cavity, we are particularly interested in the collapse pressure. As indicated in [147], the intensity of bubble collapse mostly depends on the far-field pressure, partial pressure exerted by the gas content, and material properties (e.g., viscosity, elasticity, and surface tension). In the present work, we have performed several numerical simulations varying the magnitude of the far-field pressure,

the partial pressure of the non-condensable gas content, and material properties. Then, we have summarized their influence on soft material damage. To correlate the cavitation collapse to the material damage, we have proposed a parameter called *efficiency of cavitation damage* based on the work of Thiruvengadam (1963), which quantifies the intensity of material damage to the intensity of collapse. In other words, the efficiency of cavitation damage can be defined as the ratio of the energy deposited to the surrounding medium to the energy released by the bubble collapse. We further extend the model to separately identify the damage intensity associated with the volumetric and shear deformation while maximum collapsing pressure is used to define the intensity of collapse. Each of the variable parameters is nondimensionalized, and the functional dependency of the efficiency of cavitation damage on these parameters is shown as the proposed scaling law.

In this chapter, the range of the parameters is limited to the events involved in the mTBI. However, the analysis and adopted methodology are general and can be extended to any range. The range for the far-field pressures is selected based on several previous studies on mTBI. According to the Conventional Weapon Effect Program (CONWEP), 50 to 1000 kPa blast shock overpressure can be considered for mTBI [148]. In contrast, Taylor (2014) used 360 kPa to be within the threshold of lung damage. Interestingly cavitation was predicted due to impacts and blast within the overpressure limit mentioned above, and some reported clusters (clouds) of bubbles of 1-3 mm in diameter in the contrecoup region through the experimental observations [9], [17], [144]–[146]. In addition to this, all of them reported high-pressure spike due to the cavitation bubble collapse ranging from 690-1450 kPa (gauge). For the detail of the cavitation inception mechanism in the brain, readers are referred to Refs. [149] for further study. It is important to note here that Ward (1980) [45] suggested a brain injury threshold of 235

kPa (gauge) for intracranial pressure, while Zhang (2004) indicated that deviatoric (shear) energy density of 200 Jm^{-3} should be considered as injurious. Therefore, we vary the far-field pressure from 50 to 200 kPa (gauge), keeping the value below the injury threshold proposed by Ward. By doing so, we consider no damage is done before the collapse and would like to find out whether the collapsing event alone can induce damage to the surrounding material. In this manuscript, we consider cavitation in soft materials modeling them as the rate-dependent homogenous viscoelastic material. The material properties are varied that are of relative importance as the biological soft materials. The ranges for these material parameters are discussed in detail in the results section.

Since the objective of the present work is to quantify the material damage, we developed a computational fluid dynamics (CFD) tool to simulate the compressible-multiphase fluid with added viscoelasticity. One of the robust commercially available solvers currently available is called “Fluent” [150], which can simulate compressible multiphase fluid. Currently, to the best of our knowledge, there is no available model in Fluent that can be used to simulate viscoelastic materials. Using “User Defined Functions (UDF),” the viscoelastic constitutive model is incorporated into the main tool [151]. We introduce the extra stress tensor for the added elasticity of soft materials to the momentum equation as a source term following the works of [152], [153]. The underlying physics of compressibility is more complex when added with viscoelasticity [154]–[157]. We have followed the work of Bollada [155] in this article. The present manuscript is structured as follows. In the next section, we develop the cavitation damage model. The following section shows the numerical simulation procedure, which first discusses the simulation scenario followed by the numerical method and initial simulation setup, respectively. Next, the result and discussion section summarize the outcome in detail. Finally, the article is concluded with the findings and prospects.

Cavitation Damage Model

A head-system (skin, skull, CSF, Tissue) experiences complex fluid-structure interaction under the influence of blast wave propagation (figure 3-1). The pressure profile of a shockwave can be approximated by the Friedlander wave (inset of figure 3-1(a)) and consists of a compressive shock front, which is followed by a tensile rarefaction wave. Since the acoustic wave propagation speed is higher in bone than CSF and tissue, the information of blast wave reaches to the contrecoup region earlier through the bone than through the later materials. Figure 3-1(b) depicts this scenario in detail. When the shock front arrives at position 2 through the air, the coup region (position 1) experiences a rarefaction portion of the blast wave. This tensile pressure may be the cause of the cavitation in this region. However, the stress wave already arrives at position 2' through the brain tissue while the contrecoup region (position 3) experiences stress wave much earlier. Figure 3-1(b) summarizes the acoustic impedance values for relevant materials, which is defined as the ratio of the acoustic pressure to the particle velocity [9]. It is an important intrinsic property of the material that is used to determine the fraction of sound that is transmitted through an interface of dissimilar materials. As figure 3-1(b) shows that when stress wave propagates through a medium of higher acoustic impedance to lower acoustic impedance, then it is reflected as a rarefaction (tensile) wave to the former medium. Since the acoustic impedance is higher for the brain tissue than the CSF (tabulated in figure 3-1(b)), the contrecoup region of the brain tissue may experience rarefaction waves when stress waves reflected from the interface and cavitation may occur (position 2').

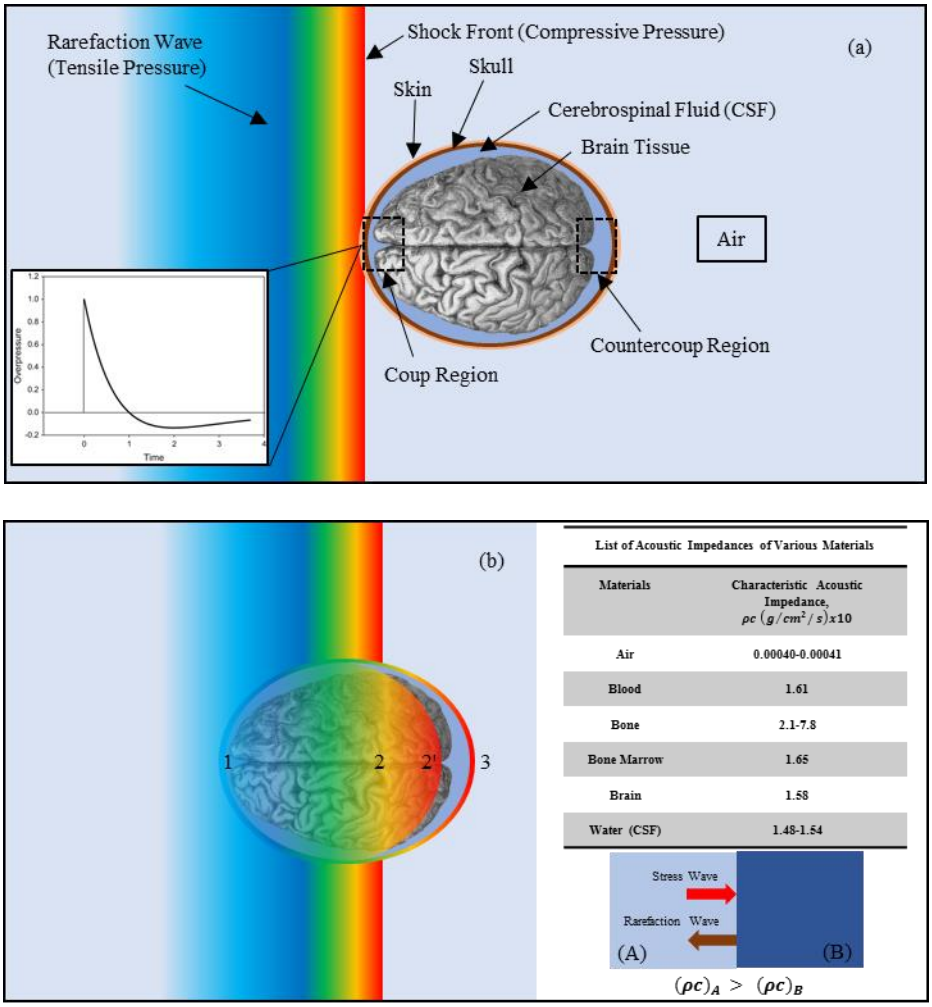

Figure 3-1 Complex fluid-structure interaction in the head system due to the incident shockwave. (a) shows the overall scenario, while (b) shows how differential wave propagation speed through the different materials dominates shock-head interaction.

Figure 3-2 (top) shows the time evolution of the bubble wall. In figure 3-2 (bottom), when a bubble nucleation site experiences tensile pressure, it grows (a-c), which is followed by the first collapse (c-e) and subsequent growths and collapses (e-f and so forth). In the present work, the initial conditions for the simulations coincide with the snapshot (c) given by figure 3-2(bottom). The detail of the initial setup for the

simulations is discussed in section 3. The compressive far-field pressure for which cavity collapses is taken to be 50 – 200kPa. This far-field pressure can be thought of as the incident shock wave overpressure or the pressure wave that reflects back and forth from the coup to the contrecoup regions. The simulations run through until after the first collapse (c-f) and capture the first collapse event (e). The initial bubble radius (R_{max}) is set to be 0.5mm for all the cases. R_{eq}^{*} is the non-dimensional stress-free bubble radius defined as, $R_{eq}^{*}(t \to \infty) = R_{eq}/R_{max}$. The intensity of collapse is defined by the collapsing pressure experienced at $\rho/R_0 = 1$ when the bubble collapses (e) where ρ is the radial position in a spherical coordinate from the center of the bubble. The energy deposition to the material is also measured at $\rho/R_0 = 1$, which is defined in more detail in the next paragraph.

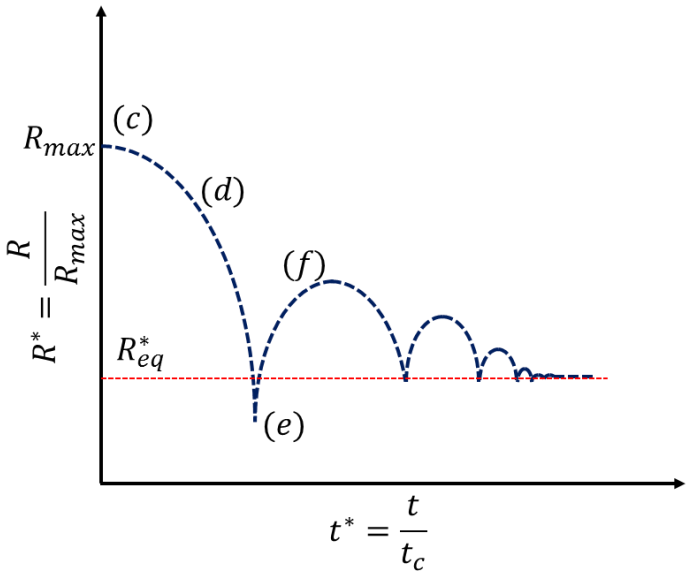

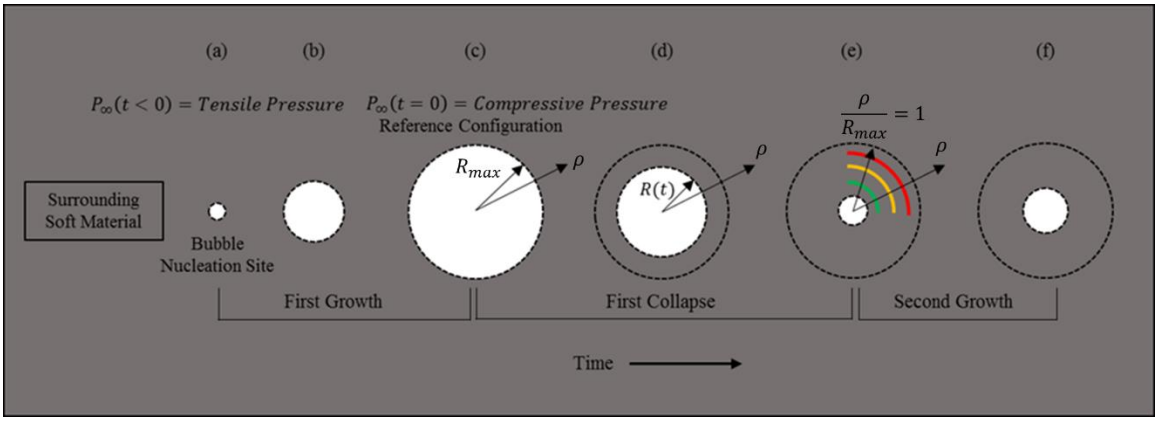

Figure 3-2 Snapshots of bubble wall motion. Bubble nucleation site grows under the critical tensile pressure (a-c) and attains the maximum size (c). The cavity collapses due to the step increase of far-field pressure (c-e) and grows again (e-f). This fluctuation continues until new mechanical and thermodynamic equilibrium is reached.

The efficiency of cavitation damage can be defined as indicated by Thiruvengadam (1963) as,

$$\eta = \frac{I_D}{I_c} \tag{3.1}$$

Where, I_D and I_C are defined as the intensity of damage and intensity of bubble collapse, respectively. The dimension of these two parameters is the energy rate per unit area. In his definition, Thiruvengadam defined intensity of damage as how much energy can be absorbed by the material per unit area due to the erosive forces that generated from the cavity collapse. In our case, equation 3.1 should be considered as the ratio between the damage accumulated on the surrounding material due to the shearing or volumetric energy deposition and the energy released by the collapse of a single bubble. For the shearing energy deposition, Taylor (2014) suggested that the high-stress level along with the associated deformation must be considered for soft material damage threshold and defined the deviatoric (shear) energy per volume as, $E_{shear} = \int tr(\boldsymbol{T}{:}\,\dot{\boldsymbol{\epsilon}})dt$, where $\boldsymbol{T}$ is the deviatoric stress tensor and $\dot{\boldsymbol{\epsilon}}$ is the rate of deformation tensor. Similarly, to quantify the volumetric response, the isotropic energy per volume is defined as $E_{iso} = \int P\, d\rho_L/\rho_L$, where P is gauge pressure (positive gauge pressure gives compressive isotropic energy and negative gauge pressure gives isotropic tensile energy) and ρ_L is the density. Therefore, the intensity of damage (for both shear and isotropic energy) is defined with the initial maximum bubble radius (R_{max}) and the collapse time(t_C) as

$$I_D = \frac{R_{max}E}{t_C} \tag{3.2}$$

Where E could be both E_{shear} and E_{iso}. The definition of $\boldsymbol{T}$ and $\dot{\boldsymbol{\epsilon}}$ require detailed discussion and will be given in the next section. However, without the loss of generality, we adhere to the definition of the intensity of collapse given in [147] as,

$$I_c = \frac{P_{peak}^2}{\rho_L c} \tag{3.3}$$

Where, P_{peak} is defined as the maximum collapse pressure (all pressure values are absolute unless otherwise mentioned) at $\rho/R_0 = 1$ and $t = t_c$. The term in the denominator $\rho_L c$ is defined as the acoustic impedance with material density ρ_L and sound speed c. It is important, at this point, to mention that the intensity of collapse greatly depends on the maximum collapse pressure which is a function of far-field pressure (P_∞), partial pressure (P_{g0}) exerted by non-condensable gas content, elasticity (shear modulus G_{kv}), viscosity (μ_{kv}) and surface tension (S) [147]. Based on the above discussion, a scaling law for cavitation damage in soft materials can be proposed as,

$$\eta = \frac{I_D}{I_c} = f\left(\frac{P_\infty}{P_{atm}}, \frac{P_{g0}}{P_\infty}, Wei, Re, We\right) \tag{3.4}$$

Where, Weissenberg number, $Wei = \tau_{kv}\frac{\dot{R}_c}{R_{max}}$ and retardation time, $\tau_{kv} = \frac{\mu_{kv}}{G_{kv}}$

Reynolds number, $Re = \frac{\rho_L \dot{R}_c R_{max}}{\mu_{kv}}$

and, Weber number, $We = \frac{\rho_L \dot{R}_c^2 R_{max}}{2S}$

Where, $\dot{R}_c$ is the maximum collapse velocity of the bubble wall. The approximated maximum collapsing velocity is given by Rayleigh as, $\dot{R}_c = \sqrt{2P_\infty R_{max}^3/3\rho_L R_c^3}$ assuming no bubble content (vacuum cavity) and inviscid fluid, which overestimates the maximum collapse velocity (R_c is collapsing radius). Therefore, we consider $\dot{R}_c$ to be directly calculated from the simulations which happen to coincide with $t/t_c \sim 0.7$ instead of the $t/t_c = 1$. The reason behind this is that the bubble first starts to

accelerate inward and decelerates to zero velocity at the time of the minimum radius. The bubble content (a mixture of vapor and air) and the restraining force of the elasticity always act against the bubble wall motion and cause the deceleration. However, we have excluded the gas diffusion effects from the above formulation since gas diffusion is expected to be insignificant during the short period of the bubble collapse time. This assumption is based on the Plesset-Hsieh criteria, which stated that a bubble of maximum radius of 1 mm or less would have a collapse of violent nature, whereas a larger bubble will collapse adiabatically and produce less intense collapsing pressure [35].

Numerical Simulation Procedures

Problem Description

Bubble collapse from out of equilibrium is considered since for any tensile pressure ($\Delta P = P_{sat} - P_{nuc}$) nucleation site with a radius greater than the corresponding critical radius (R_o) will initially grow and followed by collapse due to a step increase of far-field pressure (P_∞) [1], [25]. In this context, far-field pressure can be thought of as secondary shockwave overpressure or pressure that is reflected from the dynamic fluid-structure interaction between the skull, CSF, and brain tissue. It is evident from the previous studies that any microscale nucleation site grows to 1-3mm in diameter within the range of shock overpressure for mTBI. We consider $R_{max} = 0.5mm$ for all simulations as the maximum radius after initial growth. The maximum radius (occurs at simulation time, $t = 0$) is characterized by the zero interface wall velocity($\dot{R} = 0$) and out of mechanical equilibrium, that is bubble pressure does not satisfy Laplace relation, $P_B(t = 0) \neq P_\infty + 2S/R_{max}$. Therefore, initial bubble pressure at maximum radius is defined as, $P_B(t = 0) = P_v + P_{g0}$. The partial pressure contribution of vapor (P_v) is taken to be 3.4 kPa

(at $T_o = 300\ K$) for all cases and the initial partial pressure of gas content is given by Estrada (2018) as, $P_{g0} = (P_\infty + 2S/R_{max} - P_v)(R_{eq}/R_{max})^3$ [15]. Where, R_{eq} is the equilibrium radius of the bubble when surroundings are stress-free (for $time \to \infty$). The ratio (R_{eq}/R_{max}) can be found from the experimental observations as done in [16], but in our case, the value is taken to be an independent parameter to quantify the partial pressure of gas content. Once P_{g0} is calculated, the volume (mole) fraction of the gas content can be found from, $\alpha_g = P_{g0}/P_B$, which is required to define the vapor-air mixture (VAM) phase for the bubble in *Fluent*. Figure 3-3 shows how the two-dimensional axisymmetric domain was prepared.

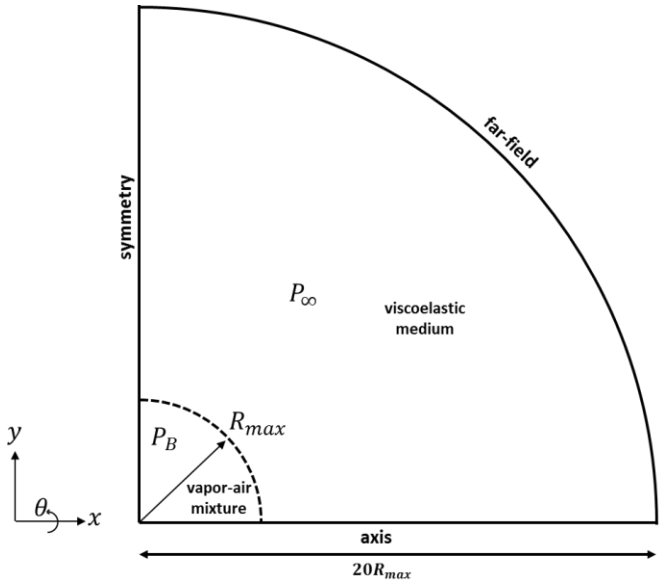

Figure 3-3 Axisymmetric domain for Rayleigh collapse (not to scale).

Numerical Method

Bubble collapse in soft viscoelastic biomaterial is simulated using the commercial solver *Fluent*. The *Multiphase, Volume of Fluid (VOF)* model is used along with an in-house subroutine developed to simulate viscoelastic material. The procedure described

here is general and can be utilized for any application involved with multiphase, compressible, viscoelastic simulation. We need three conservation equations (mass, momentum, and energy), two constitutive relations (viscous stress and elastic stress), and two equations of state (viscoelastic phase and VAM phase) to close the system of equations. The detail of the conservation equations solved by *Fluent,* when multiphase VOF method is turned on, can be found in *ANSYS Documentation* [158] and, therefore, only the method involved in viscoelastic modeling is discussed in this manuscript.

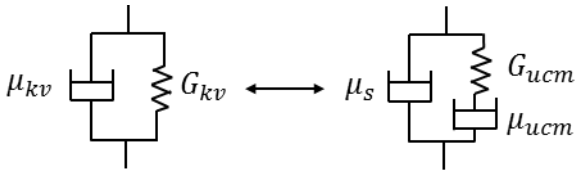

Figure 3-4 Kelvin-Voigt model and 3-parameter fluid model with Maxwell element.

The Kelvin-Voigt (KV) constitutive model for soft viscoelastic material has been considered here since many had previously used this model for soft material, and some experimental data for this model are present as well [17], [58], [159]–[163]. The stress tensor can be defined as, $\boldsymbol{\sigma} = -P\boldsymbol{I} + \boldsymbol{T}$, where P is pressure, $\boldsymbol{I}$ is the identity tensor and $\boldsymbol{T}$ is the deviatoric stress tensor, which is given for KV model as, $\boldsymbol{T} = \boldsymbol{T_V} + \boldsymbol{T_E}$ (all bold face and hat symbols are tensor and vector, respectively; unless otherwise mentioned). Both the hydrostatic $(-P\boldsymbol{I})$ and viscous stress $(\boldsymbol{T_V})$ are taken care by *Fluent* algorithm. Only the elastic contribution $(\boldsymbol{T_E})$ is needed to be incorporated into the momentum equation as source term, $\vec{F}_{source} = \vec{\nabla}.\boldsymbol{T_E}$, using the customization capability of *Fluent* through the user-defined functions (UDFs) [153]. The elastic strain, however, is not defined for fluid since, in the Eulerian formulation, the deformation gradient is not defined. Instead, the elastic strain is computed by integrating the strain rate [164]. Due to the large deformation in fluid, a non-linear Maxwell element (viscous damper (μ_{ucm}) and elastic

spring (G_{ucm}) in series) is added with the solvent viscous damper (μ_s) (figure 3-4). The zero-shear viscosity of the Kelvin-Voigt model is related to the 3-parameter Maxwell fluid as, $\mu_{kv} = \mu_s + \mu_{ucm}$. However, Maxwell element is viscoelastic in nature, having purely Newtonian (fluid like) behavior in low frequency limit and Hookean elastic (solid like) in the high frequency limit [165]. Therefore, the relaxation time of the Maxwell element ($\tau_{ucm} = \mu_{ucm}/G_{ucm}$) is crucial for the responses of the 3-parameter Maxwell to behave as Kelvin-Voigt. Given that our characteristic observation time is the bubble collapse time, then $\tau_{ucm} \gg t_c$, would model the 3-parameter Maxwell fluid as the Kelvin-Voigt model. The Deborah number is defined as the ratio of the characteristic time of the material to relax and the characteristic time of the observation. We have defined the Deborah number as, $De = \tau_{ucm}/t_c$, and $De \to \infty$ is required for the Kelvin-Voigt model. However, there is a limit on how big τ_{ucm} can be, since there are difficulties with the numerical instability for high Weissenberg number, and will be discussed in detail in the model validation part. The constitutive equation for the Maxwell element is given as

$$\tau_{ucm} \overset{\nabla}{\boldsymbol{T}_{\boldsymbol{E}}} + \boldsymbol{T}_{\boldsymbol{E}} = \mu_{ucm}(\boldsymbol{\nabla u} + \boldsymbol{\nabla u}^T) \tag{3.5}$$

Where $\boldsymbol{\nabla u}$ is the velocity gradient. The elastic stress is needed to be advected with the fluid element, and the constraint of objectivity is fulfilled by the objective derivative. The upper convective derivative is used for the purpose,

$$\overset{\nabla}{\boldsymbol{T}_{\boldsymbol{E}}} \equiv \frac{\partial \boldsymbol{T}_{\boldsymbol{E}}}{\partial t} + (\vec{u}.\vec{\nabla})\boldsymbol{T}_{\boldsymbol{E}} - \boldsymbol{\nabla u}.\boldsymbol{T}_{\boldsymbol{E}} - \boldsymbol{T}_{\boldsymbol{E}}.\boldsymbol{\nabla u}^T \tag{3.6}$$

The objectivity of the equation 3.6 is applicable to the compressible fluid as well [155]. Therefore, from equation 3.6, we get the scalar transport equation for each stress term (i.e., T_{Eij}). In equation 3.6 the first term in the left-hand side is the unsteady/transient part followed by a convective term. The last two terms in the right-hand side are the

source terms for the transport equation (S_{source}). *Fluent* has the capability of solving the general user-defined scalar (UDS) transport equation of the form given below,

$$\frac{\partial(\rho_L \varphi)}{\partial t} + \frac{\partial}{\partial x_i}(\rho_L u_i \varphi - \Gamma \frac{\partial \varphi}{\partial x_i}) = S_{source} \tag{3.7}$$

We can evaluate each term of the elastic stress tensor (T_{Eij}) comparing equations 3.6 and 3.7. We can simply put $\Gamma = 0$ into equation 3.7 since there is no diffusion term in equation 3.6. However, for high Weissenberg number flow, many have suggested that keeping diffusion term $(\Gamma \neq 0)$ significantly improve the convergence [154], and we used $\Gamma = 1$, for high τ_{ucm} without any convergence issue. It should be noted that *Fluent* by default includes density term while solving unsteady and convective terms in equation 3.7 and hence subroutine must exclude them while solving UDS for equation 3.7. Therefore, the source term for the momentum equation simply become,

$$\vec{F}_{source} = \vec{\nabla}.\boldsymbol{T_E} \tag{3.8}$$

Simulation Setup

For a bubble of radius R_{max}, we take the domain radius to be $20R_{max}$ with increasing mesh density at the center and final mesh is taken with cell size 2.5 μm when convergence criteria are met as described in [67] (figure 3-5). Quadrilateral grids are created using *ANSYS Meshing*. In *Fluent*, *Multiphase VOF* with 2 Euler phases is turned on, and *Species Transport Model* is used without reaction (this specific model is only needed for bubble content as it is defined as the mixture of vapor and air). To incorporate the compressibility, we activate the energy equation and select viscous heating from the viscous model for numerical stability. The viscoelastic phase is modeled as compressible water with added elasticity (explained in the previous section) and patched as the primary phase. The initial density of the viscoelastic phase is set to 1000kg/m^{3,} and without the

loss of generality, the compressibility was modeled using the *Tait equation of state*. The bulk modulus and sound speed of the biomaterials, of relative importance to our study, is typically in the range of 2GPa and 1500m/s, respectively [9], [11], [34]. These values are close to pure water. Besides, the near incompressibility of the biomaterials (typical Poisson's ratio 0.49) justify using the Tait equation of state for soft materials, and many have used similar equation of state to model the compressible viscoelastic materials [154], [155], [165]. The bubble content (VAM) is patched as the secondary phase, and the ideal gas law of mixture is used for the VAM density. Viscosity and surface tension are varied for representative soft materials and given in table 3-3. Operating pressure is set to 101325 Pa, and user-defined functions (UDFs) are *interpreted* before the boundary condition (BC) is set up. For the sake of convergence of compressible simulations, both pressure inlet and pressure outlet are used as BC, and both static and total pressure is set to P_∞ so that there is no pressure reflection from the boundary when the simulation starts. The boundary conditions for UDS-variables are defined as zero flux at the boundary. At this point, the source for momentum equations and UDS are added from the Cell Zone Condition. Total 31 user-defined memory (UDMI) locations and 8 UDS are required for solving the extra elastic stress tensor and saving the value of deviatoric (shear) and isotropic energy at each time step. Simulation is initiated with pressure to P_∞ value and $T_0 = 300\ K$ while all other values are kept as 0. After initialization, VAM is patched at the center with vapor volume fraction given as input to define the mixture species concentration followed by patching the bubble pressure (P_B) at the same region (figure 3-5). Pressure based couple solver is used for velocity-pressure coupling and the *QUICK* scheme is used for all discretization except the *Compressive Scheme* is used for volume fraction. Convergence criteria are set to 10^{-6} for all equations with

underrelaxation factors were set 1. All simulations are run up to $100\mu s$ with $5\ ns$ time step.

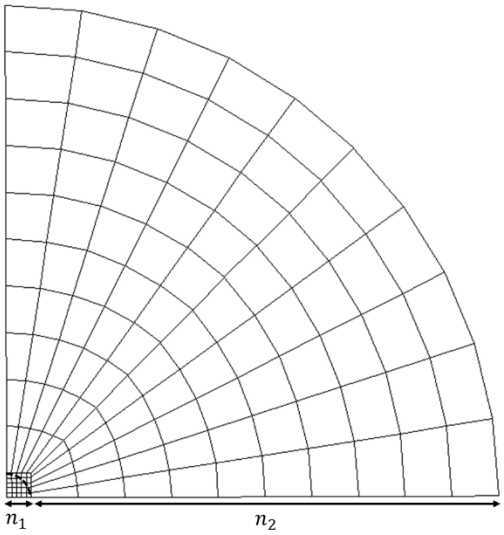

Figure 3-5 Simulation setup. A representative 2D axisymmetric mesh (not actual scale). The simulation box is made big enough so that the reflected pressure wave from the boundary does not interact with the collapsing bubble. The gradient of quadrilateral grids is meshed using *ANSYS Meshing* to have a high resolution at the center yet have a manageable number of elements to have less computational time.

Results and Discussions

Mesh Independence Study and Model Validation

We have prepared 4 meshes with increasing elements. Table 3-1 summarizes the mesh details.

Table 3-1 Mesh Independence Study

	Symmetric		
	n_1	n_2	Element
Mesh1	50	250	27500
Mesh2	100	400	90000
Mesh3	**200**	**600**	**280000**
Mesh4	250	700	412500

Bubble collapsing pressure at $\rho/R_{max} = 1$ is considered for the convergence, and relative error (%) is calculated as, $e = \left(\left|P_{peak}^{i} - P_{peak}^{i-1}\right|/P_{peak}^{i-1}\right) \times 100$, where i is the mesh number. Mesh3 is used for final simulations since the mesh independence criterion is set to $e < 1\%$.

Table 3-2 Maximum collapsing pressure at $\rho/R_{max} = 1$ for mesh independent analysis

i	Mesh1	Mesh2	Mesh3	Mesh4
$P_{peak}\ [MPa]$	2.891	1.594	1.338	1.332
Relative error (%), e		41.96	16.05	0.49

Model validation is done for water and Kelvin-Voigt with experimental data. For water, we have used the experimental observation from the work of Lauterborn et al. [166], and the Kelvin-Voigt model is validated from the work of Estrada et al. (2018).

Both Mesh2 and Mesh3 have been used, and a better fit is observed for Mesh3. In the experiment, Lauretborn observed that the bubble collapsed from the maximum radius of 2 mm, and the collapse time was roughly 0.2 ms. Figure 3-6 shows the bubble wall motion and comparison between the experimental observation and simulation. Mesh2 shows a smaller collapsing bubble radius with higher collapsing pressure. Mesh3 reasonably predicts the collapse radius and pressure. The experimental observation did not include the stress-free equilibrium bubble radius. Therefore, initial bubble pressure was not known and needed to be fitted for the collapse time.

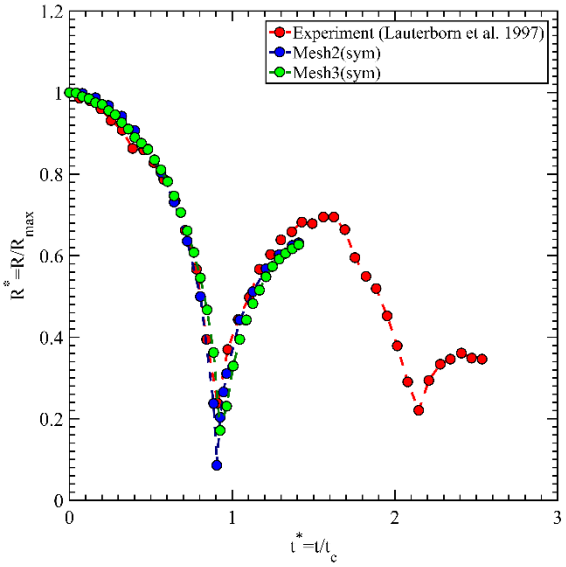

Figure 3-6 Cavitation bubble dynamics in water.

In figure 3-7, we have shown the model validation of the Kelvin-Voigt model. Experimental observation of Estrada et al. (2018) is recreated using our viscoelastic CFD model and are compared with the simulated results. They used a high energetic localized laser pulse to cavitate a bubble in soft material, and a high-speed camera is used to capture the wall motion. The wall motion is then fitted to the viscoelastic Rayleigh-Plesset equation to find the material property. They have fitted the data with the Kelvin-Voigt model with $\mu_{kv} = 0.089\ Pa.s$ and $G_{kv} = 10\ kPa$. In our 3-parameter Maxwell fluid, we needed to fit the values as, $\mu_s + \mu_{ucm} = 0.089\ Pa.s$ and $G_{ucm} = 10\ kPa$. Due to the numerical limit on the τ_{ucm}we kept the Deborah number to 1 and 2. From the experimental data $R_{max} = 344.1\mu m$ and R_{eq}~$50\mu m$. We used this ratio to find the initial bubble pressure, as discussed earlier. The collapsing time is calculated to be, $t_c = 34\mu s$ and rest of the parameters were $(\tau_{ucm}, \mu_{ucm}, \mu_s)$ set accordingly. For De=1, the 3-parameter Maxwell model relaxes within the time of the collapse, and the bubble wall

initially delays in response. However, during the first collapse, elasticity plays a significant role, and subsequent dynamics are more viscosity dominant. Therefore, viscous dissipation is less prominent. Increasing De to 2 shows a better fit and is used for all the simulations.

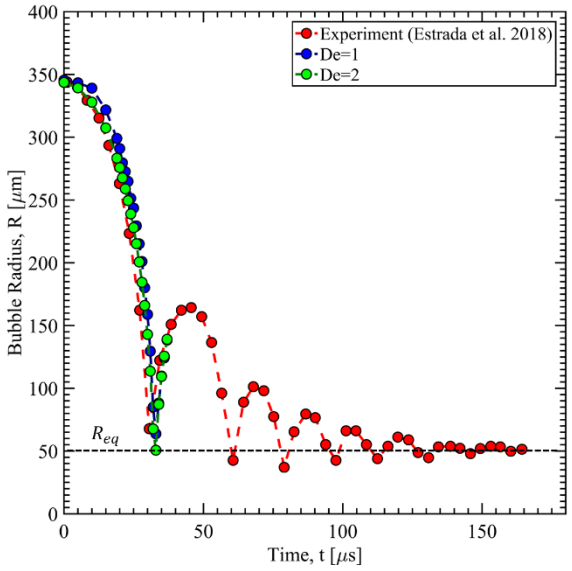

Figure 3-7 Cavitation bubble dynamics in Kelvin-Voigt material.

Bubble Dynamics in Soft Materials

Rayleigh collapse in cavitation condition has been studied. Material elasticity (shear modulus) is varied from 2.6 to 20 kPa since biomaterials fall into this category [9], [17]. Table 3-3 summarizes the material properties used in our study. A total of 17 numerical simulations are performed to characterize the cavitation collapse efficiency defined in equation 3.4.

Material 2 is taken to be the base material while 100 kPa (gauge) far-field pressure and -73 kPa (gauge) bubble pressure (for $R_{eq}/R_{max} = 0.5$) are also kept as the base parameter when other parameters are varied.

Table 3-3 Material properties

Material	Density, $\rho_L\ [kg/m^3]$	Viscosity, $\mu_{kv}\ x10^{-3}\ [Pa.s]$	Shear Modulus, $G_{kv}\ [kPa]$	Surface Tension, $S\ [mN/m]$
1	**1010**	**1.22**	**2.66**	**86**
2	**1030**	**2.59**	**6.66**	**83**
3	**1050**	**8.21**	**13.33**	**82**
4	**1080**	**17.99**	**20.00**	**81**

Figure 3-8 shows single bubble dynamics in the viscoelastic phase and capture the first collapse due to the far-field pressure of 100 kPa (gauge). Time is nondimensionalized by the collapse time as,

$$t^* = \frac{t}{t_c} \tag{3.9}$$

Figure 3.9 shows the pressure distribution from the bubble wall. At the beginning of the collapse, bubble wall pressure reduces, and as the bubble wall accelerates inward, the pressure increases. Just after the collapse, a high-pressure pulse propagates and attenuates over the radial distance. We have nondimensionalized pressure ($P^* = P/P_{atm}$) with the atmospheric value, $P_{atm} = 101\ kPa$. A critical injury threshold is considered to be, $P^*_{cric} = 3.5$ and shown in figure 3-9. $P^*_{cric} = 3.5$ coincide with the severe brain injury criteria proposed by Ward et al. (1980). At the collapse, P^* reaches 150 at the bubble wall and then shock pressure peak attenuates over time and distance. At $\rho/R_{max} = 13$ the pressure reach P^*_{cric} and we can conclude that a region of radius 13 times higher than the bubble radius will experience enough strong pressure to be damaged.

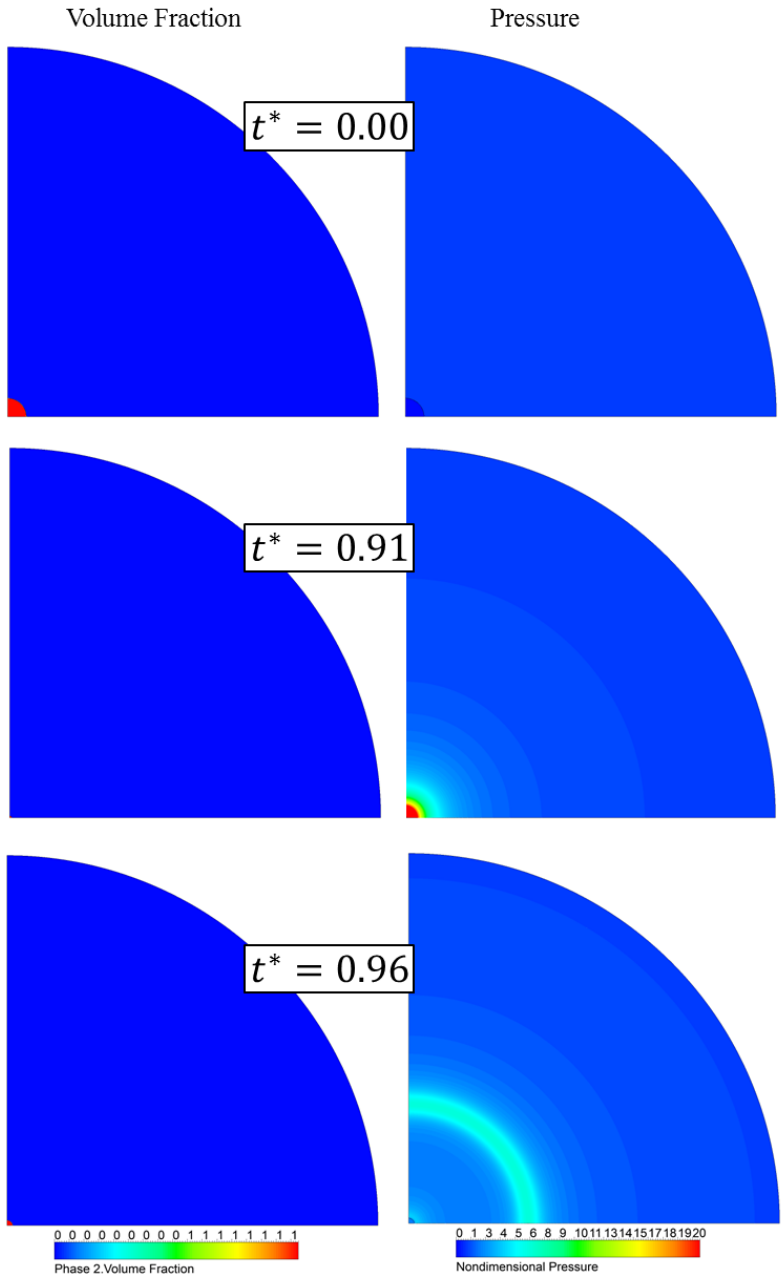

Figure 3-8 Collapsing bubble under far-field pressure of 100 kPa. Left column showing the volume fraction and the right column showing the pressure propagation after the collapse. Collapse (minimum bubble radius) was observed at $t^* = 0.91$.

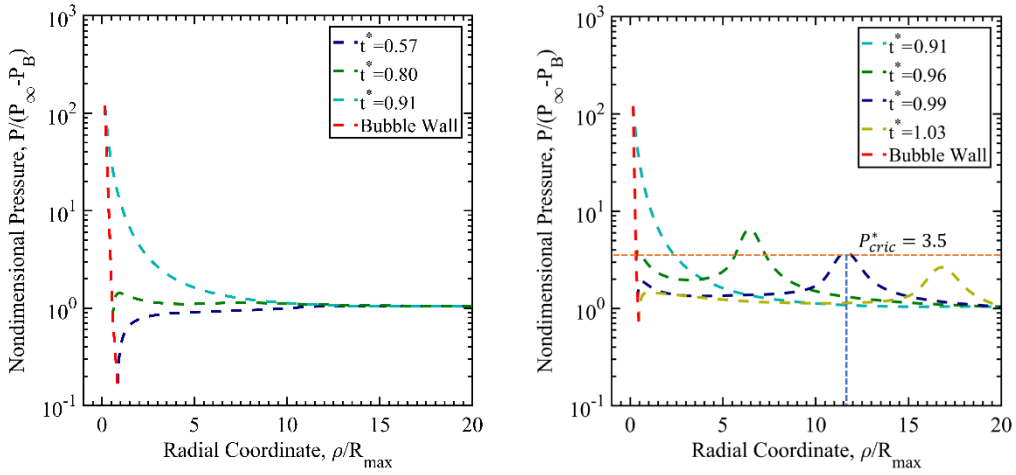

Figure 3-9 Pressure distribution from the bubble wall at different time. Collapse (left) and growth (right).

We have studied the strain and stress as well for the possible damage mechanism. However, the strain is not readily available for the Eulerian formulation in the CFD setup. The strain is estimated by integrating the strain rate tensor. Like any other fluid property, the elastic strain is needed to be advected with the fluid element, and the objective derivative fulfills the constraint of objectivity. The *Jauman* or *co-rotational* objective derivative for a tensor that incorporates translation and rotation along a path can be utilized here, and the elastic strain is given by [164],

$$\frac{\partial \boldsymbol{\epsilon}}{\partial t} + (\vec{u}.\vec{\nabla})\boldsymbol{\epsilon} = \boldsymbol{W\epsilon} - \boldsymbol{\epsilon W} + \frac{\boldsymbol{\nabla u} + \boldsymbol{\nabla u}^{\boldsymbol{T}}}{2} \tag{3.10}$$

Where $\boldsymbol{W} = (\boldsymbol{\nabla u} - \boldsymbol{\nabla u}^{\boldsymbol{T}})/2$, the asymmetric part of the velocity gradient ($\boldsymbol{\nabla u}$) that implies the solid-body rotation**.** The left-hand side of equation 3.10 is the material derivative that allows the strain to be convected along with the fluid particle, while the first two terms of the right-hand side rotate the strain as fluid itself rotates. We have used the

user-defined scaler transport equation to integrate equation 3.10, as discussed earlier. The deviatoric stress and strain is defined as,

$$\boldsymbol{\sigma^D} = \boldsymbol{\sigma} - \frac{1}{3} tr(\boldsymbol{\sigma}) \boldsymbol{I} \tag{3.11}$$

$$\boldsymbol{\epsilon^D} = \boldsymbol{\epsilon} - \frac{1}{3} tr(\boldsymbol{\epsilon}) \boldsymbol{I} \tag{3.12}$$

The von Mises stress and strain is then defined by the deviatoric tensors as,

$$\sigma_{vm} = \sqrt{\frac{3}{2} \boldsymbol{\sigma^D} : \boldsymbol{\sigma^D}} \tag{3.13}$$

$$\epsilon_{vm} = \sqrt{\frac{3}{2} \boldsymbol{\epsilon^D} : \boldsymbol{\epsilon^D}} \tag{3.14}$$

Stress is normalized by the P_{atm} as well, and figure 3-10 shows the spatial distribution of the normalized von Mises stress from the bubble wall. Two time-steps have been plotted, when the bubble collapses from its maximum size and then when it attains its minimum size at the collapse. We can see that the surrounding stress does not cross the threshold limit of damage. In figure 3-10, $\sigma_{vm}^{*} = 0.1$ corresponds to severe brain injury and a 50% probability of concussion proposed by Kang et al. (1997) and Kleiven (2007), respectively.

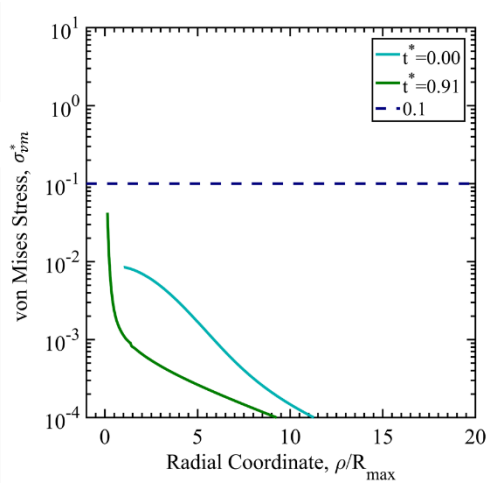

Figure 3-10 von Mises stress (nondimensionalized) distribution and injury threshold.

Deek and Willinger (2008) proposed a 50% probability of mild DAI if the von Mises strain reaches a threshold value of 0.25. What we have seen from figure 3-11(a) is that strain does not reach that high. However, another injury parameter is how much strain is experienced and at what loading rate. Strain times the strain rate estimate that quantity and shown in figure 3-11(b). We can see, at the time of the collapse, very close vicinity of the collapsing bubble experience way more strain rate dependent damage. 14/s, 19/s and 24/s indicate 25%, 50% and 75% mild TBI, respectively [56].

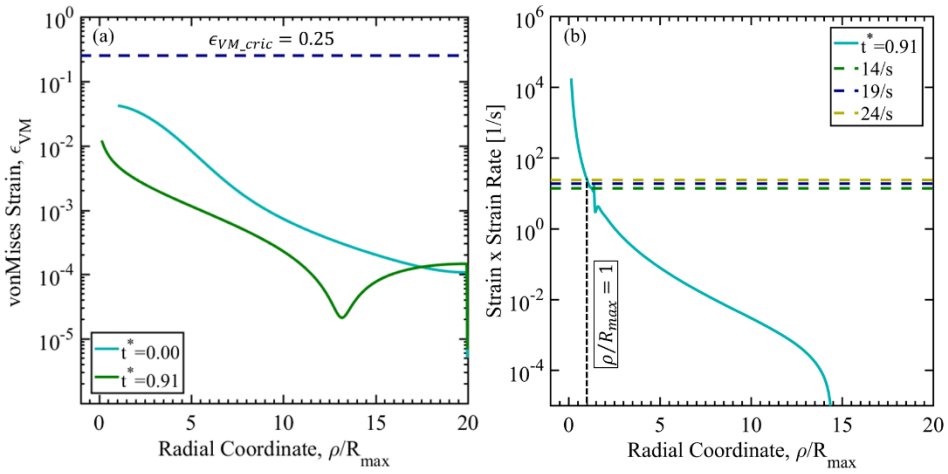

Figure 3-11 von Mises strain (a) and strain x strain rate (b) distribution compared with the injury threshold.

For the visualization purpose, we have shown a schematic of the state of deformation in figure 3-12. When the bubble grows to its maximum size, it compresses the surrounding medium. Any material points at ρ_o is in the compression at that moment. The growth is then followed by collapse, and the surrounding medium relaxes and then experiences a state of tension until the bubble attains its minimum size. The material point designated by the ρ_o at the reference configuration is now occupy the point ρ at the current configuration and experiences tension. Figure 3-11 confirms that at the time of the collapse, the material point that is dragged into the region defined by the maximum bubble volume $(4/3\,\pi R_{max}^3)$ experience enough high loading rate that may lead to a 75% probability of mild TBI. Therefore, in the subsequent analysis, we estimated the damage efficiency at $\rho/R_{max} = 1$.

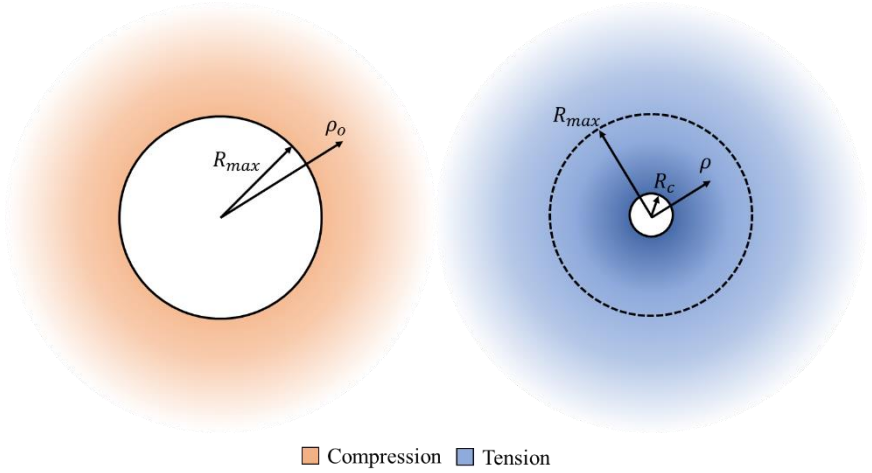

Figure 3-12 A material point in the reference configuration and the current configuration.

Effects of Far-Field Pressure

First 3 simulations are done with varied far-field pressure at 50, 100 and 200 kPa (gauge) while bubble pressure and material properties are kept fixed at -73 kPa (gauge) and material-3, respectively. Fig. 3-13 shows the secondary pressure wave (collapsing pressure), deviatoric (shear) energy and isotropic energy at $\rho/R_{max} = 1$. In all cases, local effects of cavitation collapse exceed the damage threshold value of 200 Jm^{-3}. It is evident that collapse time depends on far-field pressure and decreases with increasing pressure (Fig. 3-13(a)). The overall trend of shear energy is similar although initial differences remain to carry on. The effects of far-field pressure strongly dominate the isotropic energy. While increasing far-field pressure from 50 to 200 kPa, isotropic energy increases to 1729% while shear energy increase to 298% only.

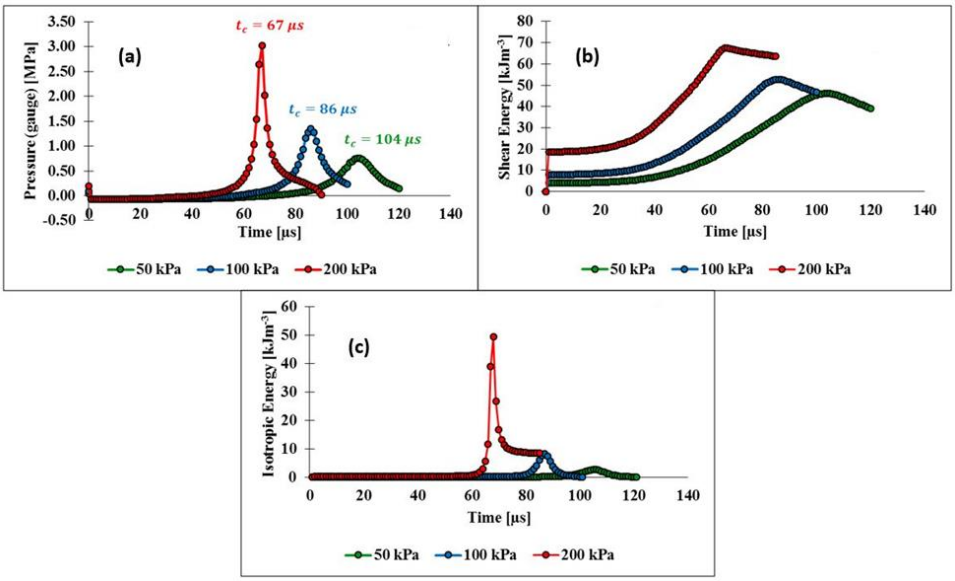

Figure 3-13 Far-field pressure effect on bubble collapse, (a) pressure profile (b) deviatoric (shear) energy (c) isotropic energy at $\rho/R_{max} = 1$

Fig. 3-14 shows the effect of far-field pressure on the collapse and damage intensity as well as on the efficiency of cavitation damage at $\rho/R_{max} = 1$. As by definition, collapse intensity increases as a quadratic function of the collapsing pressure. A similar trend is observed for the isotropic energy density and isotropic damage intensity for increasing far-field pressure fraction, P_∞/P_{atm}. Although shear energy density and shear damage intensity increase linearly with the far-field pressure, the damage efficiency caused by shear reduces for higher pressure. On the other hand, damage efficiency caused by volumetric response increases with far-field pressure. Therefore, it is obvious that for higher far-field pressure, the damage will be dictated by the isotropic (tensile or compressive) energy deposition rather than due to shear.

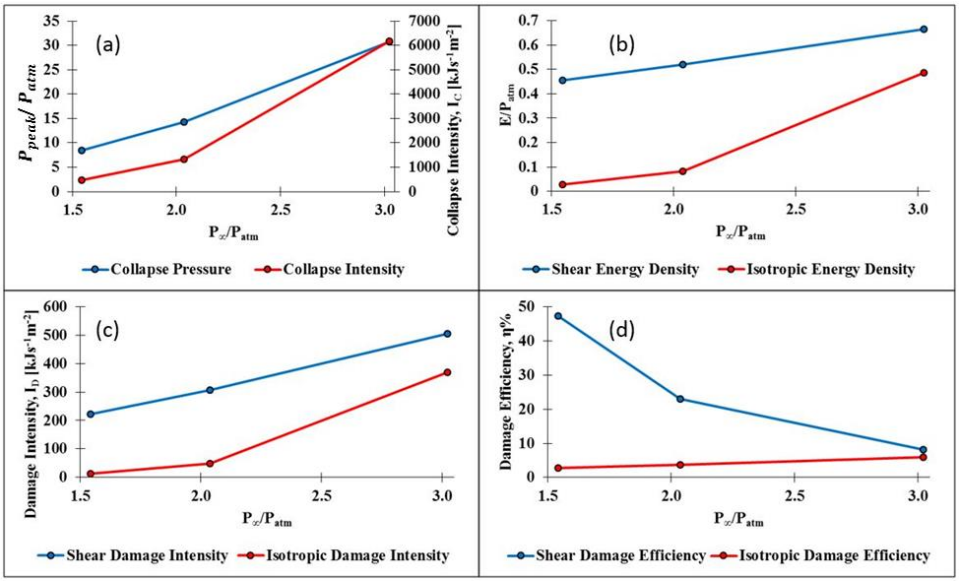

Figure 3-14 Far-field pressure effect on bubble collapse efficiency, (a) collapse pressure (abs) and collapse intensity (b) energy density (c) damage intensity, and (d) efficiency of cavitation damage.

Effects of Non-condensable Gas Content

Next, to observe the effect of gas content on the efficiency of the cavitation damage, we choose three different values of the partial pressure of the gas content. As discussed earlier, the initial contribution of gas content to bubble pressure can be approximated if R_{eq}/R_{max} is known from the experimental observation. However, in this manuscript, we consider three values of R_{eq}/R_{max} and they are varied to be 0.4, 05, and 0.6, which correspond to initial bubble pressure of -85, -73, and -55 kPa (gauge), respectively. Fig. 3-15 summarizes the effect of partial bubble pressure on the damage efficiency for 100 kPa (gauge) far-field pressure and material-3 at $\rho/R_{max} = 1$. As it is expected, collapse pressure and intensity decrease with the increasing partial pressure fraction since bubble gas content tends to dampen the violent nature of the collapse. For higher gas content, the collapse intensity, as well as isotropic damage intensity, reduce in

the same proportion, and it reflects on the damage efficiency due to isotropic energy deposition. On the other hand, although shear damage intensity decreases with the increasing gas content, the damage efficiency tends to increase. Evidently, for higher gas content, the damage will be dominated by the shear stress and shear deformation.

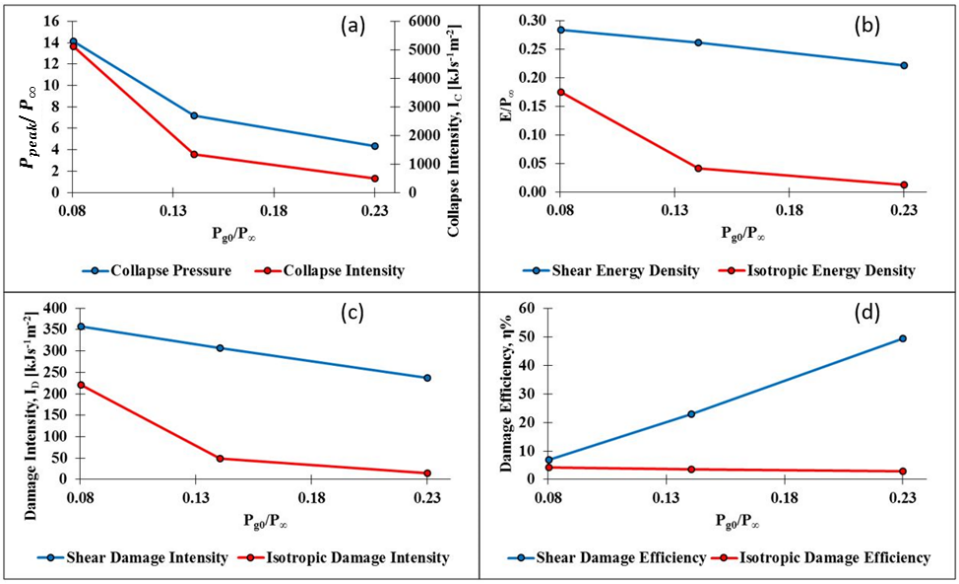

Figure 3-15 Effects of partial bubble pressure on the cavitation damage efficiency, (a) collapse pressure (abs) and collapse intensity (b) energy density (c) damage intensity, and (d) efficiency of cavitation damage.

Effects of Elasticity

We vary the shear modulus that is given in Table 3-3 and kept all other properties fixed to that of material-3. Not to mention that far-field pressure and initial bubble pressure is kept to the base values. For fixed viscosity ($8.21\ mPa.s$ for material-3), the retardation time (τ_{kv}) of the Kelvin-Voigt material reduces as shear modulus increases. The physical significance of retardation time for a material is the measure of how fast the transient response in a creep type loading and for a time considerably longer

than the τ_{kv}, the KV material behaves as pure solid [167]. For the shear modulus given in Table 3-3, the retardation time varies from $0.4 - 3\ \mu s$, which implies that in the duration of our simulation the transient response accumulates and Fig. 3-16 shows that elasticity works as the restraining force and tends to reduce the collapsing velocity. Eventually, this leads to reduced collapsing pressure as expected.

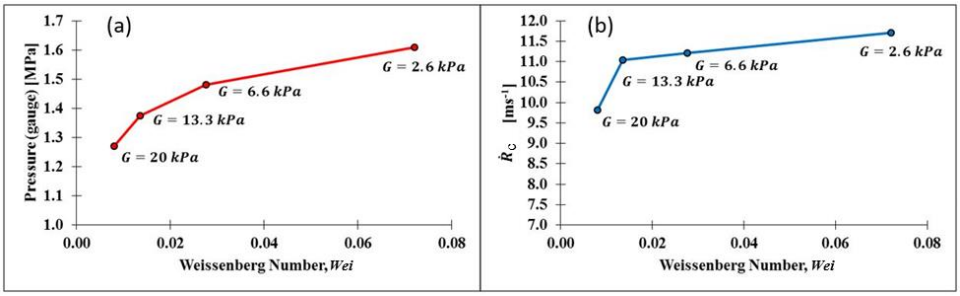

Figure 3-16 Effects of elasticity on the collapsing pressure and bubble wall velocity at $\rho/R_{max} = 1$

From Fig. 3-17, it is important to mention that collapse intensity, as well as isotropic damage intensity, reduce with increasing shear modulus. Therefore, damage efficiency due to isotropic energy recuses as well. Nevertheless, the cavitation damage efficiency for shearing increases with higher shear modulus, since added shear modulus directly contributes to the deviatoric stress.

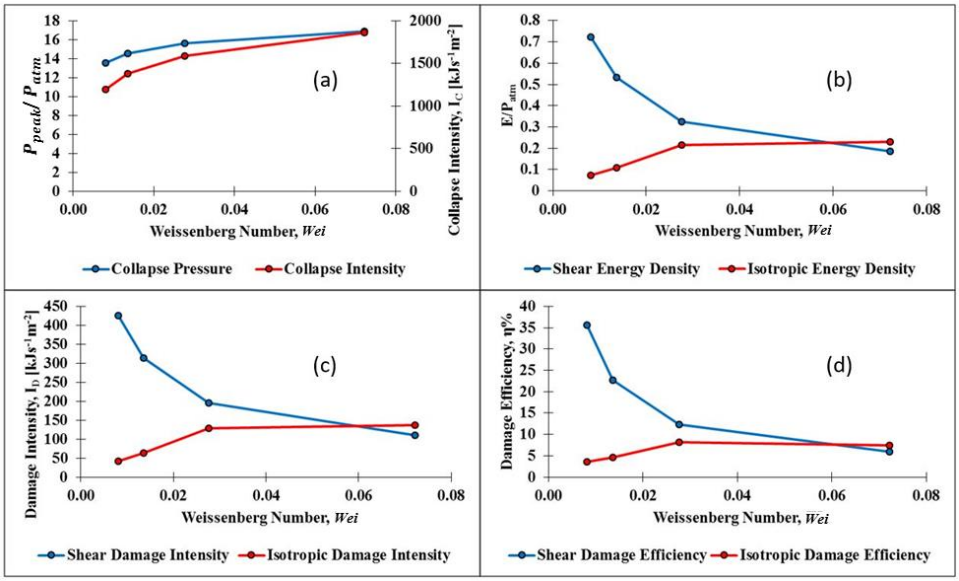

Figure 3-17 Effects of elasticity on the cavitation damage efficiency, (a) collapse pressure (abs) and collapse intensity (b) energy density (c) damage intensity, and (d) efficiency of cavitation damage.

Effects of Viscosity

Keeping all the properties fixed to material-3, only viscosity is varied, and the results are summarized in the following for 100 kPa (gauge) far-field pressure and -73 kPa (gauge) bubble pressure. We can see from Fig.3-18 that the effect of viscosity is insignificant to the collapsing bubble wall velocity. This explains why the collapsing pressure does not vary much with the Reynolds number, as Fig. 3-19(a) shows. Although viscosity is increased to 1374% for material-1 to material-4, the energy density, damage intensity, and the damage efficiency (for both shear and isotropic) vary too little to the increase in viscosity. At the time of the collapse, the Reynolds number is calculated to be in the range $10^{3,}$ and inertia plays a significant role than the viscosity. This coincides with the findings of Estrada et al. (2018) that while elasticity dominates the first collapse (discussed in the previous section), the viscosity becomes more prominent for

subsequent collapses and rebounds. Since, in our simulations, we have given much emphasis on the first collapse, which is considered to be the most damaging in nature, the subsequent collapses are not simulated, and the damping effect of viscosity is not observed.

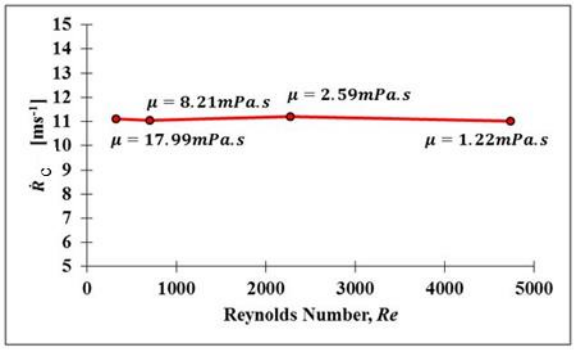

Figure 3-18 Increasing viscosity shows no effect on the collapse velocity.

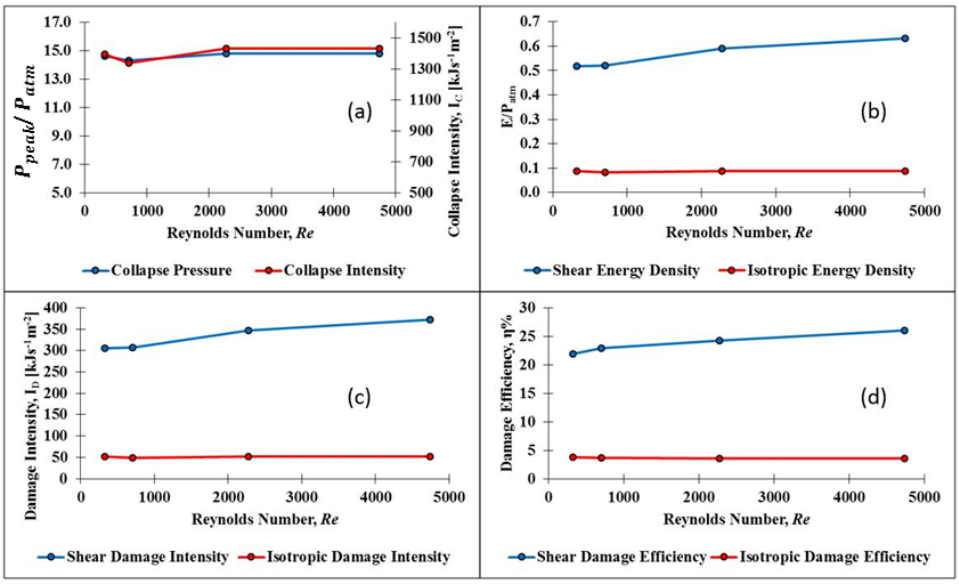

Figure 3-19 Effects of viscosity on the cavitation damage efficiency, (a) collapse pressure (abs) and collapse intensity (b) energy density (c) damage intensity, and (d) efficiency of cavitation damage.

Effects of Surface Tension

Keeping all the properties of material-3 fixed, only surface tension is varied, and the results are summarized in the following for 100 kPa (gauge) far-field pressure and -73 kPa (gauge) bubble pressure. From the Laplace equation of pressure balance ($P_B = P_\infty + 2S/R$) it is obvious that the surface tension acts in favor of collapse, although Fig. 3-20(a) shows the collapse pressure does not respond to the variation of surface tension. This is probably because of the existence of elasticity, which acts against the collapse, and both effects are canceling each other. The effects of surface tension could be more evident at the nano to microscale. Similar to viscosity (Fig.3-19(d)), shear dominated damage is more prominent in this case as well.

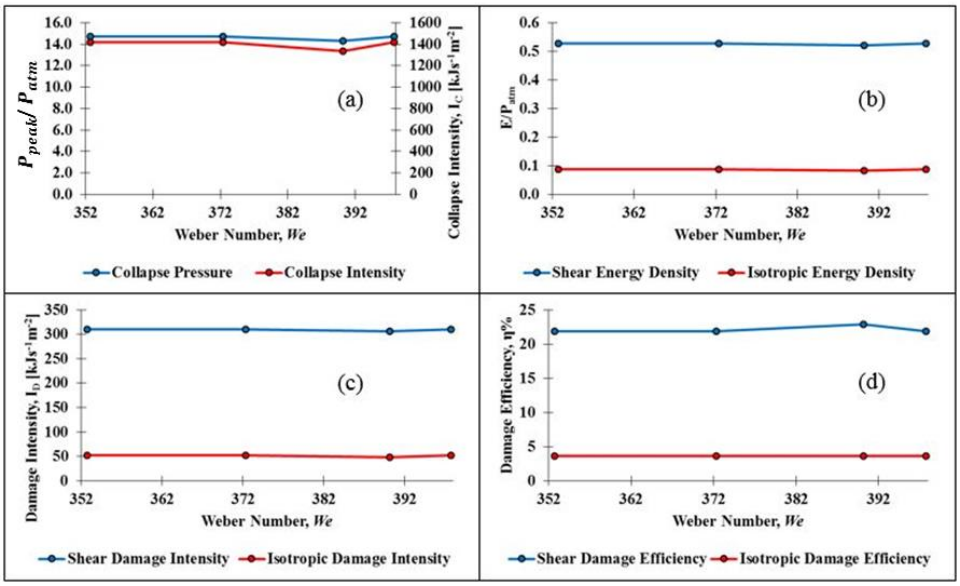

Figure 3-20 Effects of surface tension on the cavitation damage efficiency, (a) collapse pressure (abs) and collapse intensity (b) energy density (c) damage intensity, and (d) efficiency of cavitation damage.

Conclusion

The emerging implication of cavitation mechanics in different sectors, including the prediction of mild TBI damage to soft biological materials, gained importance recently. However, experimental prediction remains challenging because the brain is the most delicate part of the body. Therefore, our goal is to predict damage criteria and mechanism induced by the cavitation, and a computational approach is taken to evaluate the factors affecting the damage intensity of the brain like soft materials.

In this chapter, we have investigated the damage mechanism due to the cavitation collapse, which is potentially the major cause of mild TBI. The effect of far-field pressure and elasticity of medium, amount of non-condensable gas content inside cavitation bubble, viscosity, and surface tension of the medium on the damage efficiency is evaluated. We have discussed and identified the damage mechanics of soft materials as the properties are varied.

Our study reveals that the increase of far-field pressure decreases the collapse time and increases the peak collapsing pressure. Moreover, the increase of far-field pressure increases the collapse intensity and damage intensity. The maximum far-field pressure was limited to 200 kPa (gauge) to be within the injury threshold proposed by Ward et al. (1980). This proved to be a critical point in our case. Up to 200 kPa (gauge), far-field pressure damage was dominated by the shear deformation. However, the efficiency of shear damage decreases and isotropic damage increases, which depicts that at higher far-field pressure ($P_\infty > 200\ kPa\ (gauge)$) damage will be dominated by tensile or compressive force. The effect of gas content gives the opposite effect of far-field pressure increment. At higher gas content, the damage is dominated by shear. The gas content act as a damper by reducing the collapse pressure. Due to the numerical

instabilities, we were forced to limit the gas content within the range, $0.4 < R_{eq}/R_{max} < 0.6$, although Estrada et al. (2018) observed less gas content ($R_{eq}/R_{max} \sim 0.1$). None the less, within the range of our simulations, a quadratic relation for isotropic damage intensity and a linear isotropic damage efficiency can be extrapolated (from Fig. 3-15), and a prediction can be made for the less gas content.

Other than the two pressure factors discussed above, the elasticity of soft materials is the most interesting one to play a key role in bubble dynamics. The presence of elasticity of soft materials is advantageous since it acts as a spring and acts against the bubble wall motion. Therefore, it reduces the bubble collapse intensity and growth as well. However, the elasticity term is added to the deviatoric part of the stress tensor, which causes to increase the shear dominated damage efficiency. On the other hand, viscosity and surface tension have got a very trivial impact on tuning the shear or isotropic damage efficiency. However, viscosity is more dominant in subsequent collapses and rebounds, which is not captured in our simulations. Viscous dissipation as the thermal energy may increase the temperature of the surrounding medium in the subsequent collapse and growth [168]. This could lead to a different mechanism of soft material damage and can be studied in the future project. Although we used a compressible model to capture the secondary pressure wave of the collapsing bubble, the effect of compressibility itself was not significant within the range of parameters we considered. This effect will be more prominent, depending on more adverse far-field pressure and less gas content scenarios. The most important outcome is having the elasticity of soft materials (or any biological tissue); the violent nature of the collapsing bubble is mitigated.

From this work, damage modes at different conditions are predicted, which gives valuable insight into the continuum scale. However, in molecular-scale damage can be affected by various other factors as well, such as inhomogeneity of biomolecules, presence of hydrophobic surface, and interfacial tension, etc. In future work, those factors can be included by doing multiscale modeling, and the observed loading conditions from this manuscript can be used as the boundary conditions to the fluid-structure interaction type model where the precise nature of microstructural damage can be identified.

Chapter 4

Micromechanical Viscoelastic Characterization of the Neuronal Cell

In previous chapters, we have discussed how cavitation can be initiated in the soft materials and the intensity of cavitation induced damage. The cavitation onset criteria are studied from the microstructural point of view of the gel system, and cavitation damage is evaluated in the macroscale, respectively. To understand how continuum scale damage is correlated to the soft material microstructure, we have studied and characterized the mechanical behavior of the neuronal cell. In the tissue level, the brain is largely classified into two regions, i) gray matter and ii) white matter. In gray matter, neuronal cells are randomly distributed and the mechanical behavior is isotropic. Neuronal cells are bundled together and form fiber tracts, which are distributed in a more organized manner in the white matter region. Therefore, the mechanical behavior is anisotropic for the white matter. Figure 4-1 shows the image of the neuronal tracts in the white matter using the diffuse tensor imaging (DTI) technique.

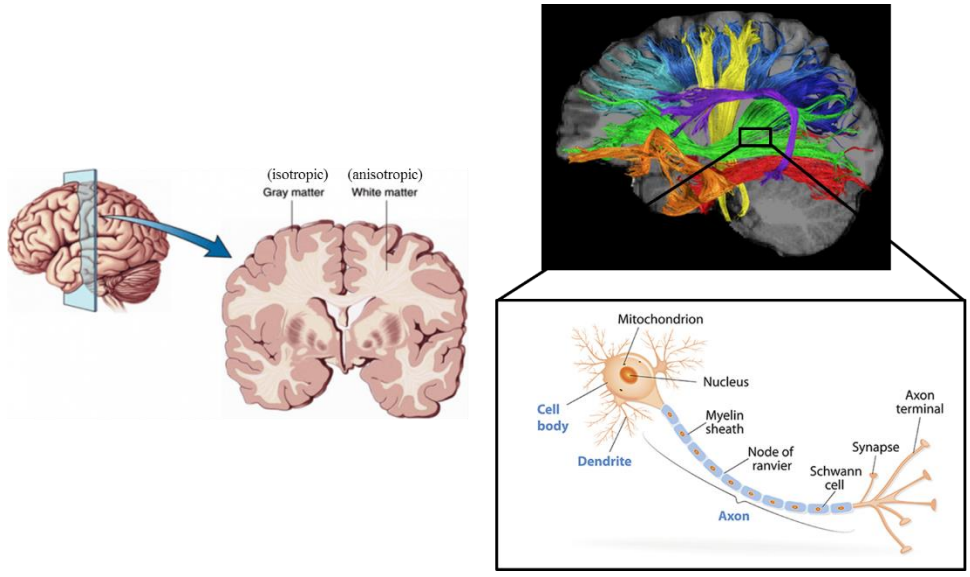

Figure 4-1 White matter and gray matter (left). Neuronal fiber tract in the white matter (right-top) and neuronal cell (right bottom).

When the head is impacted, the brain tissue undergoes shear deformation. The reason is two folds. The brain is enclosed within the skull and cannot deform volumetrically when subjected to the dynamic loading. Besides, the bulk modulus is a couple of order magnitude higher than the shear modulus, and the tissue mainly experiences deformation that is shear dominated [169]. Figure 4-2 shows how rotational acceleration and deceleration lead to axonal stretching. This type of loading condition may lead to mechanical failure of the axonal microstructure and cause the most common pathological feature of TBI called the diffuse axonal injury (DAI).

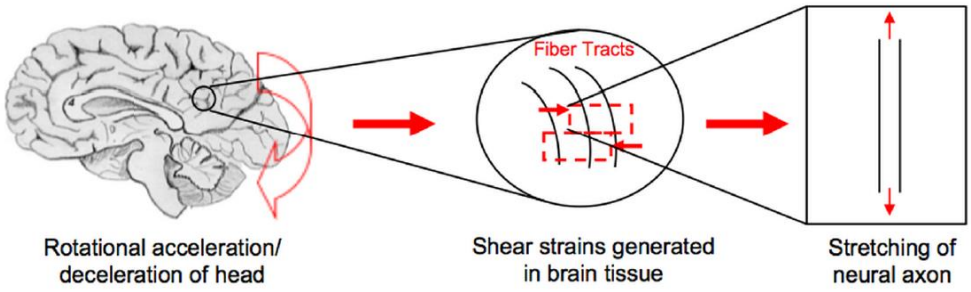

Figure 4-2 Brain subjected to rotational acceleration and deceleration, causing the axonal stretching (image adopted from [169]).

The long-term plan is to develop a brain tissue model with the microstructural detail and to study DAI. Figure 4-3 (left) shows the work of Kasthuri et al. (2015), who has reconstructed the neocortex [170]. We have imported the volume mesh of the individual axon and dendrites from their files, and figure 4-3 (right) shows an aggregate of neuronal cells randomly oriented in the space. However, the major issue is to have proper mechanical properties of the axon, and this is the main objective of this chapter.

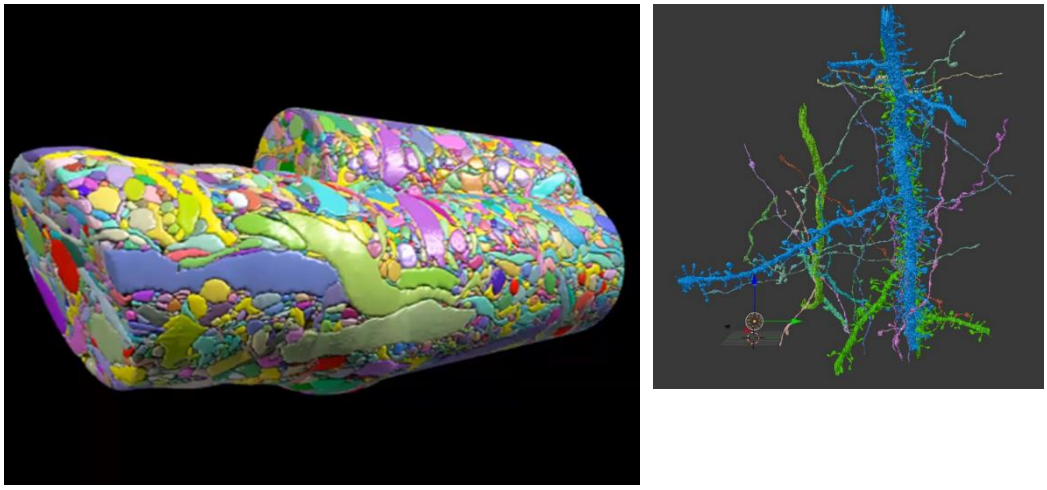

Figure 4-3 (left) reconstruction of neocortex [170]. (right) imported axon and dendrites volume mesh to model the neuronal cell aggregate.

We have taken a bottom-up approach from the multiscale point of view and developed the representative volume element (RVE) of the axon and characterize the mechanical properties. In doing so, we have modeled the detail cytoskeletal components that the axon is consists of. The long stem-like part of the neuronal cell is the axon, and the main mechanical property of the axon is due to its microstructural components. Microtubules (MT) are the primary cytoskeletal component from where the significant rigidity is contributed [171]. Axially oriented MTs are crosslinked by the Tau protein (tau) of viscoelastic nature. The time-dependent viscoelastic nature of the axon is generally coming from the tau. Figure 4-4 shows the detail of the microstructural components and their orientation.

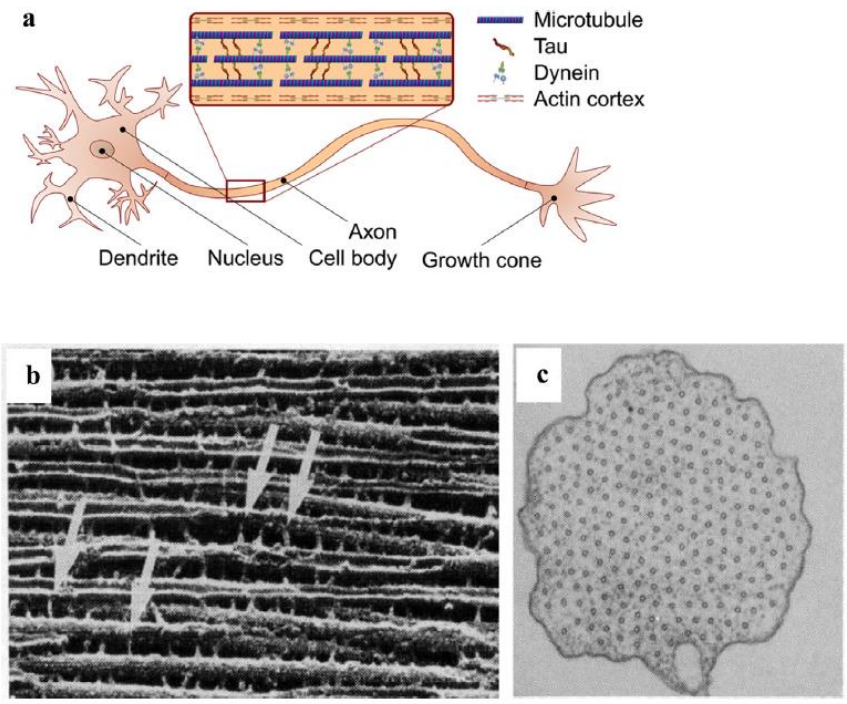

Figure 4-4 (a) anatomy of the neuronal cell. (b) SEM image of how axially oriented MTs are crosslinked with the tau. (c) A cross-sectional view of the transverse plane shows the hexagonal orientation of MTs. (adopted from [172])

The cross-sectional view of the axon indicates that the MTs are oriented in a hexagonal array, and most of the axonal microstructure studies model the MT bundle as such. Figure 4-5 shows how the MT bundles are crosslinked with tau.

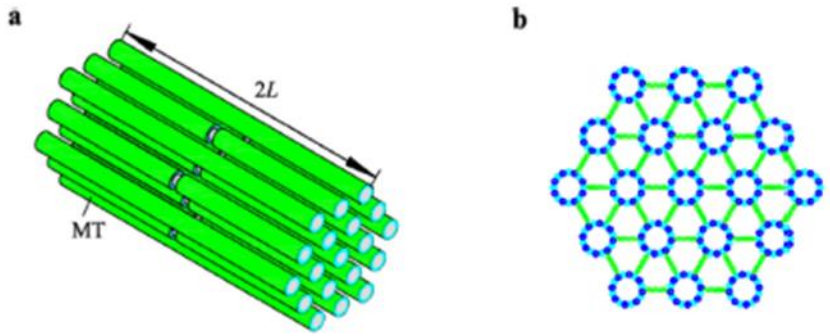

Figure 4-5 Axonal microstructural model for analysis (adopted from [172]).

Material and Geometric Properties of Axon

Just like any other microstructure of biomaterials, axonal microstructural parameters vary within a wide range. Figure 4-6 shows the geometric definition we have used as parameters. Table 4-1 summarizes those parameters and refers to the literature. The length of the MTs ($2L$) is between 1 to 10 μm with discontinuity within 80% of the center of the length. The inner (R_{IMT}) and the outer (R_{OMT}) radii of the MT are 7 nm and 12.5 nm, respectively. The Young's modulus of MT (E_{MT}) varies between 1.5 to 1.9 GPa. The spacing between two MTs (d_{MT}) are within 20-38 nm. MT fails at 50% strain (ϵ_{MT}).

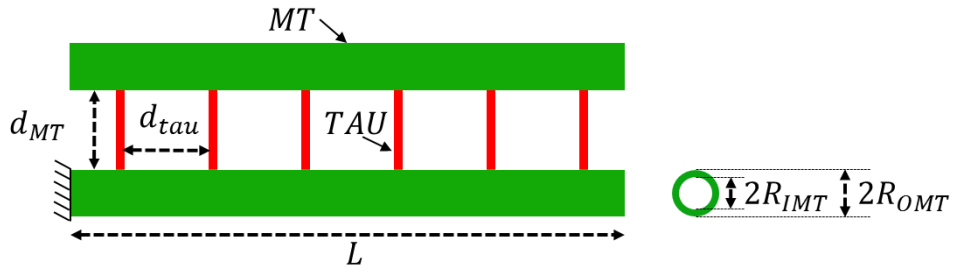

Figure 4-6 Geometric properties of the MT-Tau crosslinked network

The tau protein, on the other hand, shows viscoelastic mechanical behavior and is usually modeled as the Kelvin-Voigt model. The radius of tau (R_{tau}) varied between 4-10 nm. The Young's modulus of tau (E_{tau}) is 5 MPa and the retardation time ($\tau_{tau} =$

μ_{tau}/E_{tau}) is 0.35 s. Therefore, the tau viscosity is measured to be $\mu_{tau} = 1.75\ MPa.s$. The spacing of tau (d_{tau}) is within 20-40 nm. Tau failure strain (ϵ_{tau}) is 40%.

Table 4-1 Material and Geometric Properties of the Cytoskeletal Components

Variable	Value	References
R_{OMT}	12.5 nm	[173]
R_{IMT}	7 nm	[173]
E_{MT}	1.5-1.9 GPa	[174]
d_{MT}	20-38 nm	[175]
R_{tau}	4-10 nm	[176]
E_{tau}	5 MPa	[174], [177]
τ_{tau}	0.35 s	[178], [179]
d_{tau}	20-40 nm	[180]
$2L$	1-10 μm	[173]
ϵ_{MT}	50%	[181]–[183]
ϵ_{tau}	40%	[179]

The available material data for tau protein is for the Kelvin-Voigt (KV) model. However, we have used ANSYS Mechanical for the viscoelastic characterization, and ANSYS only accepts viscoelastic parameters for General Maxwell (GM) model. Another challenge is that the relaxation modulus must be input for shear and bulk modulus. Therefore, we have first estimated the GM parameters for Young's modulus by fitting creep responses of KV and GM. Then Alfrey's correspondence principle has been utilized to evaluate the shear relaxation parameters for tau. Figure 4-7 shows the two steps of finding the parameters.

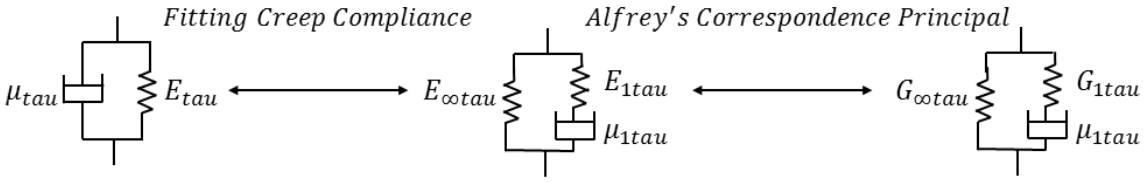

Figure 4-7 Procedure of defining the tau properties for ANSYS.

The constitutive relation between the stress (σ) and strain (ϵ) for KV and 3-parameter GM model is given below,

KV: $$\sigma = E_{tau}\epsilon + \mu_{tau}\dot{\epsilon} \tag{4.1}$$

GM: $$\sigma + \frac{\mu_{1tau}}{E_{1tau}}\dot{\sigma} = E_{\infty tau}\epsilon + \frac{\mu_{1tau}(E_{\infty tau} + E_{1tau})}{E_{1tau}}\dot{\epsilon} \tag{4.2}$$

Equation 4.1 and 4.2 are solved for creep loading ($\sigma \neq 0$ and $\dot{\sigma} = 0$) by setting $E_{tau} = E_{\infty tau}$ and $\mu_{tau} = \mu_{1tau}$. Figure 4-8 shows the fit by increasing E_{1tau}. From the analysis, the best fit is considered for $E_{1tau} = 100E_{tau}$. The viscoelastic Young's modulus relaxation function for the 3-parameter GM is then,

$$E(t)_{tau} = E_{\infty tau} + E_{1tau}\exp\left(-\frac{t}{\tau_{1tau}}\right) \tag{4.3}$$

Where t is the time and the relaxation time for the Maxwell element is $\tau_{1tau} = \mu_{1tau}/E_{1tau} = 3.5\ ms$.

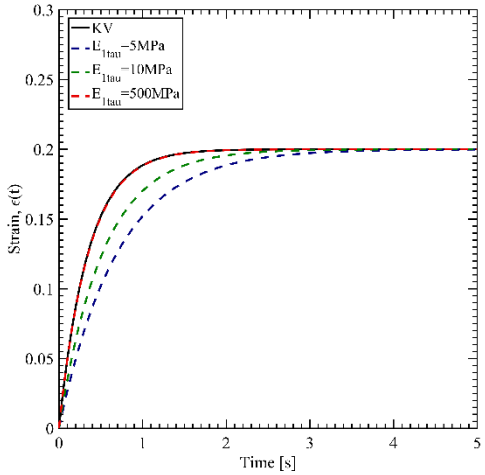

Figure 4-8 Creep response fit of 3-parameter General Maxwell to Kelvin-Voigt

Once we have estimated the values of the 3-parameter GM model for Young's modulus, then we determined the shear modulus values. Alfrey's correspondence

principle states that in the frequency domain, the viscoelastic modulus is related to the Hookean linear elastic material [167]. In the linear elastic theory, the shear modulus and Young's modulus is related by,

$$G = \frac{E}{2(1+\nu)} \tag{4.4}$$

In the above equation, G, E, and ν are shear modulus, Young's modulus, and Poisson's ratio in the linear elastic domain, respectively. In the frequency domain, the equation 4.4 is,

$$\bar{G}^*(s) = \frac{\bar{E}^*(s)}{2(1+\bar{\nu}^*(s))} \tag{4.5}$$

Where, $s = a + ib$, is a complex function. In equation 4.5, the frequency domain representation of the shear, Young's, and Poisson's ratio is related to the time domain representation of them via the Laplace transformation.

$$\bar{E}^*(s) = s\int_0^\infty \mathrm{e}^{-st}\, E(t)_{tau}dt$$

$$\bar{G}^*(s) = s\int_0^\infty \mathrm{e}^{-st}\, G(t)_{tau}dt \tag{4.6 a, b, c}$$

$$\bar{\nu}^*(s) = s\int_0^\infty \mathrm{e}^{-st}\, \nu(t)_{tau}dt$$

Considering constant Poisson's ration for tau, $\nu(t)_{tau} = 0.33$ and using equation 4.3 we get the shear relaxation modulus for tau as,

$$G(t)_{tau} = G_{\infty tau} + G_{1tau}\exp\left(-\frac{t}{\tau_{1tau}}\right) \tag{7}$$

Where long term shear modulus, $G(\infty)_{tau} = G_{\infty tau} = 1.87\ MPa$, $G_{1tau} = 187.97\ MPa$ and $\tau_{1tau} = 3.5\ ms$. The short term shear modulus is defined as, $G(0)_{tau} = G_{0tau} = G_{\infty tau} + G_{1tau} = 189.83\ MPa$.

Linear Viscoelastic Theory

In order to fully characterized the viscoelastic material properties of the axon, we have conducted relaxation tests. Relaxation test is defined as the time response of the stress as the strain remains constant. Since the viscoelastic material response is a combination of both viscous and elastic behaviors, the time-dependent stress is a function of the strain and time as,

$$\boldsymbol{\sigma} = f(\boldsymbol{\epsilon}, t) \tag{4.8}$$

Hereditary integral is used to represent the constitutive relation between the stress and strain under small deformation assumption as,

$$\sigma_{ij} = \int_0^t S_{ijkl}\,(t-\tau)\frac{d\epsilon_{kl}(\tau)}{d\tau}d\tau \qquad i,j,k,l = 1,2,3 \tag{4.9}$$

In the above equation, τ is a dummy variable and $S_{ijkl}(t)$ is the relaxation modulus. In the Voigt vector form, equation 4.9 can be represented as [184],

$$\begin{Bmatrix}\sigma_{11}(t)\\ \sigma_{22}(t)\\ \sigma_{33}(t)\\ \sigma_{23}(t)\\ \sigma_{13}(t)\\ \sigma_{12}(t)\end{Bmatrix} = \int_0^t \begin{bmatrix} S_{1111} & S_{1122} & S_{1133} & S_{1123} & S_{1113} & S_{1112}\\ S_{2211} & S_{1122} & S_{1133} & S_{2223} & S_{2213} & S_{2212}\\ S_{3311} & S_{3322} & S_{3333} & S_{3323} & S_{3313} & S_{3312}\\ S_{2311} & S_{2322} & S_{2333} & S_{2323} & S_{2313} & S_{2312}\\ S_{1311} & S_{1322} & S_{1333} & S_{1323} & S_{1313} & S_{1312}\\ S_{1211} & S_{1222} & S_{1233} & S_{1223} & S_{1213} & S_{1212}\end{bmatrix} \begin{Bmatrix} d\epsilon_{11}(\tau)/d\tau\\ d\epsilon_{22}(\tau)/d\tau\\ d\epsilon_{33}(\tau)/d\tau\\ d\epsilon_{23}(\tau)/d\tau\\ d\epsilon_{13}(\tau)/d\tau\\ d\epsilon_{12}(\tau)/d\tau\end{Bmatrix} d\tau \tag{4.10}$$

For a heterogeneous material $S_{ijkl}(t)$ is a 6x6 matrix of the relaxation modulus. However, for different material symmetry, the number of the independent relaxation function could vary between 2 to 21. For the axon microstructure, we have three

orthogonal planes of symmetry, and therefore the number of the independent relaxation function reduced to 9. In Voigt notation, they are given as,

$$\begin{Bmatrix}\sigma_1(t)\\ \sigma_2(t)\\ \sigma_3(t)\\ \sigma_4(t)\\ \sigma_5(t)\\ \sigma_6(t)\end{Bmatrix} = \int_0^t \begin{bmatrix} S_{11} & S_{12} & S_{13} & 0 & 0 & 0\\ S_{21} & S_{22} & S_{23} & 0 & 0 & 0\\ S_{31} & S_{32} & S_{33} & 0 & 0 & 0\\ 0 & 0 & 0 & S_{44} & 0 & 0\\ 0 & 0 & 0 & 0 & S_{55} & 0\\ 0 & 0 & 0 & 0 & 0 & S_{66}\end{bmatrix} \begin{Bmatrix} d\epsilon_1(\tau)/d\tau\\ d\epsilon_2(\tau)/d\tau\\ d\epsilon_3(\tau)/d\tau\\ d\epsilon_4(\tau)/d\tau\\ d\epsilon_5(\tau)/d\tau\\ d\epsilon_6(\tau)/d\tau\end{Bmatrix} d\tau \tag{4.11}$$

Due to the tensor symmetry, 9 independent relaxation functions are, S_{11}, S_{22}, S_{33}, S_{44}, S_{55}, S_{66}, $S_{12} = S_{21}$, $S_{13} = S_{31}$, and $S_{23} = S_{32}$. Each of these relaxation function can be expressed in terms of the Prony series for General Maxwell model (figure 4-9) give as [185],

$$S_{ij}(t) = S_{ij_0}(1 - \sum_{k=1}^{n} h_{ij_k}(1 - e^{-t/\tau_{ij_k}})) \tag{4.12}$$

Where,

the coefficients are defined as, $h_{ij_k} = S_{ij_k}/S_{ij_0}$

the relaxation time for each Maxwell element is, $\tau_{ij_k} = S_{ij_k}/\mu_{ij_k}$

and, the short time modulus is related to the long term modulus as, S_{ij_0}=S_{ij_∞} + $\sum_{k=1}^{n} S_{ij_k}$.

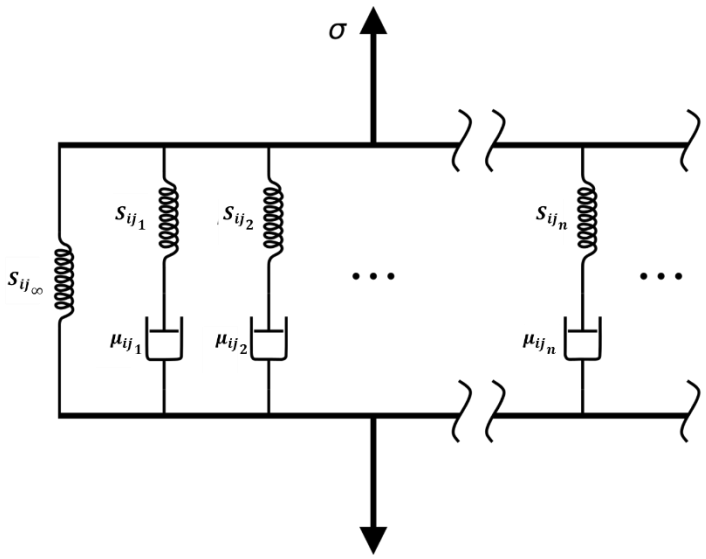

Figure 4-9 General Maxwell viscoelastic model

Figure 4-10 shows a typical relaxation loading condition. Ideally, the strain needs to step increased and kept constant for enough long time for the stress to relax. However, in practice, this is not possible, rather strain is increased in a short period of time and then kept constant for stress to relax to an asymptotic value. Therefore, the loading function is given as,

$$\epsilon_i(t) = \begin{cases} \epsilon_{i1} t/(t_1 - t_0) & for\ t_0 < t \le t_1 \\ \epsilon_{i1} & for\ t_1 < t \le t_2 \end{cases} \tag{4.13}$$

$$\frac{d\epsilon_i(t)}{dt} = \begin{cases} \epsilon_{i1}/(t_1 - t_0) & for\ t_0 < t \le t_1 \\ 0 & for\ t_1 < t \le t_2 \end{cases} \tag{4.14}$$

In the above two equations $i = 1,2,3,4,5,6$. Total 6 loading case is required to fully characterize 9 $S_{ij}(t)$ of equation 4.11. For each loading case, the simulated data is then

used to estimate the volume-averaged time-dependent stress and strain for each time-step. The volume-averaged stress and strain is defined as,

$$\sigma_i(t) = \frac{1}{V_{RVE}} \int_V [\sigma_i(t)]_k dV \tag{4.15}$$

$$\epsilon_i(t) = \frac{1}{V_{RVE}} \int_V [\epsilon_i(t)]_k dV \tag{4.16}$$

Where, V_{RVE} is the volume of the RVE. In the above two equations, the $[\sigma_i(t)]_k$, $[\epsilon_i(t)]_k$ and dV are the stress, strain, and volume, respectively, of the k^{th}-element of the finite element model. For every time step, the instantaneous volume averaged stress-strain constitutive relation is then used to estimate the relaxation function as,

$$\sigma_i(t) = S_{ij}(t)\epsilon_i(t) \tag{4.17}$$

Once the relaxation function is realized, then a nonlinear regression analysis is done to curve fit the coefficients of equation 4.12. For n number of Maxwell elements (spring and damper in series), total $2n + 1$ coefficients are needed to fit.

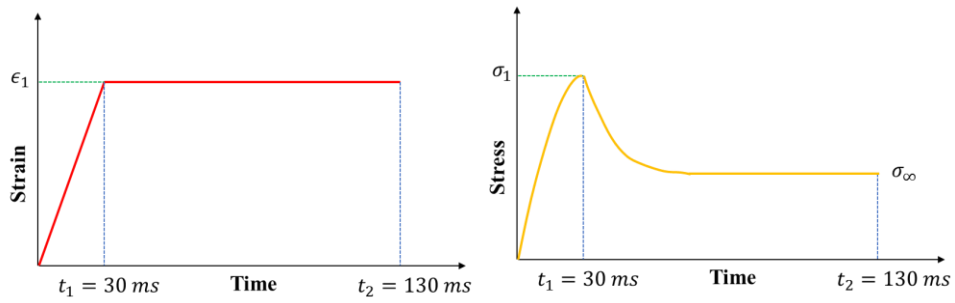

Figure 4-10 Typical relaxation test: time history of strain (left) and stress response (right).

Composite RVE Modeling

The composite representative volume element (RVE) of the axon is prepared as the finite element (FEM) micromechanical model. 4 RVEs are modeled by varying the

geometric properties. The base RVE, RVE-1, is modeled for $R_{IMT} = 7nm$, $R_{OMT} = 12.5nm$, $R_{tau} = 4nm$, $d_{MT} = 20nm$, $d_{tau} = 40nm$ and $2L = 1\mu m$ (figure 4-11). The estimated volume fraction of MT (α_{MT}) and tau (α_{tau}) are 0.192 and 0.042, respectively, for the RVE-1. Keeping all other parameters fixed, R_{tau}, d_{MT} and d_{tau} are parametrized for RVE-2, RVE-3, and RVE-4, respectively, and the details are summarized in table 4-2.

Table 4-2 RVE parameters

# RVE	Varying Parameter and value	α_{MT}	α_{tau}
RVE-2	$R_{tau} = 6nm$	0.192	0.096
RVE-3	$d_{MT} = 38nm$	0.098	0.040
RVE-4	$d_{tau} = 20nm$	0.192	0.087

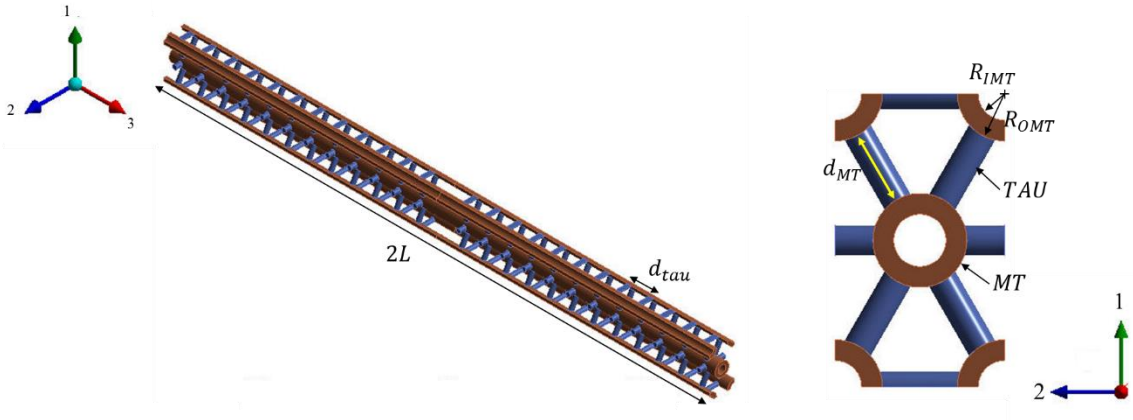

Figure 4-11 Base RVE (RVE-1) for MT and tau volume fraction of 0.192 and 0.042, respectively.

Load Cases

As discussed in equation 4-11, 6 load cases are required for complete viscoelastic material characterization of the axon RVE. Figure 4-10 shows a typical loading, and for all cases, the strain is increased for 30ms and kept constant for 130ms. Figure 4-12 shows the deformation boundary condition for the individual load case. We

have adopted the composite RVE analysis proposed by Sun et al. (1996) [186]. The first three load cases are for axial loading while the last three cases impose shear deformation.

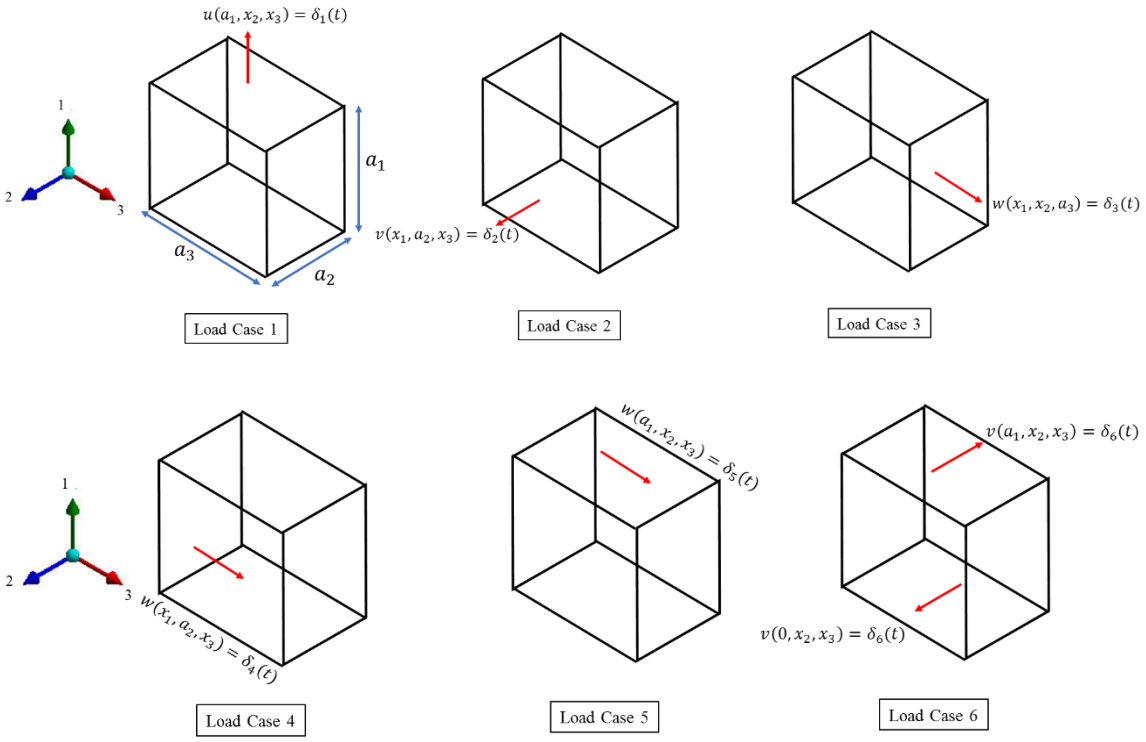

Figure 4-12 6 load cases for the viscoelastic characterization.

Load Case 1, 2 and 3

For the first three load cases, the faces at $x_1 = 0$, $x_2 = 0$ and $x_3 = 0$ are defined as the symmetric region with displacement boundary condition defined as,

$$\begin{aligned} face, x_1 = 0 \quad & u(0, x_2, x_3) = 0 \\ face, x_2 = 0 \quad & v(x_1, 0, x_3) = 0 \\ face, x_3 = 0 \quad & w(x_1, x_2, 0) = 0 \end{aligned} \tag{4.18}$$

In the above equation, x_1, x_2 and x_3 are coordinates; and u, v, and w are displacements, respectively, in the three principal coordinates shown in figure 4-12. The displacement boundary conditions for the other three faces for first three load cases are,

Load Case 1

$$\begin{aligned} face, x_1 = a_1 \quad & u(a_1, x_2, x_3) = \delta_1(t) \\ face, x_2 = a_2 \quad & v(x_1, a_2, x_3) = 0 \\ face, x_3 = a_3 \quad & w(x_1, x_2, a_3) = 0 \end{aligned} \tag{4.19}$$

Load Case 2

$$\begin{aligned} face, x_1 = a_1 \quad & u(a_1, x_2, x_3) = 0 \\ face, x_2 = a_2 \quad & v(x_1, a_2, x_3) = \delta_2(t) \\ face, x_3 = a_3 \quad & w(x_1, x_2, a_3) = 0 \end{aligned} \tag{4.20}$$

Load Case 3

$$\begin{aligned} face, x_1 = a_1 \quad & u(a_1, x_2, x_3) = 0 \\ face, x_2 = a_2 \quad & v(x_1, a_2, x_3) = 0 \\ face, x_3 = a_3 \quad & w(x_1, x_2, a_3) = \delta_3(t) \end{aligned} \tag{4.21}$$

Load Case 4,5 and 6

Three shearing deformation is implemented as,

Load Case 4

$$face, x_2 = 0 \quad u(x_1, 0, x_3) = 0$$

$$v(x_1, 0, x_3) = 0 \tag{4.22}$$

$$w(x_1, 0, x_3) = 0$$

$face, x_2 = a_2$ $\quad u(x_1, a_2, x_3) = \delta_4(t)$

Load Case 5

$$u(0, x_2, x_3) = 0$$

$face, x_1 = 0$ $\quad v(0, x_2, x_3) = 0$ (4.23)

$$w(0, x_2, x_3) = 0$$

$face, x_1 = a_1$ $\quad u(a_1, x_2, x_3) = \delta_5(t)$

Load Case 6

$$u(0, x_2, x_3) = 0$$

$face, x_1 = 0$ $\quad v(0, x_2, x_3) = \delta_6(t)$ (4.24)

$$w(0, x_2, x_3) = 0$$

$$u(a_1, x_2, x_3) = 0$$

$face, x_1 = a_1$ $\quad v(a_1, x_2, x_3) = -\delta_6(t)$ (4.25)

$$w(a_1, x_2, x_3) = 0$$

For load case 6, the rigid body constraint is implemented by fixing displacement in all directions for the center-node of the FEM model.

Prony Series Fit to the Time-Dependent Strain

Once we have the simulation data for the volume-averaged stress and strain (equation 4.15 and 4.16) for different load cases, we can utilize a formulation that can be used to fit the Prony series parameters given in equation 4.12. The hereditary integral

given in equation 4.9 will be used by substituting the strain function (equation 4.13 and 4.14) and Prony kernel (4.12).

Mathematical Formulation

For the multiple loading process, the hereditary integral is done for the two steps of loading shown in figure 4-10. Considering $\epsilon_0 = \epsilon(0) = 0$ and $t_0 = 0$ we can derive the formulation in two steps as,

Step 1: $0 < t \leq t_1$

$$\sigma_i = \epsilon_0 S_{ij}(t) + \int_0^t S_{ij}\,(t-\tau)\frac{d\epsilon_k(\tau)}{d\tau}d\tau$$

$$= \frac{S_{ij_0}\epsilon_{i1}}{t_1}\left[t - \sum_{k=1}^{n} h_{ij_k} t + \sum_{k=1}^{n} h_{ij_k}\tau_{ij_k} - \sum_{k=1}^{n} h_{ij_k}\tau_{ij_k} e^{-t/\tau_{ij_k}}\right] \qquad (4.26)$$

Step 2: $t_1 < t \leq t_2$

$$\sigma_i = \epsilon_0 S_{ij}(t) + \int_0^{t_1-} S_{ij}\,(t-\tau)\frac{d\epsilon_k(\tau)}{d\tau}d\tau + \int_{t_1+}^{t} S_{ij}\,(t-\tau)\frac{d\epsilon_k(\tau)}{d\tau}d\tau$$

$$= \frac{S_{ij_0}\epsilon_{i1}}{t_1}\left[t_1 - \sum_{k=1}^{n} h_{ij_k} t_1 + \sum_{k=1}^{n} h_{ij_k}\tau_{ij_k} e^{-(t-t_1)/\tau_{ij_k}} - \sum_{k=1}^{n} h_{ij_k}\tau_{ij_k} e^{-t/\tau_{ij_k}}\right] \qquad (4.27)$$

We have found that $n = 2$ (two Maxwell elements) can provide a good fit to the data, hence total $(2n + 1 =)\ 5$ parameters ($S_{ij_0}, h_{ij_1}, h_{ij_2}, \tau_{ij_1}\ and\ \tau_{ij_2}$) are reported for each relaxation function ($S_{ij}(t)$).

Nonlinear Regression for the Curve Fitting

The Prony series coefficients defined in equation 4.26 and 4.27 will be estimated by using the nonlinear regression method. The Marquardt-Levenberg method has been

implemented for the data fit [187]. The error function (χ^2) is minimized for unknown constant coefficients (C) in every iteration and given as [188],

$$\chi(C)^2 = \sum_{i=1}^{N_d} \left[\frac{y_i - y(x_i; C)}{\sigma_{SD_i}} \right]^2 \tag{4.28}$$

Where, N_d is the number of data points, the simulated stress, and strain data points are y_i and x_i, respectively. Function $y(x_i; C)$ is given by equation 4.26 and 4.27 for coefficient vector, $C = \{S_{ij_0}, h_{ij_1}, h_{ij_2}, \tau_{ij_1}, \tau_{ij_2}\}^T$. For the i^{th} data point the standard deviation is given by σ_{SD_i}. Initial values of vector C are defined first and then at each iteration the $\chi(C)^2$ is minimized. An improved C is estimated until $\chi(C)^2$ reach a minimum and does not change. The thermodynamic constraint for each coefficient is defined as [185],

$$S_{ij_0} > 0, \quad h_{ij_k} \geq 0, \quad \sum h_{ij_k} \leq 1 \quad and \quad \tau_{ij_k} \geq 0 \tag{4.29}$$

Results and Discussion

A total of 24 simulations have been carried out for 4 different RVEs and 6 load cases to estimate 9 different relaxation moduli of the axon for MT Young's modulus 1.5 GPa. Another 6 simulations were carried out for increased $E_{MT} = 1.9\ GPa$. Results from a total 30 simulations are discussed here.

Figure 4-13 and 4-14 show the snapshots from the load case 5 and load case 6. The displacement boundary condition is applied as shown in figure 4-12 and increased till 30ms, followed by a constant displacement until 130ms. Within 20ms, stress relaxes in both cases. The relaxation time of the axon RVE is seen to be close to 20ms for all cases and summarized below.

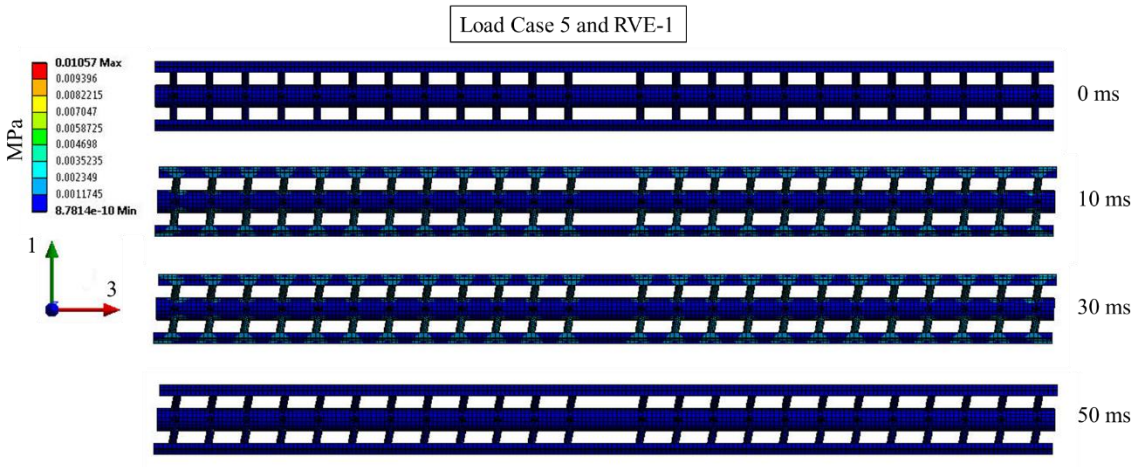

Figure 4-13 $S_{55}(t)$ estimation by imposing the load case 5. $\delta_5(t)$ is increased until $t_1 = 30ms$ and kept constant for 100 ms ($t_2 = 130\ ms$). At the $t = 50ms$ the stress relaxes while the RVE is still deformed.

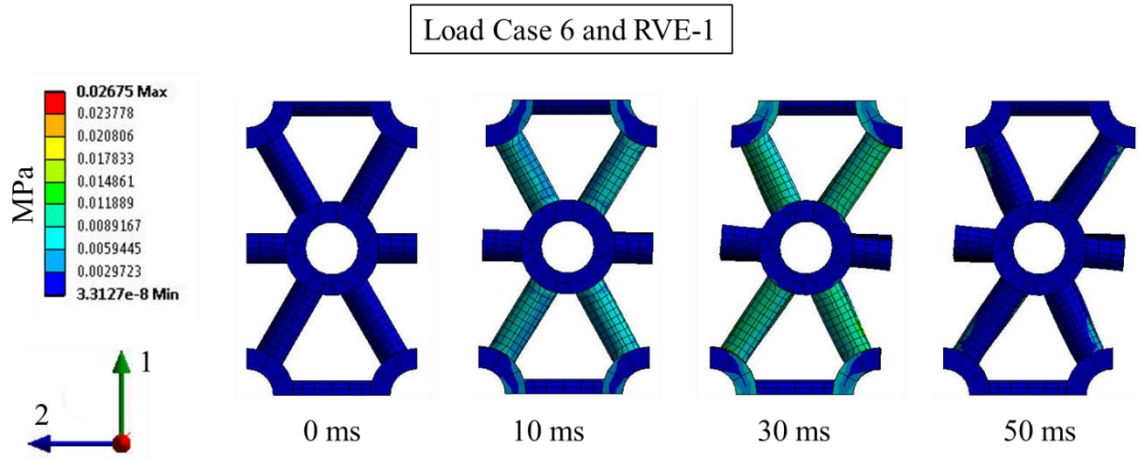

Figure 4-14 $S_{66}(t)$ estimation by imposing load case 6. $\delta_6(t)$ is increased until $t_1 = 30ms$ and kept constant for 100 ms ($t_2 = 130\ ms$). At the $t = 50ms$ the stress relaxes while the RVE is still deformed.

Total 6 load cases were needed to estimate 9 independent relaxation moduli, and figure 4-15 to 4-20 show the nonlinear regression fit to volume averaged stress with the Prony series parameters. The fitted parameters are summarized in table 4-3 to 4-7 for

different RVEs. The short time modulus (S_{ij_0}) is maximum in the longitudinal direction along with the MT orientation ($S_{33}(t)$). The effect of Young's modulus of the MT is insignificant in all relaxation moduli except $S_{33}(t)$, which is increased as E_{MT} is increased. The transverse relaxation moduli ($S_{11}(t) and\ S_{22}(t)$) and the shear relaxation moduli ($S_{44}(t)\ and\ S_{55}(t)$) are in the same order for all RVEs indicating transverse isotropy.

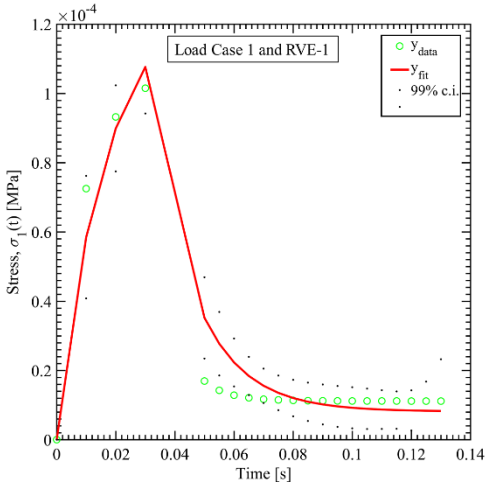

Figure 4-15 Nonlinear regression fit for the estimation of $S_{11}(t)$ from the load case 1.

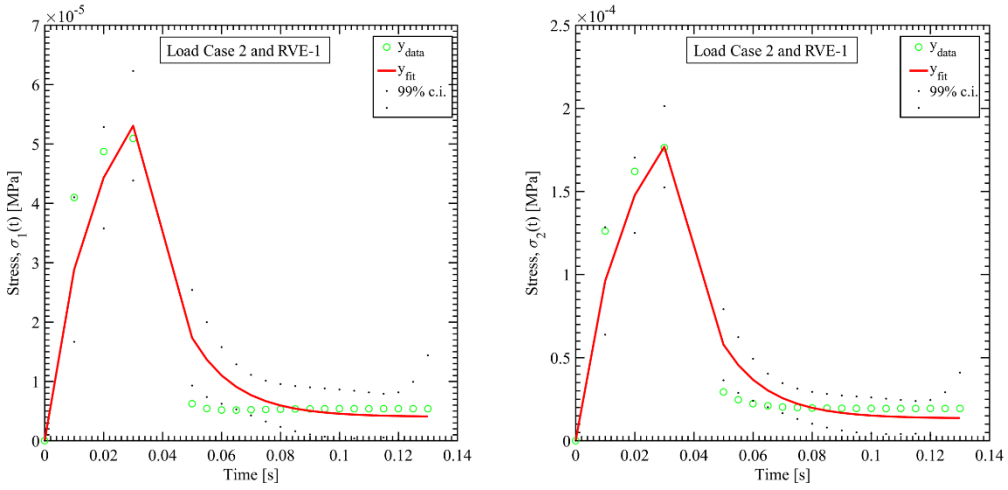

Figure 4-16 Nonlinear regression fit for the estimation of $S_{12}(t)$ (left) and $S_{22}(t)$ (right) from the load case 2.

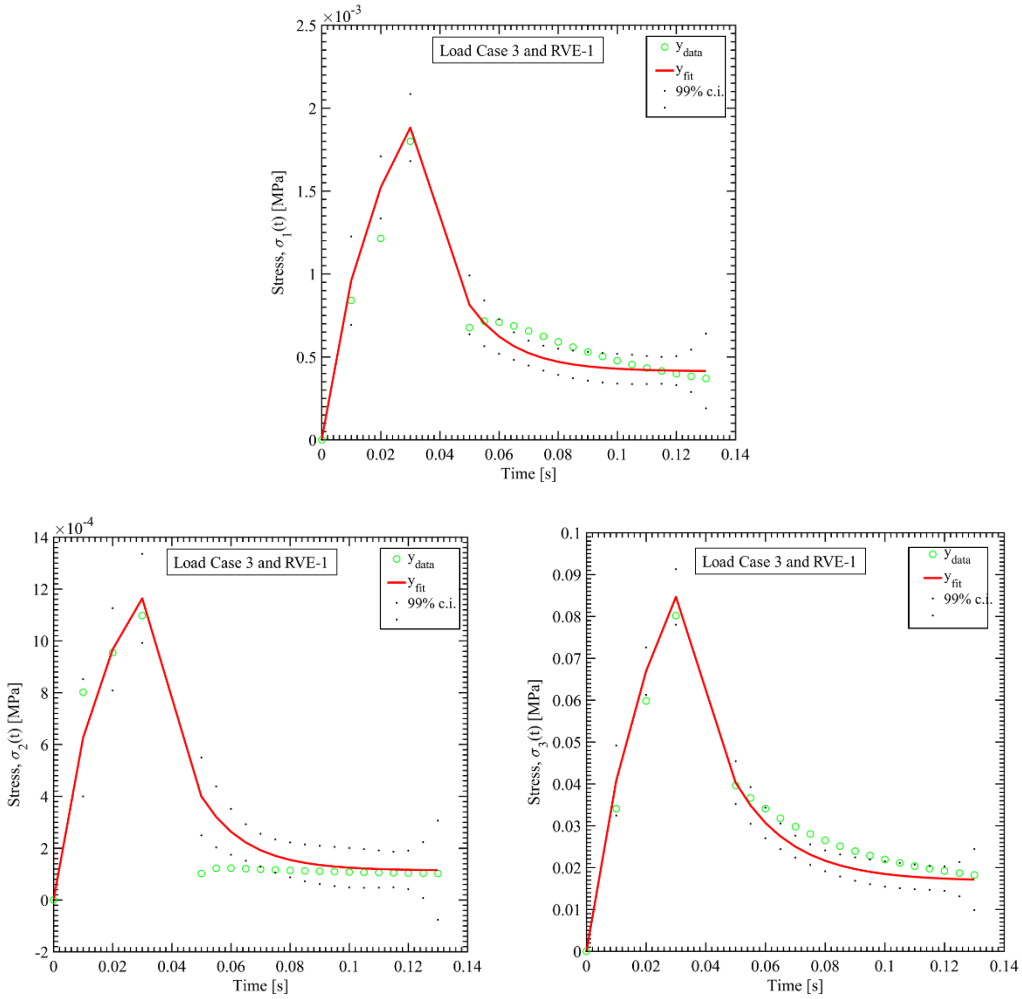

Figure 4-17 Nonlinear regression fit for the estimation of $S_{13}(t)$ (top), $S_{23}(t)$ (bottom left) and $S_{33}(t)$ (bottom right) from the load case 3.

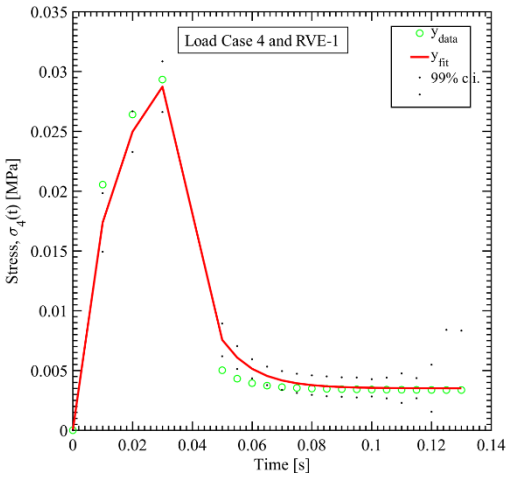

Figure 4-18 Nonlinear regression fit for the estimation of $S_{44}(t)$ from the load case 4.

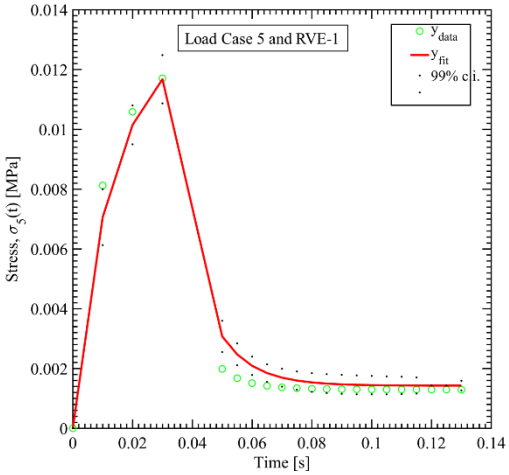

Figure 4-19 Nonlinear regression fit for the estimation of $S_{55}(t)$ from the load case 5.

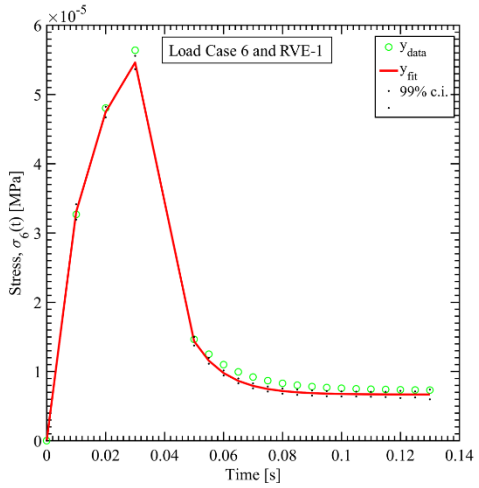

Figure 4-20 Nonlinear regression fit for the estimation of $S_{66}(t)$ from the load case 6.

Tow relaxation times are identified, one being very fast (τ_{ij_1}) in the order of a fraction of millisecond and another one (τ_{ij_2}) is in the order of a couple of milliseconds. The corresponding coefficient (h_{ij_1}) related to the short relaxation time reduce 10-15% of the stress. The Maxwell element consists of τ_{ij_1} and h_{ij_1} dictates the short-term responses of the axon RVE. The second Maxwell element ($\tau_{ij_2}\ and\ h_{ij_2}$) dominates the long-term responses and relaxes 80-85% stress. Therefore, the long term relaxation moduli are ($S_{ij}(t \to \infty) = S_{ij_0}\left(1 - \sum_{k=1}^{n} h_{ij_k}\right)$) 90-95% lower than the short term shear moduli ($S_{ij}(t = 0) = S_{ij_0}$).

Table 4-3 Prony series parameters for all $S_{ij}(t)$ for RVE-1 ($E_{MT} = 1.5\ GPa$)

	RVE-1 ($E_{MT} = 1.5\ GPa$)				
$S_{ij}(t)$	$S_{ij_0}\ [MPa]$	h_{ij_1}	h_{ij_2}	$\tau_{ij_1}[ms]$	$\tau_{ij_2}\ [ms]$
S_{11}	950	0.15	0.82	0.8	15.5
S_{12}	270	0.15	0.82	0.8	15.5
S_{22}	900	0.15	0.82	0.8	15.5
S_{13}	80	0.10	0.80	0.8	15.5
S_{23}	55	0.13	0.83	0.8	15.5
S_{33}	3250	0.10	0.80	0.8	19.0
S_{44}	310	0.13	0.83	0.7	11.0
S_{55}	310	0.13	0.83	0.7	11.0
S_{66}	310	0.13	0.83	0.7	11.0

Table 4-4 Prony series parameters for all $S_{ij}(t)$ for RVE-1 ($E_{MT} = 1.9\ GPa$)

	RVE-1 ($E_{MT} = 1.9\ GPa$)				
$S_{ij}(t)$	$S_{ij_0}\ [MPa]$	h_{ij_1}	h_{ij_2}	$\tau_{ij_1}[ms]$	$\tau_{ij_2}\ [ms]$
S_{11}	950	0.15	0.82	0.8	15.5
S_{12}	270	0.15	0.82	0.8	15.5
S_{22}	900	0.15	0.82	0.8	15.5
S_{13}	100	0.10	0.80	0.8	15.5
S_{23}	60	0.13	0.83	0.8	15.5
S_{33}	4000	0.10	0.80	0.8	19.0
S_{44}	310	0.13	0.83	0.7	11.0
S_{55}	310	0.13	0.83	0.7	11.0
S_{66}	310	0.13	0.83	0.7	11.0

Table 4-5 Prony series parameters for all $S_{ij}(t)$ for RVE-2

	RVE-2				
$S_{ij}(t)$	$S_{ij_0}\ [MPa]$	h_{ij_1}	h_{ij_2}	$\tau_{ij_1}[ms]$	$\tau_{ij_2}\ [ms]$
S_{11}	1100	0.13	0.83	0.7	11.0
S_{12}	340	0.13	0.83	0.7	11.0
S_{22}	1100	0.13	0.83	0.7	11.0
S_{13}	130	0.13	0.83	0.7	11.0
S_{23}	120	0.14	0.84	0.7	11.0
S_{33}	2800	0.05	0.65	0.8	19.0
S_{44}	310	0.13	0.83	0.7	11.0
S_{55}	310	0.13	0.83	0.7	11.0
S_{66}	250	0.13	0.83	0.7	11.0

Table 4-6 Prony series parameters for all $S_{ij}(t)$ for RVE-3

	RVE-3				
$S_{ij}(t)$	$S_{ij_0}\,[MPa]$	h_{ij_1}	h_{ij_2}	$\tau_{ij_1}[ms]$	$\tau_{ij_2}\,[ms]$
S_{11}	800	0.13	0.82	0.8	15.5
S_{12}	290	0.15	0.82	0.8	11.5
S_{22}	750	0.15	0.82	0.8	15.5
S_{13}	340	0.13	0.83	0.6	17.0
S_{23}	150	0.14	0.84	0.8	17.0
S_{33}	4500	0.13	0.83	0.8	15.0
S_{44}	280	0.13	0.83	0.7	11.0
S_{55}	270	0.13	0.83	0.7	11.0
S_{66}	270	0.13	0.83	0.7	11.0

Table 4-7 Prony series parameters for all $S_{ij}(t)$ for RVE-4

	RVE-4				
$S_{ij}(t)$	$S_{ij_0}\,[MPa]$	h_{ij_1}	h_{ij_2}	$\tau_{ij_1}[ms]$	$\tau_{ij_2}\,[ms]$
S_{11}	950	0.15	0.82	0.8	15.5
S_{12}	350	0.15	0.82	0.8	11.5
S_{22}	900	0.15	0.82	0.8	15.5
S_{13}	110	0.10	0.80	0.8	15.5
S_{23}	110	0.13	0.83	0.8	11.5
S_{33}	2900	0.05	0.75	1.0	25.0
S_{44}	310	0.13	0.83	0.7	11.0
S_{55}	310	0.13	0.83	0.7	11.0
S_{66}	310	0.13	0.83	0.7	11.0

Figure 4-21 to 4-26 compare all each relaxation modulus for different RVEs. In RVE-2 and RVE-4 the volume fraction of tau (α_{tau}) is increased by increasing the radius of tau cross-section (R_{tau}) and tau spacing (d_{tau}), respectively. In RVE-3 the volume fraction of MT (α_{MT}) is reduced by increasing the MT spacing (d_{MT}). The effect of increasing tau volume fraction is prominent in transverse loading case (1 and 2) and shows increasing short term modulus ($S_{11}(t), S_{12}(t)\ and\ S_{22}(t)$) as α_{tau} is increased (figure 4-21 and 4-22). For the longitudinal loading case (load case 3) the effect of decreasing MT volume fraction is dominant, and more stiffness is shown for decreasing α_{MT} (figure 4-23). The shear responses of the axon RVE are identical for all RVEs

indicating no or little effect of the MT and tau volume fraction (figure 4-24, 4-25, and 4-26).

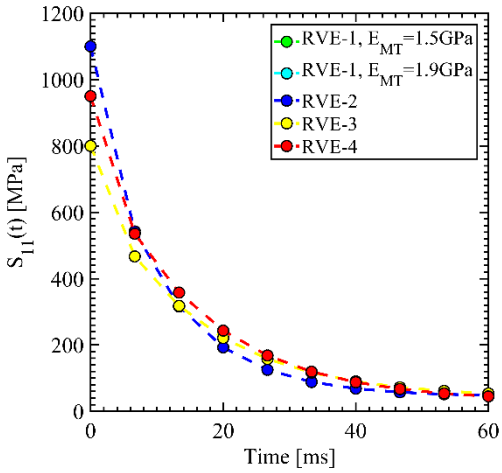

Figure 4-21 Comparison of $S_{11}(t)$ for different RVE (Load Case 1)

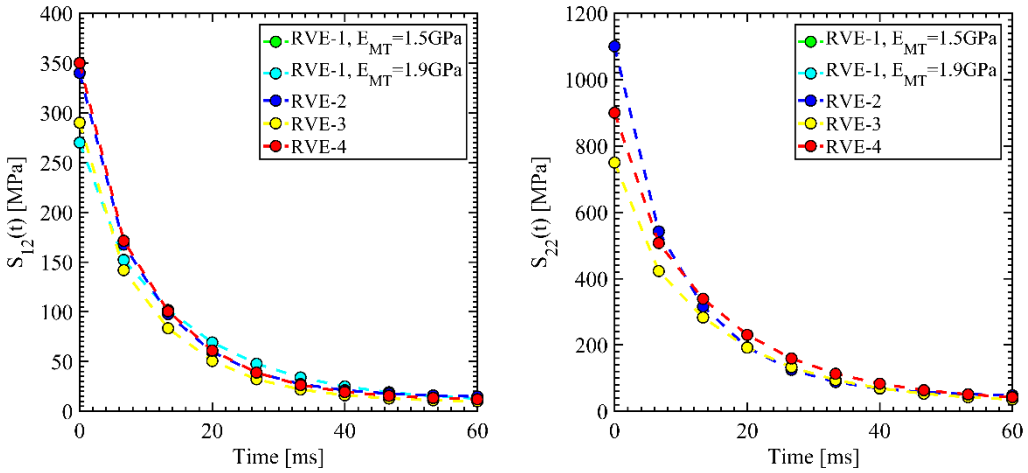

Figure 4-22 Comparison of $S_{12}(t)$ (left) and $S_{22}(t)$ (right) for different RVE (Load Case 2)

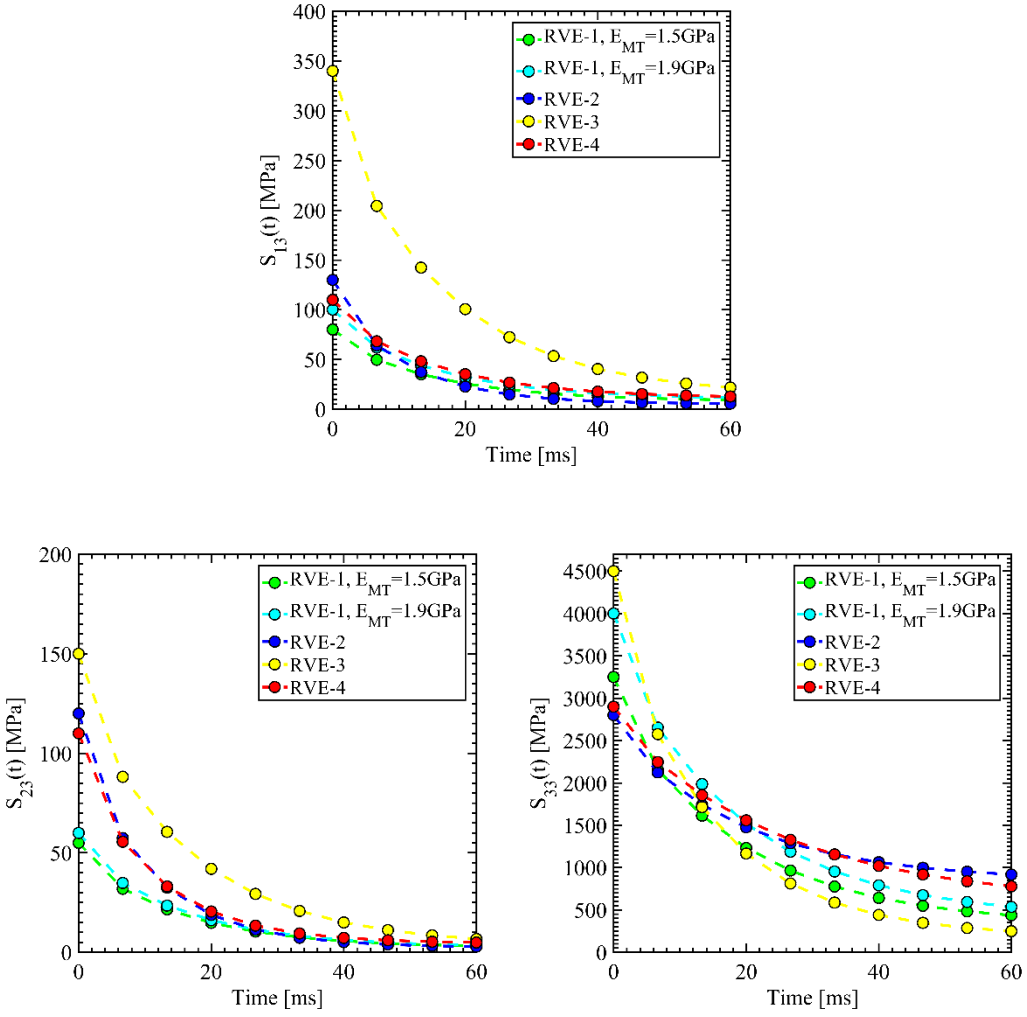

Figure 4-23 Comparison of $S_{13}(t)$ (top), $S_{23}(t)$ (bottom left) and $S_{33}(t)$ (bottom right) for different RVE (Load Case 3)

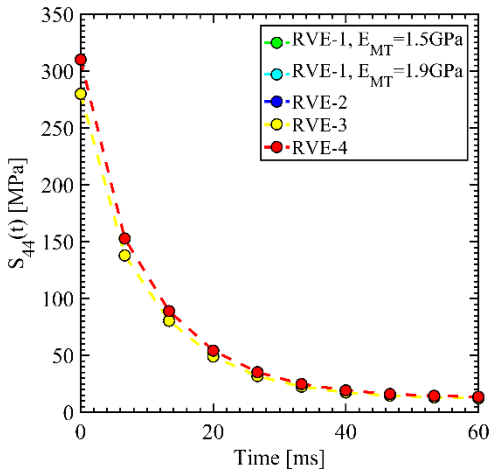

Figure 4-24 Comparison of $S_{44}(t)$ for different RVE (Load Case 4)

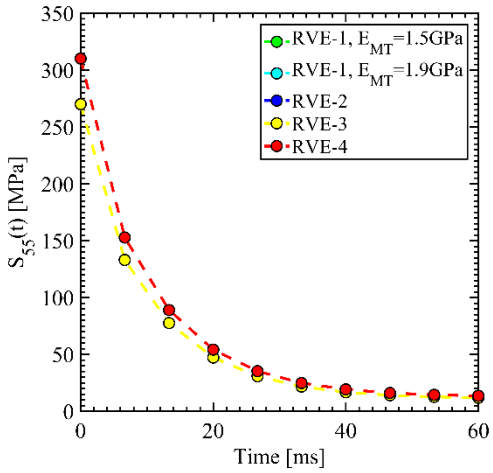

Figure 4-25 Comparison of $S_{55}(t)$ for different RVE (Load Case 5)

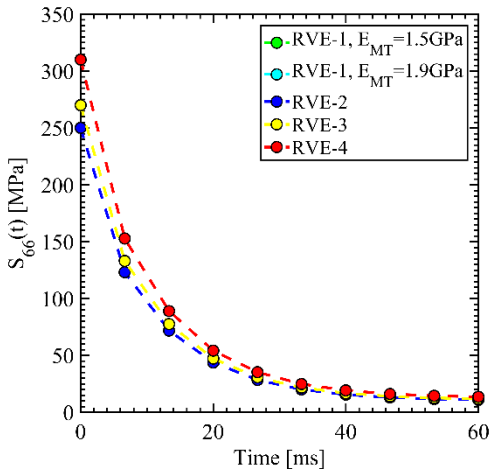

Figure 4-26 Comparison of $S_{66}(t)$ for different RVE (Load Case 6)

Finally, figure 4-27 shows all 9 relaxation moduli from RVE-1 and indicates that although the RVE is orthotropic due to the hexagonal orientation of the MTs, the relaxation matrix is transverse isotropic. From figure 4-27, $S_{11}(t) = S_{22}(t)$, $S_{44}(t) = S_{55}(t)$ and $S_{13}(t) = S_{23}(t)$. Therefore, we can conclude that there are 6 distinct relaxation moduli in which 5 are independent ($S_{11}(t), S_{33}(t), S_{44}(t), S_{66}(t)\ and\ S_{13}(t)$). The relaxation matrix can be written as,

$$S_{ij}(t) = \begin{bmatrix} S_{11} & S_{12} & S_{13} & 0 & 0 & 0 \\ S_{12} & S_{11} & S_{13} & 0 & 0 & 0 \\ S_{13} & S_{13} & S_{33} & 0 & 0 & 0 \\ 0 & 0 & 0 & S_{44} & 0 & 0 \\ 0 & 0 & 0 & 0 & S_{44} & 0 \\ 0 & 0 & 0 & 0 & 0 & S_{66} \end{bmatrix} \tag{4.30}$$

In the frequency domain S_{12} is related to S_{11} and S_{66} as,

$$\bar{S}_{12}{}^{*}(s) = \bar{S}_{11}{}^{*}(s) - 2\bar{S}_{66}{}^{*}(s) \tag{4.31}$$

In the above equation $\bar{S}_{11}{}^{*}(s)$ and $\bar{S}_{66}{}^{*}(s)$ can be estimated as shown in equation 4.6.

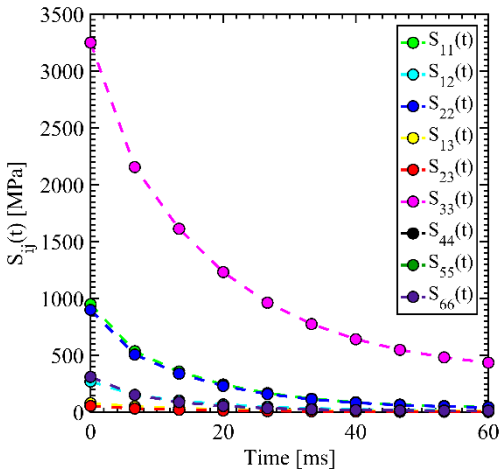

Figure 4-27 Transverse isotropy with 5 independent relaxation moduli.

References

[1] C. E. Brennen, *Cavitation and bubble dynamics*. 2013.

[2] A. Andersen and K. A. Mørch, “Cavitation nuclei in water exposed to transient pressures,” *J. Fluid Mech.*, vol. 771, pp. 424–448, 2015.

[3] T. G. Leighton, “The principles of cavitation,” *Ultrasound food Process.*, vol. 12, 1998.

[4] M. S. Plesset, “The dynamics of cavitation bubbles,” *J. Appl. Mech.*, vol. 16, pp. 277–282, 1949.

[5] M. S. Plesset and A. Prosperetti, “Bubble dynamics and cavitation,” *Annu. Rev. Fluid Mech.*, vol. 9, no. 1, pp. 145–185, 1977.

[6] A. Prosperetti, “A generalization of the Rayleigh–Plesset equation of bubble dynamics,” *Phys. Fluids*, vol. 25, no. 3, pp. 409–410, 1982.

[7] Lord Rayleigh, “VIII. On the pressure developed in a liquid during the collapse of a spherical cavity,” *London, Edinburgh, Dublin Philos. Mag. J. Sci.*, vol. 34, no. 200, pp. 94–98, 1917, doi: 10.1080/14786440808635681.

[8] E. JOHNSEN and T. COLONIUS, “Numerical simulations of non-spherical bubble collapse,” *J. Fluid Mech.*, vol. 629, no. 1, pp. 231–262, Jun. 2009, doi: 10.1017/S0022112009006351.

[9] J. Goeller, A. Wardlaw, D. Treichler, J. O’Bruba, and G. Weiss, “Investigation of Cavitation as a Possible Damage Mechanism in Blast-Induced Traumatic Brain Injury,” *J. Neurotrauma*, vol. 29, no. 10, pp. 1970–1981, 2012, doi: 10.1089/neu.2011.2224.

[10] A. Nakagawa *et al.*, “Mechanisms of Primary Blast-Induced Traumatic Brain Injury: Insights from Shock-Wave Research,” *J. Neurotrauma*, vol. 28, no. 6, pp. 1101–1119, Jun. 2011, doi: 10.1089/neu.2010.1442.

[11] P. A. Taylor, J. S. Ludwigsen, and C. C. Ford, “Investigation of blast-induced traumatic brain injury,” *Brain Inj.*, vol. 28, no. 7, pp. 879–895, Jan. 2014, doi: 10.3109/02699052.2014.888478.

[12] L. Zhang, K. H. Yang, and A. I. King, “Comparison of brain responses between frontal and lateral impacts by finite element modeling,” *J. Neurotrauma*, vol. 18, no. 1, pp. 21–30, 2001, doi: 10.1089/089771501750055749.

[13] L. Zhang, K. H. Yang, and A. I. King, “A proposed injury threshold for mild traumatic brain injury,” *J. Biomech. Eng.*, vol. 126, no. 2, pp. 226–236, 2004, doi: 10.1115/1.1691446.

[14] W. Yuan-Ting and A. Adnan, “Effect of Shock-Induced Cavitation Bubble Collapse on the damage in the Simulated Perineuronal Net of the Brain,” *Sci. Reports (Nature Publ. Group)*, vol. 7, pp. 1–9, 2017, doi: http://dx.doi.org/10.1038/s41598-017-05790-3.

[15] J. A. Zimberlin *et al.*, “Cavitation rheology for soft materials,” *Soft Matter*, vol. 3, no. 6, p. 763, 2007, doi: 10.1039/b617050a.

[16] J. B. Estrada, C. Barajas, D. L. Henann, E. Johnsen, and C. Franck, “High strain-rate soft material characterization via inertial cavitation,” *J. Mech. Phys. Solids*, vol. 112, pp. 291–317, 2018.

[17] W. Kang, A. Adnan, T. O’Shaughnessy, and A. Bagchi, “Cavitation nucleation in gelatin: Experiment and mechanism,” *Acta Biomater.*, vol. 67, pp. 295–306, 2018, doi: https://doi.org/10.1016/j.actbio.2017.11.030.

[18] C. C. Coussios and R. A. Roy, “Applications of acoustics and cavitation to noninvasive therapy and drug delivery,” *Annu. Mech.*, vol. 40, pp. 395–420, 2008.

[19] G. A. Husseini, M. A. D. de la Rosa, E. S. Richardson, D. A. Christensen, and W. G. Pitt, “The role of cavitation in acoustically activated drug delivery,” *J. Control.*

Release, vol. 107, no. 2, pp. 253–261, 2005.

[20] S. Mitragotri, “Healing sound: the use of ultrasound in drug delivery and other therapeutic applications,” *Nat. Rev. Drug Discov.*, vol. 4, no. 3, p. 255, 2005.

[21] W. G. Pitt, G. A. Husseini, and B. J. Staples, “Ultrasonic drug delivery–a general review,” *Expert Opin. Drug Deliv.*, vol. 1, no. 1, pp. 37–56, 2004.

[22] C. C. Church, “A theoretical study of cavitation generated by an extracorporeal shock wave lithotripter,” *J. Acoust. Soc. Am.*, vol. 86, no. 1, pp. 215–227, 1989.

[23] A. J. Coleman, J. E. Saunders, L. A. Crum, and M. Dyson, “Acoustic cavitation generated by an extracorporeal shockwave lithotripter,” *Ultrasound Med. Biol.*, vol. 13, no. 2, pp. 69–76, 1987.

[24] Y. A. Pishchalnikov *et al.*, “Cavitation bubble cluster activity in the breakage of kidney stones by lithotripter shockwaves,” *J. Endourol.*, vol. 17, no. 7, pp. 435–446, 2003.

[25] V. P. Carey, *Liquid-vapor phase-change phenomena: an introduction to the thermophysics of vaporization and condensation processes in heat transfer equipment*. CRC Press, 2020.

[26] C. C. Church, “Spontaneous homogeneous nucleation, inertial cavitation and the safety of diagnostic ultrasound,” *Ultrasound Med. Biol.*, vol. 28, no. 10, pp. 1349–1364, 2002, doi: 10.1016/S0301-5629(02)00579-3.

[27] J. Herbertz, “Spontaneous cavitation in liquids free of nuclei,” *Fortschritte der Akust. DAGA*, vol. 14, p. 439, 1988.

[28] M. S. Plesset, “Shockwaves from cavity collapse,” *Philos. Trans. R. Soc. London.Series A, Math. Phys. Sci.*, pp. 241–244, 1966.

[29] W.-J. Yang and H.-C. Yeh, “Theoretical study of bubble dynamics in purely viscous fluids,” *AIChE J.*, vol. 12, no. 5, pp. 927–931, 1966, doi:

10.1002/aic.690120517.

[30] A. Balasubramanya, S. Kohlstädt, and H. Nilsson, “Viscoelasticity and constitutive relations,” 2016.

[31] M. T. Warnez and E. Johnsen, “Numerical modeling of bubble dynamics in viscoelastic media with relaxation,” *Phys. Fluids*, vol. 27, no. 6, p. 63103, 2015, doi: 10.1063/1.4922598.

[32] B. Dollet, P. Marmottant, and V. Garbin, “Bubble dynamics in soft and biological matter,” *Annu. Rev. Fluid Mech.*, vol. 51, pp. 331–355, 2019.

[33] X. Yang and C. C. Church, “A model for the dynamics of gas bubbles in soft tissue,” *J. Acoust. Soc. Am.*, vol. 118, no. 6, pp. 3595–3606, 2005, doi: 10.1121/1.2118307.

[34] R. Gaudron, M. T. Warnez, and E. Johnsen, “Bubble dynamics in a viscoelastic medium with nonlinear elasticity,” *J. Fluid Mech.*, vol. 766, pp. 54–75, 2015, doi: http://dx.doi.org/10.1017/jfm.2015.7.

[35] T. B. Benjamin and A. T. Ellis, “The collapse of cavitation bubbles and the pressures thereby produced against solid boundaries,” *Philos. Trans. R. Soc. London.Series A, Math. Phys. Sci.*, pp. 221–240, 1966.

[36] J. R. Blake and D. C. Gibson, “Cavitation Bubbles Near Boundaries,” *Annu. Rev. Fluid Mech.*, vol. 19, no. 1, pp. 99–123, 1987, doi: 10.1146/annurev.fluid.19.1.99.

[37] S. Fujikawa and T. Akamatsu, “Effects of the non-equilibrium condensation of vapour on the pressure wave produced by the collapse of a bubble in a liquid,” *J. Fluid Mech.*, vol. 97, no. 3, pp. 481–512, 1980, doi: 10.1017/S0022112080002662.

[38] R. Hicking, M. S. Plesset, R. Hickling, and M. S. Plesset, “Collapse and rebound of a spherical bubble in water,” *Phys. Fluids*, vol. 7, no. 1, pp. 7–14, 1964, doi:

10.1063/1.1711058.

[39] J. B. Keller and M. Miksis, “Bubble oscillations of large amplitude,” *J. Acoust. Soc. Am.*, vol. 68, no. 2, pp. 628–633, 1980.

[40] E. Lauer, X. Y. Hu, S. Hickel, and N. A. Adams, “Numerical modelling and investigation of symmetric and asymmetric cavitation bubble dynamics,” *Comput. Fluids*, vol. 69, pp. 1–19, 2012.

[41] A. Pearson, E. Cox, J. R. Blake, and S. R. Otto, “Bubble interactions near a free surface,” *Eng. Anal. Bound. Elem.*, vol. 28, no. 4, pp. 295–313, 2004.

[42] A. Prosperetti and A. Lezzi, “Bubble dynamics in a compressible liquid. Part 1. First-order theory,” *J. Fluid Mech.*, vol. 168, no. 1, p. 457, Jul. 1986, doi: 10.1017/S0022112086000460.

[43] A. Shima, K. Takayama, Y. Tomita, and N. Ohsawa, “Mechanism of impact pressure generation from spark-generated bubble collapse near a wall,” *AIAA J.*, 1983, doi: 10.2514/3.8027.

[44] H. Kimoto, “EXPERIMENTAL EVALUATION OF THE EFFECTS OF A WATER MICROJET AND A SHOCK WAVE BY A LOCAL PRESSURE SENSOR.,” in *American Society of Mechanical Engineers, Fluids Engineering Division (Publication) FED*, 1987.

[45] C. Ward, M. Chan, and A. Nahum, “Intracranial pressure—a brain injury criterion,” *SAE Trans.*, pp. 3867–3880, 1980.

[46] H. S. Kang, R. Willinger, B. M. Diaw, and B. Chinn, “Validation of a 3D anatomic human head model and replication of head impact in motorcycle accident by finite element modeling,” in *Stapp Car Crash Conference Proceedings*, 1997.

[47] R. Anderson *et al.*, “Mechanisms of Axonal Injury: an Experimental and Numerical Study of Sheep Model of Head Impact,” in *Proceedings of the International*

Research Council on Biomechanics of Injury (IRCOBI) Conference, 1999.

[48] E. G. Takhounts, R. H. Eppinger, J. Q. Campbell, R. E. Tannous, E. D. Power, and L. S. Shook, “On the Development of the SIMon Finite Element Head Model,” in *SAE Technical Papers*, 2003, doi: 10.4271/2003-22-0007.

[49] S. Kleiven, “Predictors for traumatic brain injuries evaluated through accident reconstructions.,” *Stapp Car Crash J.*, 2007.

[50] J. Yao, J. Yang, and D. Otte, “Investigation of head injuries by reconstructions of real-world vehicle-versus-adult-pedestrian accidents,” *Saf. Sci.*, 2008, doi: 10.1016/j.ssci.2007.06.021.

[51] C. Deck and R. Willinger, “Improved head injury criteria based on head FE model,” *Int. J. Crashworthiness*, 2008, doi: 10.1080/13588260802411523.

[52] X. Trosseille, C. Tarriére, F. Lavaste, F. Guillon, and A. Domont, “Development of a F.E.M. of the human head according to a specific test protocol,” in *SAE Technical Papers*, 1992, doi: 10.4271/922527.

[53] S. S. Margulies and L. E. Thibault, “A proposed tolerance criterion for diffuse axonal injury in man,” *J. Biomech.*, 1992, doi: 10.1016/0021-9290(92)90231-O.

[54] D. I. Shreiber *et al.*, “Experimental investigation of cerebral contusion: Histopathological and immunohistochemical evaluation of dynamic cortical deformation,” *J. Neuropathol. Exp. Neurol.*, 1999, doi: 10.1097/00005072-199902000-00005.

[55] D. C. VIANO and P. LOVSUND, “Biomechanics of Brain and Spinal-Cord Injury: Analysis of Neuropathologic and Neurophysiology Experiments,” *J. Crash Prev. Inj. Control*, 1999, doi: 10.1080/10286589908915739.

[56] A. I. King, K. H. Yang, L. Zhang, and W. Hardy, “Is head injury caused by linear or angular acceleration?,” in *Proceedings of the International Research Conference*

on the Biomechanics of Impacts (IRCOBI), 2003.

[57] D. C. Viano, I. R. Casson, E. J. Pellman, L. Zhang, A. I. King, and K. H. Yang, "Concussion in professional football: Brain responses by finite element analysis: Part 9," *Neurosurgery*, 2005, doi: 10.1227/01.NEU.0000186950.54075.3B.

[58] P. Movahed, W. Kreider, A. D. Maxwell, S. B. Hutchens, and J. B. Freund, "Cavitation-induced damage of soft materials by focused ultrasound bursts: A fracture-based bubble dynamics model," *J. Acoust. Soc. Am.*, vol. 140, no. 2, pp. 1374–1386, 2016, doi: 10.1121/1.4961364.

[59] F. G. Blake Jr, "THE TENSILE STRENGTH OF LIQUIDS: A REVIEW OF THE LITERATURE. Technical Memo No. 9," 1949.

[60] A. N. Gent and P. B. Lindley, "Tension flaws in bonded cylinders of soft rubber," *Rubber Chem. Technol.*, vol. 31, no. 2, pp. 393–394, 1958.

[61] J. M. Ball, "Discontinuous equilibrium solutions and cavitation in nonlinear elasticity," *Philos. Trans. R. Soc. London. Ser. A, Math. Phys. Sci.*, vol. 306, no. 1496, pp. 557–611, 1982.

[62] C. O. Horgan and R. Abeyaratne, "A bifurcation problem for a compressible nonlinearly elastic medium: growth of a micro-void," *J. Elast.*, vol. 16, no. 2, pp. 189–200, 1986.

[63] C. O. Horgan and D. A. Polignone, "Cavitation in nonlinearly elastic solids: A review," *Appl. Mech. Rev.*, vol. 48, no. 8, pp. 471–485, 1995, doi: 10.1115/1.3005108.

[64] A. N. Gent and D. A. Tompkins, "Nucleation and Growth of Gas Bubbles in Elastomers," *J. Appl. Phys.*, vol. 40, no. 6, pp. 2520–2525, May 1969, doi: 10.1063/1.1658026.

[65] C. Fond, "Cavitation criterion for rubber materials: A review of void-growth

models," *J. Polym. Sci. Part B Polym. Phys.*, vol. 39, no. 17, pp. 2081–2096, 2001, doi: 10.1002/polb.1183.

[66] A. N. Gent and C. Wang, "Fracture mechanics and cavitation in rubber-like solids," *J. Mater. Sci.*, vol. 26, no. 12, pp. 3392–3395, Jun. 1991, doi: 10.1007/BF01124691.

[67] A. A. Griffith, "VI. The phenomena of rupture and flow in solids," *Philos. Trans. R. Soc. london. Ser. A, Contain. Pap. a Math. or Phys. character*, vol. 221, no. 582–593, pp. 163–198, 1921.

[68] A. N. Gent, "Cavitation in Rubber: A Cautionary Tale," *Rubber Chem. Technol.*, vol. 63, no. 3, pp. 49–53, 1990, doi: 10.5254/1.3538266.

[69] M. L. Williams and R. A. Schapery, "Spherical flaw instability in hydrostatic tension," *Int. J. Fract. Mech.*, vol. 1, no. 1, pp. 64–72, 1965, doi: 10.1007/BF00184154.

[70] Y. Lev and K. Y. Volokh, "On Cavitation in Rubberlike Materials," *J. Appl. Mech. Trans. ASME*, vol. 83, no. 4, pp. 1–4, 2016, doi: 10.1115/1.4032377.

[71] A. Faye, J. A. Rodríguez-Martínez, and K. Y. Volokh, "Spherical void expansion in rubber-like materials: The stabilizing effects of viscosity and inertia," *Int. J. Non. Linear. Mech.*, vol. 92, no. March, pp. 118–126, 2017, doi: 10.1016/j.ijnonlinmec.2017.04.005.

[72] O. Lopez-Pamies, M. I. Idiart, and T. Nakamura, "Cavitation in elastomeric solids: I - A defect-growth theory," *J. Mech. Phys. Solids*, vol. 59, no. 8, pp. 1464–1487, 2011, doi: 10.1016/j.jmps.2011.04.015.

[73] O. Lopez-Pamies, T. Nakamura, and M. I. Idiart, "Cavitation in elastomeric solids: II—Onset-of-cavitation surfaces for Neo-Hookean materials," *J. Mech. Phys. Solids*, vol. 59, no. 8, pp. 1488–1505, Aug. 2011, doi:

10.1016/j.jmps.2011.04.016.

[74] A. Kumar, D. Aranda-Iglesias, and O. Lopez-Pamies, “Some Remarks on the Effects of Inertia and Viscous Dissipation in the Onset of Cavitation in Rubber,” *J. Elast.*, vol. 126, no. 2, pp. 201–213, 2017, doi: 10.1007/s10659-016-9589-y.

[75] V. Lefèvre, K. Ravi-Chandar, and O. Lopez-Pamies, “Cavitation in rubber: an elastic instability or a fracture phenomenon?,” *Int. J. Fract.*, vol. 192, no. 1, pp. 0–23, 2015, doi: 10.1007/s10704-014-9982-0.

[76] L. R. G. Treloar, “The Physics of Rubber Elasticity,” *Oxford Univ. Press*, 1975.

[77] R. H. Pritchard, Y. Y. Shery Huang, and E. M. Terentjev, “Mechanics of biological networks: From the cell cytoskeleton to connective tissue,” *Soft Matter*, vol. 10, no. 12. pp. 1864–1884, 2014, doi: 10.1039/c3sm52769g.

[78] M. Blander and J. L. Katz, “Bubble nucleation in liquids,” *AIChE J.*, vol. 21, no. 5, pp. 833–848, Sep. 1975, doi: 10.1002/aic.690210502.

[79] J. H. Lienhard and A. Karim, “Homogeneous nucleation and the spinodal line,” *J. Heat Transfer*, vol. 103, no. 1, pp. 61–64, 1981, doi: 10.1115/1.3244431.

[80] L. Bernath, “Theory of Bubble Formation in Liquids.,” *Ind. Eng. Chem.*, vol. 44, no. 6, pp. 1310–1313, 1952, doi: 10.1021/ie50510a037.

[81] R. C. Picu, “Mechanics of random fiber networks - A review,” *Soft Matter*, vol. 7, no. 15. pp. 6768–6785, 2011, doi: 10.1039/c1sm05022b.

[82] C. P. Broedersz and F. C. Mackintosh, “Modeling semiflexible polymer networks,” *Rev. Mod. Phys.*, vol. 86, no. 3, pp. 995–1036, 2014, doi: 10.1103/RevModPhys.86.995.

[83] K. Linka, M. Hillgärtner, and M. Itskov, “Fatigue of soft fibrous tissues: Multi-scale mechanics and constitutive modeling,” *Acta Biomater.*, vol. 71, pp. 398–410, 2018, doi: 10.1016/j.actbio.2018.03.010.

[84] M. Hillgärtner, K. Linka, and M. Itskov, “Worm-like chain model extensions for highly stretched tropocollagen molecules,” *J. Biomech.*, vol. 80, pp. 129–135, 2018, doi: 10.1016/j.jbiomech.2018.08.034.

[85] A. Kabla and L. Mahadevan, “Nonlinear mechanics of soft fibrous networks,” *J. R. Soc. Interface*, vol. 4, no. 12, pp. 99–106, 2007, doi: 10.1098/rsif.2006.0151.

[86] E. Kuhl, K. Garikipati, E. M. Arruda, and K. Grosh, “Remodeling of biological tissue: Mechanically induced reorientation of a transversely isotropic chain network,” *J. Mech. Phys. Solids*, vol. 53, no. 7, pp. 1552–1573, Jul. 2005, doi: 10.1016/j.jmps.2005.03.002.

[87] J. E. Bischoff, E. A. Arruda, and K. Grosh, “A microstructurally based orthotropic hyperelastic constitutive law,” *J. Appl. Mech. Trans. ASME*, vol. 69, no. 5, pp. 570–579, 2002, doi: 10.1115/1.1485754.

[88] M. E. Susilo, B. A. Roeder, S. L. Voytik-Harbin, K. Kokini, and E. A. Nauman, “Development of a three-dimensional unit cell to model the micromechanical response of a collagen-based extracellular matrix,” *Acta Biomater.*, vol. 6, no. 4, pp. 1471–1486, Apr. 2010, doi: 10.1016/j.actbio.2009.11.014.

[89] G. A. Holzapfel and R. W. Ogden Editors, *Biomechanics: Trends in Modeling and Simulation*. 2014.

[90] S. P. Lake, M. F. Hadi, V. K. Lai, and V. H. Barocas, “Mechanics of a Fiber Network Within a Non-Fibrillar Matrix: Model and Comparison with Collagen-Agarose Co-gels,” *Ann. Biomed. Eng.*, vol. 40, no. 10, pp. 2111–2121, Oct. 2012, doi: 10.1007/s10439-012-0584-6.

[91] R. C. Picu, S. Deogekar, and M. R. Islam, “Poisson’s Contraction and Fiber Kinematics in Tissue: Insight from Collagen Network Simulations,” *J. Biomech. Eng.*, vol. 140, no. 2, pp. 1–12, 2018, doi: 10.1115/1.4038428.

[92] L. Zhang, S. P. Lake, V. K. Lai, C. R. Picu, V. H. Barocas, and M. S. Shephard, “A coupled fiber-matrix model demonstrates highly inhomogeneous microstructural interactions in soft tissues under tensile load,” *J. Biomech. Eng.*, vol. 135, no. 1, pp. 1–9, 2013, doi: 10.1115/1.4023136.

[93] A. M. Stein, D. A. Vader, D. A. Weitz, and L. M. Sander, “The micromechanics of three-dimensional collagen-I gels,” *Complexity*, vol. 16, no. 4, pp. 22–28, 2011.

[94] A. M. STEIN, D. A. VADER, L. M. JAWERTH, D. A. WEITZ, and L. M. SANDER, “An algorithm for extracting the network geometry of three-dimensional collagen gels,” *J. Microsc.*, vol. 232, no. 3, pp. 463–475, Dec. 2008, doi: 10.1111/j.1365-2818.2008.02141.x.

[95] B. Lee *et al.*, “A three-dimensional computational model of collagen network mechanics,” *PLoS One*, vol. 9, no. 11, pp. 1–12, 2014, doi: 10.1371/journal.pone.0111896.

[96] P. L. Chandran, T. Stylianopoulos, and V. H. Barocas, “Microstructure-Based, Multiscale Modeling for the Mechanical Behavior of Hydrated Fiber Networks,” *Multiscale Model. Simul.*, vol. 7, no. 1, pp. 22–43, Jan. 2008, doi: 10.1137/070689504.

[97] P. L. Chandran and V. H. Barocas, “Affine Versus Non-Affine Fibril Kinematics in Collagen Networks: Theoretical Studies of Network Behavior,” *J. Biomech. Eng.*, vol. 128, no. 2, pp. 259–270, Apr. 2006, doi: 10.1115/1.2165699.

[98] D. A. Head, A. J. Levine, and F. C. MacKintosh, “Distinct regimes of elastic response and deformation modes of cross-linked cytoskeletal and semiflexible polymer networks,” *Phys. Rev. E*, vol. 68, no. 6, p. 61907, 2003.

[99] S. B. Lindström, A. Kulachenko, L. M. Jawerth, and D. A. Vader, “Finite-strain, finite-size mechanics of rigidly cross-linked biopolymer networks,” *Soft Matter*, vol.

9, no. 30, pp. 7302–7313, 2013, doi: 10.1039/c3sm50451d.

[100] D. Caccavo, S. Cascone, G. Lamberti, and A. A. Barba, “Hydrogels: Experimental characterization and mathematical modelling of their mechanical and diffusive behaviour,” *Chemical Society Reviews*, vol. 47, no. 7. Royal Society of Chemistry, pp. 2357–2373, 2018, doi: 10.1039/c7cs00638a.

[101] Q. Chai, Y. Jiao, and X. Yu, “Hydrogels for Biomedical Applications: Their Characteristics and the Mechanisms behind Them,” *Gels*, vol. 3, no. 1, p. 6, Jan. 2017, doi: 10.3390/gels3010006.

[102] A. Karoyo and L. Wilson, “Physicochemical Properties and the Gelation Process of Supramolecular Hydrogels: A Review,” *Gels*, vol. 3, no. 1, p. 1, Jan. 2017, doi: 10.3390/gels3010001.

[103] A. Duconseille, T. Astruc, N. Quintana, F. Meersman, and V. Sante-Lhoutellier, “Gelatin structure and composition linked to hard capsule dissolution: A review,” *Food Hydrocolloids*, vol. 43. pp. 360–376, 2015, doi: 10.1016/j.foodhyd.2014.06.006.

[104] G. O. Phillips and P. A. Williams, *Handbook of Hydrocolloids: Second Edition*. 2009.

[105] H. Bechir, L. Chevalier, and M. Idjeri, “A three-dimensional network model for rubber elasticity: The effect of local entanglements constraints,” *Int. J. Eng. Sci.*, 2010, doi: 10.1016/j.ijengsci.2009.10.004.

[106] M. C. Wang and E. Guth, “Statistical theory of networks of non-Gaussian flexible chains,” *J. Chem. Phys.*, vol. 20, no. 7, pp. 1144–1157, 1952.

[107] P. J. Flory and J. Rehner Jr, “Statistical mechanics of cross-linked polymer networks I. Rubberlike elasticity,” *J. Chem. Phys.*, vol. 11, no. 11, pp. 512–520, 1943.

[108] L. R. G. Treloar, “The statistical length of long-chain molecules,” *Trans. Faraday Soc.*, vol. 42, pp. 77–82, 1946.

[109] E. M. Arruda and M. C. Boyce, “A three-dimensional constitutive model for the large stretch behavior of rubber elastic materials,” *J. Mech. Phys. Solids*, vol. 41, no. 2, pp. 389–412, Feb. 1993, doi: 10.1016/0022-5096(93)90013-6.

[110] M. C. Boyce, “Direct comparison of the Gent and the Arruda-Boyce constitutive models of rubber elasticity,” *Rubber Chem. Technol.*, vol. 69, no. 5, pp. 781–785, 1996.

[111] P. K. Purohit, R. I. Litvinov, A. E. X. Brown, D. E. Discher, and J. W. Weisel, “Protein unfolding accounts for the unusual mechanical behavior of fibrin networks,” *Acta Biomater.*, vol. 7, no. 6, pp. 2374–2383, Jun. 2011, doi: 10.1016/j.actbio.2011.02.026.

[112] K. Bertoldi and M. C. Boyce, “Mechanics of the hysteretic large strain behavior of mussel byssus threads,” *J. Mater. Sci.*, vol. 42, no. 21, pp. 8943–8956, 2007, doi: 10.1007/s10853-007-1649-z.

[113] C. Marmorat, A. Arinstein, N. Koifman, Y. Talmon, E. Zussman, and M. Rafailovich, “Cryo-Imaging of Hydrogels Supermolecular Structure,” *Sci. Rep.*, vol. 6, no. January, pp. 6–11, 2016, doi: 10.1038/srep25495.

[114] M. Czerner, J. Martucci, L. A. Fasce, R. Ruseckaite, and P. M. Frontini, “Mechanical and fracture behavior of gelatin gels,” in *13th International Conference on Fracture 2013, ICF 2013*, 2013, vol. 6, pp. 4439–4448.

[115] M. Czerner, L. A. Fasce, J. F. Martucci, R. Ruseckaite, and P. M. Frontini, “Deformation and fracture behavior of physical gelatin gel systems,” *Food Hydrocoll.*, vol. 60, pp. 299–307, 2016, doi: 10.1016/j.foodhyd.2016.04.007.

[116] R. W. Ogden and P. R. S. L. A, “Large deformation isotropic elasticity – on the

correlation of theory and experiment for incompressible rubberlike solids," *Proc. R. Soc. London. A. Math. Phys. Sci.*, vol. 326, no. 1567, pp. 565–584, Feb. 1972, doi: 10.1098/rspa.1972.0026.

[117] M. Fang and M. M. B. Holl, "Variation in type I collagen fibril nanomorphology: the significance and origin," *Bonekey Rep.*, 2013, doi: 10.1038/bonekey.2013.128.

[118] P. B. Welzel *et al.*, "Modulating Biofunctional starPEG Heparin Hydrogels by Varying Size and Ratio of the Constituents," *Polymers (Basel).*, 2011, doi: 10.3390/polym3010602.

[119] F. C. Mackintosh, J. Kas, and P. A. Janmey, "Elasticity of Semi-flexible polymer networks," *Phys. Rev. Lett.*, vol. 75, no. 24, p. 4425, 1995, [Online]. Available: https://journals-aps-org.ep.fjernadgang.kb.dk/prl/pdf/10.1103/PhysRevLett.75.4425%0Ahttps://journals.aps.org/prl/pdf/10.1103/PhysRevLett.75.4425.

[120] L. R. G. Treloar, "Calculations of elastic moduli of polymer crystals: I. Polyethylene and nylon 66," *Polymer (Guildf).*, 1960, doi: 10.1016/0032-3861(60)90012-4.

[121] A. Markidou, W.-H. W. Y. W. H. Shih, and W.-H. W. Y. W. H. Shih, "Soft-materials elastic and shear moduli measurement using piezoelectric cantilevers," *Rev. Sci. Instrum.*, vol. 76, no. 6, p. 64302, 2005, doi: 10.1063/1.1928407.

[122] B. Mohanty and H. B. Bohidar, "Microscopic structure of gelatin coacervates," *Int. J. Biol. Macromol.*, vol. 36, no. 1–2, pp. 39–46, 2005, doi: 10.1016/j.ijbiomac.2005.03.012.

[123] N. A. Hotaling, K. Bharti, H. Kriel, and C. G. Simon Jr, "DiameterJ: A validated open source nanofiber diameter measurement tool," *Biomaterials*, vol. 61, pp. 327–338, 2015.

[124] J. Schindelin and others, “Fiji: An open-source platform for biological-image analysis. Nature Methods9, 676--682.” .

[125] J. P. R. O. Orgel, T. C. Irving, A. Miller, and T. J. Wess, “Microfibrillar structure of type I collagen in situ,” *Proc. Natl. Acad. Sci. U. S. A.*, vol. 103, no. 24, pp. 9001–9005, 2006, doi: 10.1073/pnas.0502718103.

[126] M. F. Hadi and V. H. Barocas, “Microscale fiber network alignment affects macroscale failure behavior in simulated collagen tissue analogs,” *J. Biomech. Eng.*, vol. 135, no. 2, pp. 1–8, 2013, doi: 10.1115/1.4023411.

[127] B. A. Roeder, K. Kokini, J. E. Sturgis, J. P. Robinson, and S. L. Voytik-Harbin, “Tensile mechanical properties of three-dimensional type I collagen extracellular matrices with varied microstructure,” *J. Biomech. Eng.*, vol. 124, no. 2, pp. 214–222, 2002, doi: 10.1115/1.1449904.

[128] Y. Tang, R. Ballarini, M. J. Buehler, and S. J. Eppell, “Deformation micromechanisms of collagen fibrils under uniaxial tension,” *J. R. Soc. Interface*, vol. 7, no. 46, pp. 839–850, 2010, doi: 10.1098/rsif.2009.0390.

[129] T. Baumberger, C. Caroli, and D. Martina, “Fracture of a biopolymer gel as a viscoplastic disentanglement process,” *Eur. Phys. J. E*, vol. 21, no. 1, pp. 81–89, 2006, doi: 10.1140/epje/i2006-10048-6.

[130] Y. C. Fung and R. Skalak, “Biomechanics: Mechanical Properties of Living Tissues,” *J. Biomech. Eng.*, 1981, doi: 10.1115/1.3138285.

[131] F. H. Silver and D. L. Christiansen, *Biomaterials Science and Biocompatibility*. 1999.

[132] P. BORNSTEIN and W. TRAUB, “The Chemistry and Biology of Collagen,” in *The Proteins*, 1979.

[133] J. S. Graham, A. N. Vomund, C. L. Phillips, and M. Grandbois, “Structural

changes in human type I collagen fibrils investigated by force spectroscopy," *Exp. Cell Res.*, vol. 299, no. 2, pp. 335–342, 2004.

[134] J. A. J. J. Van Der Rijt, K. O. Van Der Werf, M. L. Bennink, P. J. Dijkstra, and J. Feijen, "Micromechanical testing of individual collagen fibrils," *Macromol. Biosci.*, vol. 6, no. 9, pp. 697–702, 2006, doi: 10.1002/mabi.200600063.

[135] M. P. E. Wenger, L. Bozec, M. A. Horton, and P. Mesquidaz, "Mechanical properties of collagen fibrils," *Biophys. J.*, vol. 93, no. 4, pp. 1255–1263, 2007, doi: 10.1529/biophysj.106.103192.

[136] A. A. Griffith and J. J. Gilman, "The phenomena of rupture and flow in solids," *Trans. ASM*, vol. 61, pp. 855–906, 1968.

[137] S. B. Hutchens, S. Fakhouri, and A. J. Crosby, "Elastic cavitation and fracture via injection," *Soft Matter*, vol. 12, no. 9, pp. 2557–2566, 2016.

[138] A. E. Forte, F. D'amico, M. N. Charalambides, D. Dini, and J. G. Williams, "Modelling and experimental characterisation of the rate dependent fracture properties of gelatine gels," *Food Hydrocoll.*, vol. 46, pp. 180–190, 2015.

[139] C. E. Brennen, *Cavitation and bubble dynamics*. Cambridge University Press, 2014.

[140] S. H. Min and M. L. Berkowitz, "Bubbles in water under stretch-induced cavitation," *J. Chem. Phys.*, 2019, doi: 10.1063/1.5079735.

[141] J. H. Johnston, "The Surface Tension of Protein Solutions. Part III," *Biochem. J.*, 1927, doi: 10.1042/bj0211314.

[142] H. Sato and K. Ueberreiter, "Surface tension of aqueous gelatin solutions, 1. Concentration dependence," *Die Makromol. Chemie Macromol. Chem. Phys.*, vol. 180, no. 3, pp. 829–835, 1979.

[143] N. G. Parker and M. J. W. Povey, "Ultrasonic study of the gelation of gelatin:

Phase diagram, hysteresis and kinetics," *Food Hydrocoll.*, 2012, doi: 10.1016/j.foodhyd.2011.04.016.

[144] P. Lubock and W. Goldsmith, "Experimental cavitation studies in a model head-neck system," *J. Biomech.*, vol. 13, no. 12, pp. 1041–1052, 1980.

[145] G. S. Nusholtz, E. B. WYLIE, and L. E. E. G. GLASCOE, "Internal cavitation in simple head impact model," *J. Neurotrauma*, vol. 12, no. 4, pp. 707–714, 1995.

[146] D. F. Moore, R. A. Radovitzky, L. Shupenko, A. Klinoff, M. S. Jaffee, and J. M. Rosen, "Blast physics and central nervous system injury," 2008.

[147] A. Thiruvengadam, "A Unified Theory of Cavitation Damage," - *Journal of Basic Engineering*, no. 3. ASME, p. 365, 1963.

[148] D. W. Hyde, "CONWEP 2.1. 0.8, Conventional Weapons Effects Program," *Vicksburg, MS United States Army Corps Eng.*, 2004.

[149] R. K. Gupta and A. Przekwas, "Mathematical models of blast-induced TBI: Current status, challenges, and prospects," *Front. Neurol.*, vol. 4 MAY, no. May, pp. 1–21, 2013, doi: 10.3389/fneur.2013.00059.

[150] "ANSYS (R) Academic Research Mechanical and CFD, Release 19.1." .

[151] "ANSYS (R) Academic Research Mechanical and CFD, Release 19.1, Fluent User Guide." .

[152] F. Habla, H. Marschall, O. Hinrichsen, L. Dietsche, H. Jasak, and J. L. Favero, "Numerical simulation of viscoelastic two-phase flows using openFOAM®," *Chem. Eng. Sci.*, vol. 66, no. 22, pp. 5487–5496, 2011, doi: http://dx.doi.org/10.1016/j.ces.2011.06.076.

[153] Z.-Y. Zheng, F.-C. Li, and J.-C. Yang, "Modeling asymmetric flow of viscoelastic fluid in symmetric planar sudden expansion geometry based on user-defined function in FLUENT CFD package," *Adv. Mech. Eng.*, vol. 5, p. 795937, 2013, doi:

10.1155/2013/795937.

[154] F. Belblidia, I. J. Keshtiban, and M. F. Webster, “Stabilised computations for viscoelastic flows under compressible implementations,” *2nd Annu. Eur. Rheol. Conf.*, vol. 134, no. 1, pp. 56–76, 2006, doi: https://doi.org/10.1016/j.jnnfm.2005.12.003.

[155] P. C. Bollada and T. N. Phillips, “On the Mathematical Modelling of a Compressible Viscoelastic Fluid,” *Arch. Ration. Mech. Anal.*, vol. 205, no. 1, pp. 1–26, Jul. 2012, doi: 10.1007/s00205-012-0496-5.

[156] M. S. Darwish, J. R. Whiteman, and M. J. Bevis, “Numerical modelling of viscoelastic liquids using a finite-volume method,” *J. Nonnewton. Fluid Mech.*, vol. 45, no. 3, pp. 311–337, 1992, [Online]. Available: http://ns6rl9th2k.search.serialssolutions.com?ctx_ver=Z39.88-2004&ctx_enc=info:ofi/enc:UTF-8&rfr_id=info:sid/ProQ%253Acomputerinfo&rft_val_fmt=info:ofi/fmt:kev:mtx:journal&rft.genre=article&rft.jtitle=Journal+of+Non-Newtonian+Fluid+Mechanics&rft.atitle=Nu.

[157] M. F. Tomé, M. S. B. de Araujo, M. A. Alves, and F. T. Pinho, “Numerical simulation of viscoelastic flows using integral constitutive equations: A finite difference approach,” *J. Comput. Phys.*, vol. 227, no. 8, pp. 4207–4243, 2008.

[158] “ANSYS (R) Academic Research Mechanical and CFD, Release 19.1, Fluent Theory Guide.” .

[159] F. Hamaguchi and K. Ando, “Linear oscillation of gas bubbles in a viscoelastic material under ultrasound irradiation,” *Physics of Fluids*, vol. 27, no. 11. American Institute of Physics, Melville, NY :, p. 113103, 2015, doi: 10.1063/1.4935875.

[160] S. Catheline, “Measurement of viscoelastic properties of homogeneous soft solid

using transient elastography: An inverse problem approach," *J. Acoust. Soc. Am.*, vol. 116, no. 6, pp. 3734–3741, 12AD.

[161] L. Liu, Y. Fan, and W. Li, "Viscoelastic shock wave in ballistic gelatin behind soft body armor," *Journal of the mechanical behavior of biomedical materials.*, vol. 34. Elsevier, Amsterdam] :, pp. 199–207, 2014, doi: 10.1016/j.jmbbm.2014.02.011.

[162] V. T. Nayar, J. D. Weiland, C. S. Nelson, and A. M. Hodge, "Elastic and viscoelastic characterization of agar," *Journal of the mechanical behavior of biomedical materials.*, vol. 7. Elsevier, Amsterdam] :, pp. 60–68, 2012, doi: 10.1016/j.jmbbm.2011.05.027.

[163] J. Zhang, C. R. Daubert, and E. A. Foegeding, "Characterization of polyacrylamide gels as an elastic model for food gels," *Rheologica acta*, vol. 44, no. 6. Springer, Berlin ;, pp. 622–630, 2005, doi: 10.1007/s00397-005-0444-5.

[164] T. G. Goktekin, "Animating Viscoelastic Fluids," University of California, Berkeley, 2011.

[165] D. Chakraborty and J. E. Sader, "Constitutive models for linear compressible viscoelastic flows of simple liquids at nanometer length scales," *Phys. Fluids*, 2015, doi: 10.1063/1.4919620.

[166] W. Lauterborn and C. D. Ohl, "Cavitation bubble dynamics," *Ultrason. Sonochem.*, 1997, doi: 10.1016/S1350-4177(97)00009-6.

[167] H. F. Brinson and L. C. Brinson, *Polymer Engineering Science and Viscoelasticity*. Boston, MA: Springer, 2008.

[168] E. Johnsen and L. Mancia, "Bubble dynamics in soft materials: Viscoelastic and thermal effects," in *Journal of Physics: Conference Series*, 2015, vol. 656, no. 1, doi: 10.1088/1742-6596/656/1/012022.

[169] R. M. Wright and K. T. Ramesh, "An axonal strain injury criterion for traumatic

brain injury," *Biomech. Model. Mechanobiol.*, vol. 11, no. 1–2, pp. 245–260, 2012, doi: 10.1007/s10237-011-0307-1.

[170] N. Kasthuri *et al.*, "Saturated Reconstruction of a Volume of Neocortex," *Cell*, 2015, doi: 10.1016/j.cell.2015.06.054.

[171] H. Ouyang, E. Nauman, and R. Shi, "Contribution of cytoskeletal elements to the axonal mechanical properties," *J. Biol. Eng.*, vol. 7, no. 1, p. 21, 2013, doi: 10.1186/1754-1611-7-21.

[172] J. Wu *et al.*, "Mathematical modelling of microtubule-tau protein transients: Insights into the superior mechanical behavior of axon," *Appl. Math. Model.*, vol. 71, pp. 452–466, Jul. 2019, doi: 10.1016/j.apm.2019.02.030.

[173] F. Pampaloni, G. Lattanzi, A. Jonáš, T. Surrey, E. Frey, and E. L. Florin, "Thermal fluctuations of grafted microtubules provide evidence of a length-dependent persistence length," *Proc. Natl. Acad. Sci. U. S. A.*, 2006, doi: 10.1073/pnas.0603931103.

[174] M. Soheilypour, M. Peyro, S. J. Peter, and M. R. K. Mofrad, "Buckling behavior of individual and bundled microtubules," *Biophys. J.*, vol. 108, no. 7, pp. 1718–1726, 2015, doi: 10.1016/j.bpj.2015.01.030.

[175] K. J. Rosenberg, J. L. Ross, H. E. Feinstein, S. C. Feinstein, and J. Israelachvili, "Complementary dimerization of microtubule-associated tau protein: Implications for microtubule bundling and tau-mediated pathogenesis," *Proc. Natl. Acad. Sci. U. S. A.*, 2008, doi: 10.1073/pnas.0802036105.

[176] M. G. Spillantini and M. Goedert, "Tau protein pathology in neurodegenerative diseases," *Trends in Neurosciences*. 1998, doi: 10.1016/S0166-2236(98)01337-X.

[177] S. J. Peter and M. R. K. Mofrad, "Computational modeling of axonal microtubule bundles under tension," *Biophys. J.*, vol. 102, no. 4, pp. 749–757, 2012, doi:

10.1016/j.bpj.2011.11.4024.

[178] H. Ahmadzadeh, D. H. Smith, and V. B. Shenoy, “Viscoelasticity of tau proteins leads to strain rate-dependent breaking of microtubules during axonal stretch injury: Predictions from a mathematical model,” *Biophys. J.*, vol. 106, no. 5, pp. 1123–1133, 2014, doi: 10.1016/j.bpj.2014.01.024.

[179] S. Wegmann, J. Schöler, C. A. Bippes, E. Mandelkow, and D. J. Muller, “Competing interactions stabilize pro- and anti-aggregant conformations of human Tau,” *J. Biol. Chem.*, 2011, doi: 10.1074/jbc.M111.237875.

[180] N. Hirokawa, Y. Shiomura, and S. Okabe, “Tau proteins: the molecular structure and mode of binding on microtubules.,” *J. Cell Biol.*, 1988, doi: 10.1083/jcb.107.4.1449.

[181] P. A. Janmey, U. Euteneuer, P. Traub, and M. Schliwa, “Viscoelastic properties of vimentin compared with other filamentous biopolymer networks,” *J. Cell Biol.*, 1991, doi: 10.1083/jcb.113.1.155.

[182] P. Chełminiak, J. M. Dixon, and J. A. Tuszyński, “Torsional elastic deformations of microtubules within continuous sheet model,” *Eur. Phys. J. E*, 2010, doi: 10.1140/epje/i2010-10562-x.

[183] K. K. Sarangapani, B. Akiyoshi, N. M. Duggan, S. Biggins, and C. L. Asbury, “Phosphoregulation promotes release of kinetochores from dynamic microtubules via multiple mechanisms,” *Proc. Natl. Acad. Sci. U. S. A.*, 2013, doi: 10.1073/pnas.1220700110.

[184] A. Naik, N. Abolfathi, G. Karami, and M. Ziejewski, “Micromechanical viscoelastic characterization of fibrous composites,” *J. Compos. Mater.*, vol. 42, no. 12, pp. 1179–1204, 2008, doi: 10.1177/0021998308091221.

[185] C. Tzikang and T. Chen, “Determining a Prony Series for a Viscoelastic Material

From Time Varying Strain Data," *Nasa*, 2000.

[186] C. T. Sun and R. S. Vaidya, "Prediction of composite properties from a representative volume element," *Compos. Sci. Technol.*, vol. 56, no. 2, pp. 171–179, 1996, doi: 10.1016/0266-3538(95)00141-7.

[187] W. H. Press, B. P. Flannery, S. A. Teukolsky, W. T. Vetterling, and others, "Numerical recipes." Cambridge University Press Cambridge, 1989.

[188] H. P. Gavin, "The Levenburg-Marqurdt Algorithm For Nonlinear Least Squares Curve-Fitting Problems," *Duke Univ.*, 2019.

Biographical Information

Fuad Hasan has earned a Ph.D. in Aerospace Engineering from the University of Texas at Arlington (UTA) in the summer of 2020. He joined the Multiscale Mechanics and Physics Laboratory (MMPL) in fall 2016 and started his research under the supervision of Professor Ashfaq Adnan. Before joining UTA, he earned two Master's degrees in Mechanical Engineering (the University of Texas at San Antonio, 2016) and in Aerospace Engineering (University of Pisa, 2014), respectively. Fuad completed his Bachelor in Science in Mechanical Engineering from the Military Institute of Science and Technology (Bangladesh) in 2010. After his undergrad, he joined his alma mater as Lecturer in the Mechanical Engineering department and worked there until he got Erasmus Mundus scholarship to study in Pisa.

Fuad's research interests include multiscale computational mechanics (CFD and FEM), damage and fracture of soft materials, fluid-solid interaction, etc. He worked on the traumatic brain injury project that was funded by the Office of Naval Research (ONR) and collaborated with the Naval Research Lab (NRL). He also worked as the graduate teaching assistant (GTA) at UTA and UTSA. He was the GTA of the finite element method and the numerical method courses, respectively. Other than his research works, Fuad was involved with extra-curricular activities and assumed the position of the President of the Bangladesh Student Organization (BSO). His hobbies include photography, sports (soccer, cricket, table tennis), and travel. In the future, he would like to pursue his career in either academic or research.